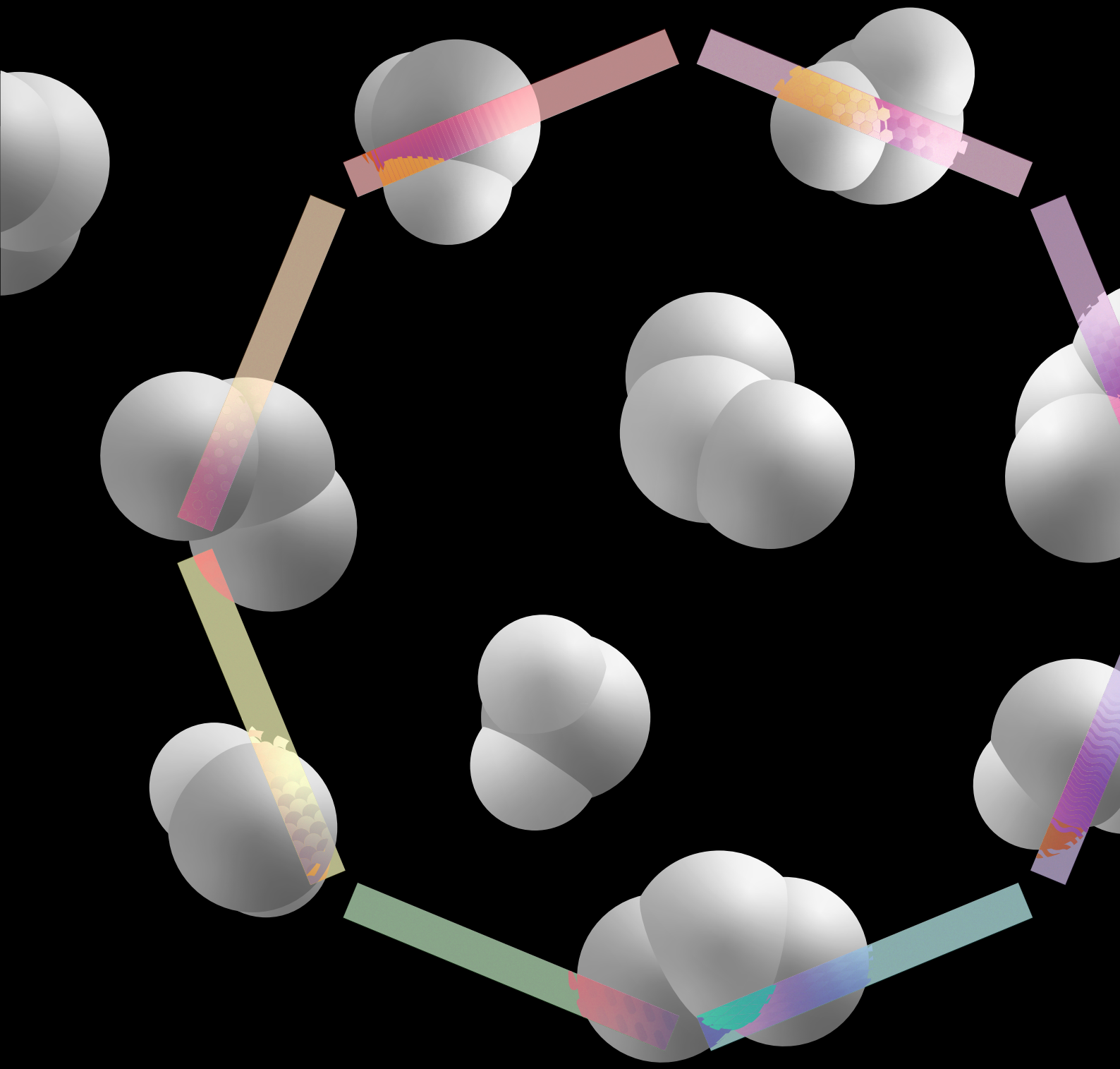

Gas Sensor Based on **Array of Multi-Layer Graphene** Decorated with **Metal/Metal Oxide Nanoparticles**

TU Delft

Master of Science
Microelectronics
Electrical Engineering
EEMCS

Hanxing Meng
5280230

22 Aug 2022

GAS SENSOR BASED ON ARRAY OF MULTI-LAYER GRAPHENE DECORATED WITH METAL/METAL OXIDE NANOPARTICLES

A thesis submitted to the Delft University of Technology in partial fulfillment of the requirements for the degree of

Master of Science in Microelectronics

by

Hanxing Meng

August 2022

Hanxing Meng: *Gas Sensor Based on Array of Multi-layer Graphene Decorated with Metal/Metal Oxide Nanoparticles* (2022)

The work in this thesis was made in the:

Electronic Components, Technology and Materials
Department of Microelectronics
Faculty of Electrical Engineering, Mathematics & Computer Science
Delft University of Technology

Supervisors: Dr.ir. S. Vollebregt
Dr. L.N. Sacco

ABSTRACT

Graphene as an allotrope of carbon is promising for the detection of gaseous molecules due to its extremely high surface-to-volume ratio. However, its low selectivity poses a major problem for practical applications. The work presented in this thesis addresses the selectivity problem by depositing metal/metal oxide nanoparticles (NPs) on the surface of graphene.

For this purpose, gas sensors with multiple multi-layer graphene (MLG) strips were fabricated. Four types of metal/metal oxide nanoparticles were investigated: Gold (Au), Platinum (Pt), Copper (Cu), and Iron (Fe). Various techniques were developed to study the properties of graphene and NPs. In addition, an automatic measurement setup with multi-strips switching is developed for data acquisition. Finally, the sensors decorated with different metal types and coverages are investigated for their response to H_2O and NO_2.

The study shows that both the pristine devices and the sensors decorated with NPs hardly response to water molecules, while the responses to NO_2 are larger and vary depending on the NPs. The results are promising for the development of a gas sensor array based on this methodology with improved selectivity for gas detection.

ACKNOWLEDGEMENTS

This endeavor would not have been possible without my daily supervisor, Leandro. His patience, enthusiasm, and intelligence encouraged me at every stage. I would also like to express my deepest appreciation to my professor Sten for his invaluable support and feedback. He has helped me overcome the obstacles along the journey with his knowledge and experience.

My thanks also go to Shanliang for his help with the measurement setup, Joost for training in NP printing and Cascade, Dong for helping me with the equipment, Jiarui for helping me during the process, and all the people in our group for their encouragement and support. Thanks are also due to the EKL staff for their help during the process phase. I would also like to thank the other master students, especially my office mates in the old and new offices and the member of my Nanoprinter group, for their support in work and in life. I also thank my roommates and friends. We had many nice, relaxing weekends that kept me working hard on the weekdays. A special thanks also goes to my friend Bo-fan for the great cover design.

Finally, I thank my parents for their constant support throughout my life. Their belief in me kept my motivation high during my studies.

CONTENTS

LIST OF FIGURES

LIST OF TABLES

1 INTRODUCTION

The rapid development in various industries has pushed the boundary of our possibility, but, at the same time, adding greatly to the air pollution. According to the European Environment Agency and the World Health Organization (WHO), air pollution is currently recognized as the single biggest environmental threat to human health both in Europe and worldwide[17]. Each year, more than seven million deaths are directly caused by exposure to ambient and household air pollution, while regarding many other life-threatening environmental problems, such as acid rain, eutrophication, haze, ozone depletion, etc, air pollution is identified as the main contributor. Though over the recent decades, the air quality has shown some improvement[18], more than 91% of the world population lives in places where air pollution levels exceed the WHO guideline limits.

In parallel to finding more sustainable ways of development, monitoring the air quality, or the gas compositions helps people understand the environment in which they, or others, live. Therefore, gas sensors, as a fundamental need, are constantly being improved in terms of versatility, and efficiency[19]. As will be elaborated in Chapter 2, these are typically quantified by a number of technical properties, including sensitivity, selectivity, stability, power consumption, response/recovery rate, and size.

1.1 MOTIVATION AND PROBLEM FORMULATION

The first gas sensors, electrolyte-solution-based electrochemical sensors, were invented back in the 70's[20]. Since then, both their technologies and their applications of them have been growing. Depending on their intended environment and function, the physical makeup and sensing process can vary significantly between sensors.

The metal oxide based gas sensor is one of the most commonly used types of electrochemical gas sensors, which feature high sensitivity, stability, small size, and low cost. gaining them some fans in the industry[21]. However, their high operation temperature, subsequently high power consumption, and poor selectivity, strongly restrict their applications.

An emerging material alternative to MOS used for gas-sensing is carbon-based nanomaterials (SNMs), including graphene, carbon nanotubes (CNTs), and their derivatives. In general, their distinctive structures provide a large specific surface, suitable for gas-sensing, as well as excellent electron transportation properties, which make them ideal candidates for room temperature (RT) gas-sensing Within this category, CNT-based gas sensors show several drawbacks. compared to graphene. First, the recovery time of CNT-based gas sensors is usually long, as a result of the high bonding energy they form with many gases or organic vapors. Their designed recovery time at room temperature is around 10h[22]. Second, the fabrication of CNT-based sensors involves highly complicated processes, which often impose both technological and economical obstacles to their uses.

Graphene, on the other hand, is (or is composed of) two-dimensional (2D) materials. It turns out to have outstanding characteristics in gas sensing, including large surface areas, good molecule-scale sensitivities, room temperature operation capabilities, small size, and low electronic noise, all differentiating it from other ma-

terials at an unprecedented scale[23]. However, graphene also has some downsides: slow recovery, lack of saturation, and poor selectivity. This study will explore the methods to solve the last issue.

On top of that, graphene can achieve even higher sensitivity and selectivity by having its surface functionalized with metal, metal oxide, or other molecules[21]. Metal or metal oxide nanoparticles (NPs) can not only make chemical doping but also create additional interaction sites which can add to graphene's sensitivity towards certain molecules. For example, the epitaxial graphene functionalized with Fe_3O_4 or TiO_2 can easily detect benzene down to 5 ppb, a precision level the non-functionalized graphene can not reach[24].

Thanks to it, one can not only use graphene for detecting a single gas type but also build so-named sensor arrays by combining differently functionalized graphenes. As to be explained in Chapter 2, sensor arrays, or electronic noses, can achieve distinguished selectivity through the characteristic signature derived from the different responses towards a target analyte given by multiple sensors in the array[25].

1.2 THESIS OBJECTIVES

Because of the many potentials of graphene-based gas sensors, the study wants to further explore their capabilities and applicabilities. In particular, it investigates a type of sensor that combines the above-mentioned elements - sensor arrays composed of graphene sensors functionalized by mental/metal oxide NPs, by designing, making, and testing a selection of its possible implementation.

1.3 THESIS OUTLINE

The thesis comprises five chapters:

- Introduction: the current chapter which clarifies the motivation, the objectives, and the methodologies of this study;
- Background theory and concepts: a chapter that provides background knowledge, concepts, and the latest research outcomes, regarding graphene, graphene sensors, metal/metal oxide NPs, and sensor arrays;
- Experimental methods: a chapter to explain the complete fabrication flow of functionalized graphene-based gas sensors, with emphasis on the graphene synthesis and NP functionalization steps. Additionally, it demonstrates the sensor device setup as well as the automation of the sensor operations;
- Characterization: a chapter that discusses the characterization methods both for the sensor materials and sensor devices. The former includes Raman spectra, scanning electron microscopy (SEM), and atomic force microscopy (AFM) For the devices, their sheet resistances are measured and visualized in a colored wafer map while their TCR values are depicted in drawings;
- Gas sensor tests: a chapter that performs all the gas tests. For the humidity test, three types of devices are tested: the pristine MLG devices with a SiO_2 substrate, the Au-NPs functionalized devices, and the pristine MLG devices integrated onto a micro-hotplate with a SiN_x substrate. As for NO_2, the pristine MLG devices are tested, followed by the Au, Pt, and Cu nanoparticles deposited devices.

2 BACKGROUND THEORY AND CONCEPTS

As briefly introduced in Chapter 1, graphene-based sensors are advantageous in many ways, especially when combined with functionalization and/or used together as a sensor array. Based on existing studies, this chapter first explains the reasons behind and unveils the underlying mechanisms. On top of that, the different configurations and fabrication possibilities are discussed, which provides directions for the steps that follow.

2.1 GRAPHENE

An introduction of graphene and its significant properties are given in this section, including its mechanical properties and allotropes. Next to it, the common methods for the synthesis of graphene are discussed.

2.1.1 Introduction to graphene

Graphene refers to the 2D matrix of carbon atoms arranged in a honeycomb lattice, which was predicted by P.R. Wallace in 1947, regarding its electronic structure and the linear dispersion relation [26]. But, it was not until 2004, K.S. Novoselov and A.K. Geim extracted thin layers of graphite from a graphite crystal using simple mechanical exfoliation with scotch tape [27]. Since then, graphene has attracted an exponential amount of attention among researchers, and lots of techniques have been designed and investigated to produce graphene-based materials for various applications.

More precisely, graphene is a one-atom-thick layer of sp^2 carbon atoms bonded together in a repeating pattern of hexagons. The bond length between these carbon atoms is 0.142 nm, as shown in Figure 2.1. It is the fundamental building block of several carbon allotropes, as summarized in Figure 2.2. O-dimensional (0-D) fullerene is an 0-dimensional allotrope formed by cutting and folding graphene into a spherical shape, while 1-dimensional CNT is built by rolling up graphene into a cylinder and 3-dimensional graphite comes from stacked graphene layers[1].

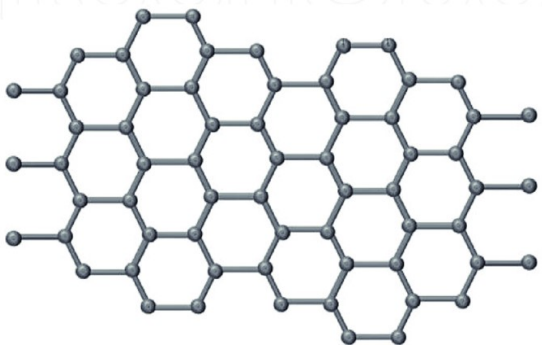

Figure 2.1: Carbon atoms bonded in a honeycomb lattice, showing C-C bond length of 0.142 nm in graphene structure [1]

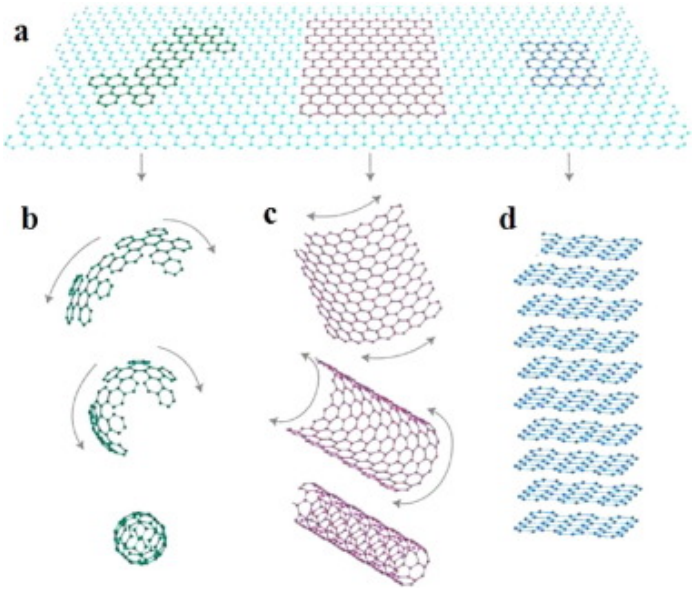

Figure 2.2: Allotropes of carbon: a) 2-D graphene; b) 0-D fullerene; c) 1-D carbon nanotube; d) 3-D graphite. [1]

Although graphene is the thinnest and lightest material known to humans in that it can reach one atom thick and weighs as low as 0.77 milligrams per square meter (1g of single-layer graphene can cover 1298.7 square meters), it is incredibly strong with Young's modulus of 1.0 ± 0.1 TPa and tensile strength of 130 GPa [28]. Next to the strength, graphene exhibits other excellent mechanical and chemical properties, such as a high surface-to-volume ratio (2630 m^2g^-1)[29], uniform and high light transmittance (around 98 %), high thermal conductivity (5000 Wm^-1K^-1)[30] and good chemical stability [31]. These values are all experimentally measured.

2.1.2 Electrical properties

The signiture two-dimensional lattice structure consists of hexagonal rings/chains of covalently bonded carbon atoms, like a honeycomb. Within the structure, two types of carbon atoms are present, shown as A and B in Figure 2.3. The lattice vectors of the real space unit cell are described by,

$$\vec{a}_1 = \frac{a}{2}(3, \sqrt{3}), \vec{a}_2 = \frac{a}{2}(3, -\sqrt{3}) \tag{2.1}$$

where a is the lattice constant defined as $a = \sqrt{3}\, a_0$, where $a_0 \approx 1.42\mathring{A}$, which is the nearest neighbor inter-atomic distance.

The first Brillouin zone (BZ) is represented in the reciprocal lattice, whose vectors are described by

$$\vec{b}_1 = \frac{2\pi}{3a}(1, \sqrt{3}), \vec{b}_2 = \frac{2\pi}{3a}(1, -\sqrt{3}) \tag{2.2}$$

The corners of the graphene BZ are marked by six points, two of which are heterogeneous due to the two sub-lattices A and B. These two points are represented by K and K' in the right figure of Figure 2.3, y named the Dirac points. Their positions in the momentum space can be described by

$$\vec{K} = \frac{2\pi}{3a}(1, \frac{1}{\sqrt{3}}), \vec{K'} = \frac{2\pi}{3a}(1, -\frac{1}{\sqrt{3}}) \tag{2.3}$$

Figure 2.4shows the low-energy-band structure of graphene and the six Dirac points, in which the valence and conduction band meet in the reciprocal space at

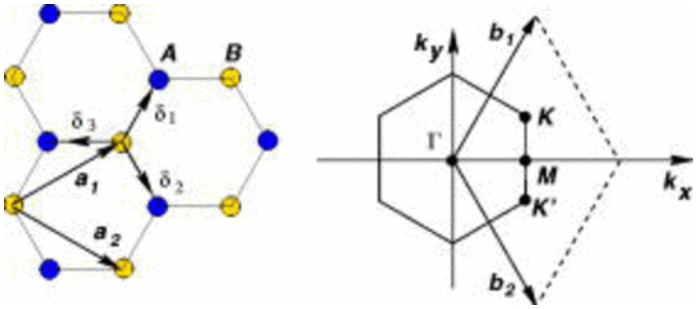

Figure 2.3: Left: The Honeycomb lattice of graphene, made out of two overlapping triangular sub-lattices (A: blue atoms and B: yellow atoms). The vectors a_1 and s_2 are the lattice unit vectors, and δ_1, δ_2 and δ_3 are the nearest-neighbor vector. Right: Reciprocal lattice with the first Brillouin zone. The Dirac cones are located at the K and K′ points. [2]

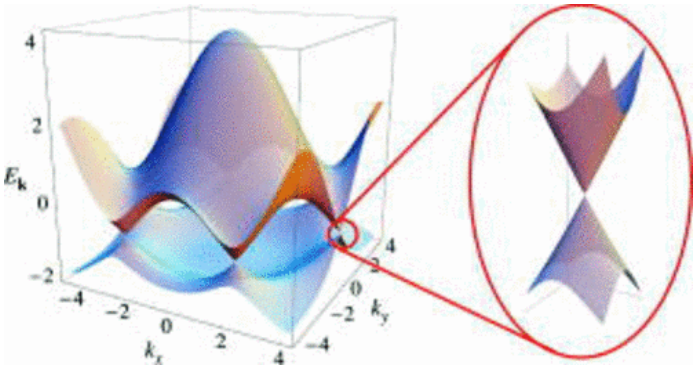

Figure 2.4: Dirac points in graphene with the electronic dispersion of the honeycomb lattice zoomed in the energy spectrum of finite values [3]

the Dirac points. As illustrated, they are perfectly symmetrical with respect to the Fermi energy level referred to as $E_F = 0\ eV$. The energy dispersion (the spectrum for excitations) close to the Direc points is linear near the six individual corners of the Brillouin zone. Furthermore, the effective mass of the electrons and holes is equal to the second derivative of the energy versus momentum relation. Therefore, an electron has a zero effective mass. This is also the reason why the electron mobility of graphene is extremely high.

This linear energy dispersion also forms a conic-shape energy band, namely the Dirac cone, whose density of states (DOS) can be calculated by,

$$DOS(E) = \frac{2|E|}{\pi(\hbar v_F)^2} \tag{2.4}$$

where E is the electron(hole) energy, $\hbar$ is the reduced Planck constant, and v_F is the Fermi velocity [32]. Hence, the DOS is linearly correlated with energy, while becoming zero at the Dirac points.

Another unique and probably the most appreciated property of graphene is that it is a zero-overlap semimetal with very high electrical conductivity. A carbon atom has six electrons in total, two of which are located in the inner shell while the other four are in the outer shell, which is usually available for chemical bonding. In graphene, three out of the four outer shell electrons are occupied to form the two-dimensional plane, leaving one atom freely available for electrical conduction. These highly-mobile electrons, sometimes called π electrons, are ready to create π-bonds with external atoms and molecules. It is these bonding and anti-bonding relations that are responsible for the unique electronic properties of graphene.

Graphene is often categorized by the number of layers. True graphene usually refers to a monolayer, or single layer graphene (SLG), which is only one atomic

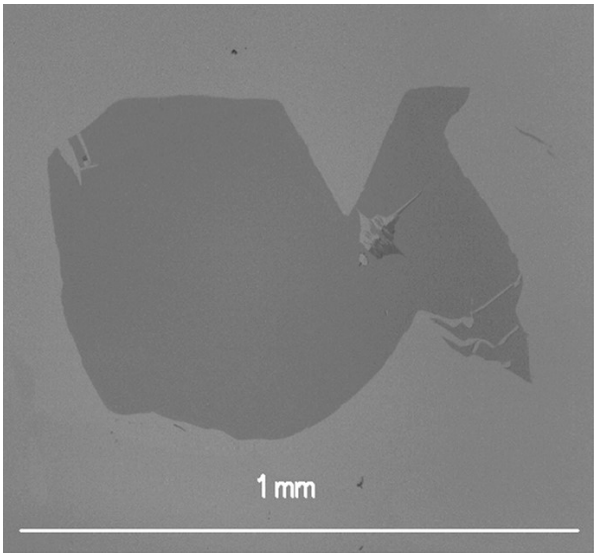

Figure 2.5: A monolayer graphene flake generated by Mechanically exfoliated on 300 nm SiO_2 surface [3]

layer thick. With up to 10 layers, it is named a few layers of graphene (FLG), while those of above 10 layers are called multi-layers graphene (MLG)[33].

2.1.3 Graphene growth and functionalization

Up to now, many techniques have been developed to synthesize graphene, each of which leads to different extra characteristics[1].

The first method, known as Mechanical Exfoliation (ME) or the Scotch Tape technique, was introduced by Noveselov *et al*. in 2004[25] . ME uses a high tack tape (e.g. $Nitto^{TM}$ tape) to peel thin flakes from a bulk graphite crystal. Multiple peeling can be done to reduce the thickness of a thin flake until almost no residue is left, making it possible to obtain SLG that is a few millimeters thick. Figure 2.5 shows a piece of SLG obtained from ME on a 300 nm SiO_2 (substrate). Graphene produced by this method generally presents the best quality and exhibits fewer lattice defects and less superficial contamination compared to those from other techniques. However, this method cannot be adopted in a commercial context because of its scaling limitation.

Another approach to producing graphene is Liquid Phase Exfoliation (LPE), which exfoliates graphene chemically. This method requires a solvent, whose surface energy is comparable to that of graphene. The interface between the graphene and such a solvent can provide sufficient energy that exfoliates graphene from bulk graphite. The number of layers can be altered through a series of post-treatment, hence the graphene thickness can be controlled. In this approach, the solvent and substrate strongly determine the quality of the graphene produced. Nonetheless, the quality is normally suboptimal compared to that of ME [3].

A common implementation for mass production of graphene is CVD. In this method, a hydrocarbon-based gas as the source undergoes chemical reactions at a high temperature. As illustrated in Figure 2.6, during the reaction, the carbon atoms leave the gas, get attracted to a transition metal substrate, and form single- or multi-layer substrate, e.g. Ni for multi-layer graphene [34], Cu for single-layer graphene [35]. CVD provides an inexpensive method to produce graphene with reasonably high quality, potentially on a large scale. However, the resulted graphene still needs to be transferred to an insulating substrate.

Another technique to produce graphene is the thermal decomposition of SiC, which provides a highly reproducible way to obtain homogenous large-area graphene.

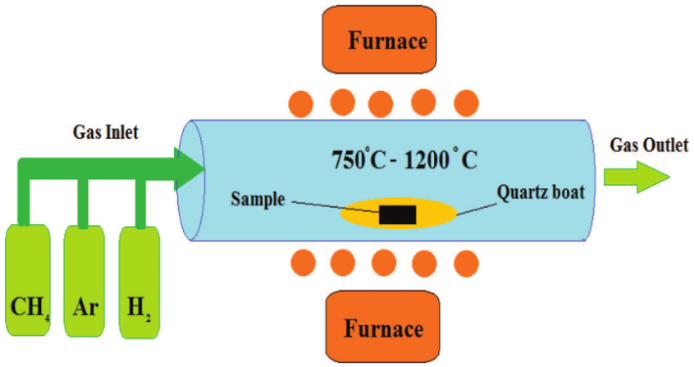

Figure 2.6: The schematic of the CVD graphene grown on metals with high carbon solubility

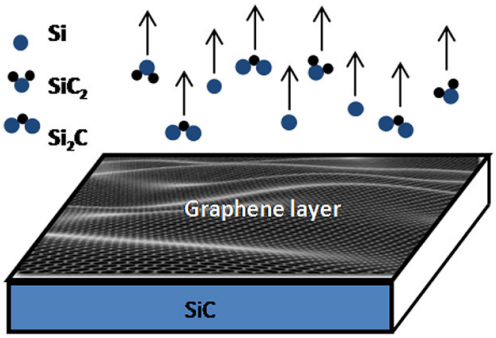

Figure 2.7: Illustration of the epitaxial graphene on Silicon Carbide [4]

As shown in Figure 2.7, Silicon Carbide, as the raw material, is annealed at high temperature either in a vacuum or under atmospheric pressure. At a high temperature, the silicon atoms in SiC evaporate while the carbon atoms stY on the surface, thus forming the graphene layers[4].

Lastly, the Laser-Induced technique provides scalable produce and pattern porous graphene, in which a pulsed CO_2 infrared laser is used to directly convert the polymer films to three-dimensional (3D) porous graphene. During this process, sp_3 carbon atoms are photothermally converted into sp_2 carbon atoms by the laser. The graphene produced by this method is called Laser-Induced graphene (LIG) and features high electrical conductivity [36].

In addition to the aforementioned methods, many more are available to produce graphenes, such as synthetic route, splitting nanotubes, and reduction of graphene oxide through heating. Efforts are consistently being made for the development and improvement of various techniques, yet each has its own advantages and disadvantages[1]. The choice of technique differs per application and varies based on different criteria, such as the quality and the scale.

2.2 GRAPHENE-BASED GAS SENSOR

As previously explained, graphene has a large theoretical surface area (2630 $m^2g^{-}1$) and can thus provide an ideal surface-to-volume ratio, up to the extent that every atom in graphene can be regarded as a reactive site[7]. Additionally, the various interaction between the graphene and the target gases, the zero rest mass of the charge carriers near the Dirac points, the high carrier mobility, and the low electrical noise, all make graphene an excellent material for gas sensing. To provide a better picture, this section starts with an overview of the sensing mechanism of the graphene-based gas sensors. After that, the most important sensor performance pa-

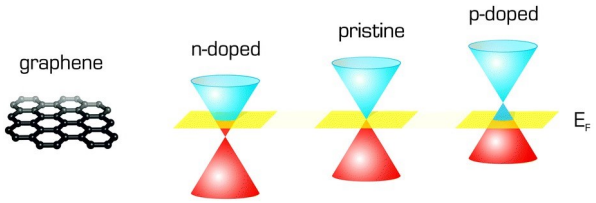

Figure 2.8: The band structure of the single layer graphene with n-type doping and p-type doping with the respect to the Fermi level [5]

rameters and the ways of optimization are discussed. Finally, the limitations along with the ways to deal with them are reviewed.

2.2.1 Sensing mechanism

Graphene responds differently to different gases in terms of its conductance. For example, the electron-donating gas molecules decrease the conductance of p-type doped graphene, while the electron-withdrawing gas molecules increase it [3]. The sensitivity of graphene-based gas sensors can be ultimately high that the detection of a single gas molecule is possible [6].

A graphene-based gas sensor can be fabricated for different device configurations. The most common and widely used one is chemiresistor. In this configuration, the detection of gas relies on the resistance change of the sensing material induced by the absorption or desorption of the target gas. Though generally, graphene is a p-type semiconductor due to the residual oxygen-containing groups and the existence of the water molecules [37], its electron concentration can change as a result of absorption or desorption, which furtherly leads to E_F level change, as illustrated in Figure 2.8.

In the case that the graphene is exposed to electron-withdrawing gases, for example, CO_2, H_2O and NO_2, the electrons are transferred from the graphene to the adsorbed gas, as shown in the left figure of Figure 2.9, which subsequently decreases the electron concentration and in the meantime increases the hole concentration in the graphene. As a result, the conductivity of graphene will increase due to its p-type behavior. Conversely, if the graphene is exposed to electron-donating gases, for example, NH_3 and CO, the electrons will be transferred from the exposed gas to the graphene, as shown in the left figure of Figure 2.9, which increases the electron concentration and decrease the hole concentration in graphene. Subsequently, the conductivity will decrease as well [21]. Figure 2.10 provides the resistivity change caused by the electron transfer of the graphene under different types of gases, mentioned above.

Another common configuration is graphene-based Field effect transistors (FET). In this configuration, the graphene is employed as a channel material between the source and drain electrodes, as shown in Figure 2.11. By absorption of the target gas, the conductivity of the graphene changes, leading to a noticeable variation in the drain current, from which the concentration of the absorbed gas can be deduced.

Yet a popular configuration is the surface work function (SWF) change transistor, which relies on the surface dipole moment and the electron affinity change caused by the absorption of the gas molecules. Comparably, the frequency change caused by the surface mass change can also be used to realize gas sensing, which is known as the Surface Acoustic Wave (SAW) technique [7].

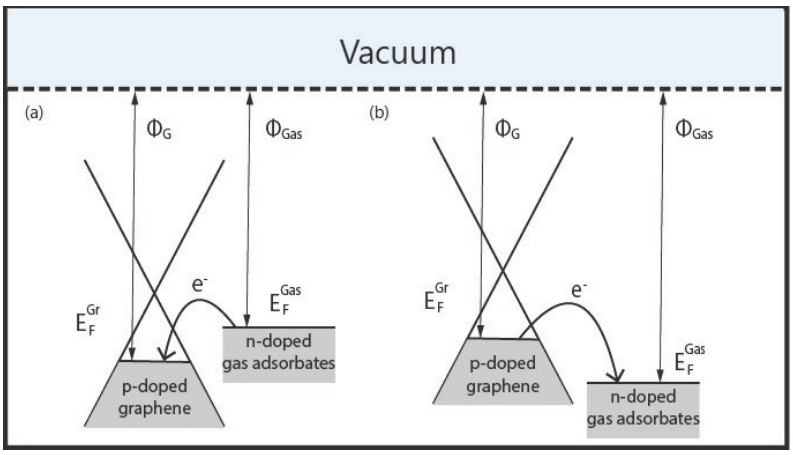

Figure 2.9: The band diagram of p-doped graphene accepting (donating) electrons from (to) an electron donating (accepting) gas.

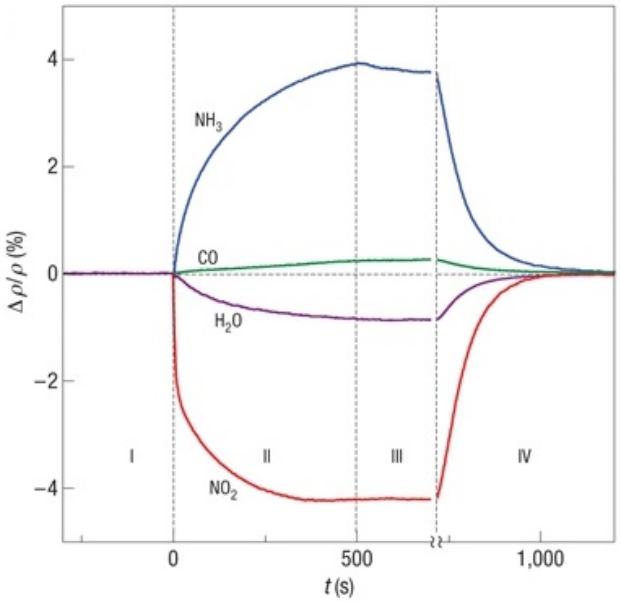

Figure 2.10: The resistivity change caused by the exposure to various gases with a concentration of 1 p.p.m of graphene-based chemiresistor gas sensor. The positive sign means the gas is electron-donating gas, and the negative sign means the gas is an electron-withdrawing gas [6].

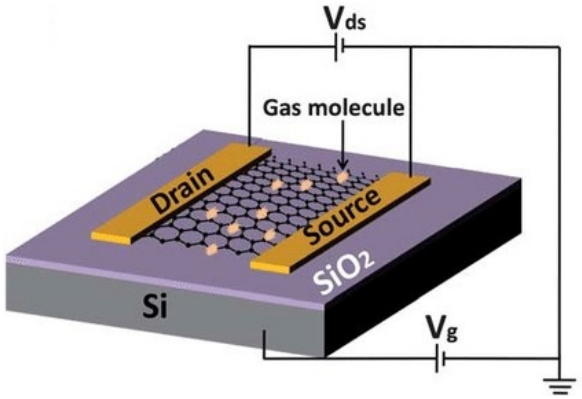

Figure 2.11: The schematic of a typical GFET gas sensor with Si/SiO_2 substrate [7]

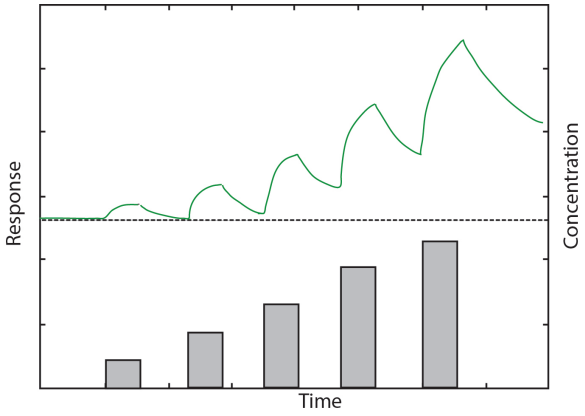

Figure 2.12: The sensor response for different gas concentrations as a function of time. The curve deviation from the baseline highlights the irreversibility of the adsorption process.

2.2.2 Performance parameters

Many parameters can serve to evaluate the performance of the gas sensors, such as the adsorption ability, sensitivity, selectivity, stability, and dynamic range. Here, the most crucial parameters of the graphene gas sensor are discussed.

- The response and response curve

  The response is defined as the normalized difference between the output signal before and after exposure to the analyte. For example, the response towards a chemiressitor can be calculated using

  $$Response = \frac{R_{Gas} - R_0}{R_0} = \frac{\Delta R}{R_0} \tag{2.5}$$

  where R_{Gas} is the resistance of the device under the presence of the target gas and R_0 is the resistance without the exposure to it.

  The response curve describes how the sensor reacts towards the target gas as a function of time. Figure 2.12 gives an example of the gas sensor response curve. Normally, a higher analyte concentration gives a more significant response.

- Selectivity

  Selectivity refers to the ability to discriminate the target gas of interest from a mixture. Selectivity can be quantified by the selectivity coefficient, which is defined as

  $$K = \frac{S_A}{S_B} \tag{2.6}$$

  where S_A is the sensitivity towards the target gas (A) and S_B is the sensitivity towards the reference gas (B).

  Selectivity is a significant parameter to evaluate the performance of a sensor. A high selectivity makes sure that the sensor gives accurate predictions of both the existence and concentration of a target gas. To improve the selectivity, it is important to understand the sensor's design and sensing mechanism with regard to the target gas.

- Sensitivity

  The sensitivity is the sloop of the calibration curve, which is the curve of the measured signals as a function of the known concentrations of the analyte.

The parameter sensitivity (S) can be defined as $\frac{R_a}{R_g}$ for the reducing gases and $\frac{R_g}{R_a}$ for the oxidizing gases, where R_a is the resistance of the device under exposure of the reference gas, normally the air, and R_g is the resistance under exposure of the target gas. Noticeably, the sensitivity resembles the slope of the calibration graph, which gives the values for the desired quantity as a function of the values of sensor output. Hence, The sensitivity can be represented as a response divided by the concentration. In general, high sensitivity also means high efficiency.

- Stability

  Stability refers to the sensor's ability to keep its characteristics constant over time. Many factors can influence stability, such as the components' aging, the change in the signal-to-noise ratio, and the decrease in the sensor sensitivity. Stability determines reliability and is, therefore, a crucial parameter, especially when the sensor is for use in a severe environment.

- Limit of detection (LOD)

  Limit of detection (LOD) is a key figure of merit for chemical-based sensors, which is defined as the minimum concentration of the analyte required to be detectable under a certain experimental condition (temperature, pressure, humidity). The linear regression model shows that when the signal is three times greater than the noise, LOD can be calculated from the sensitivity of the sensor, as reflected in

  $$LOD \geq 3 \times RMS_{noise}/S \tag{2.7}$$

  where RMS_{noise} is the noise level in the absence of the analyte gas, and S is the sensitivity.

  Noteworthily, for non-linear semiconductor gas sensors, this model is not accurate due to the nonlinearity. Readers are referred to the study of Burgues et al. who proposed a methodology to overcome the associated challenges[38].

- Response characteristics

  The response of a gas sensor is characterized by two parameters: response time (τ_s) and recovery time (τ_r). The response time is the time required for a sensor to reach 90% of the total response. The recovery time is the time required to return to 90% of the original baseline signal upon removal of the target gas.

  The response time can differ per gas type and is highly dependent on the sensing mechanism.

2.2.3 Ways to accelerate recovery

Due to the 2D structure of graphene, all atoms of a graphene layer can be considered superficial atoms, which makes the active surface area available for interactions extremely large. Consequently, compared to 1D structured materials, such as carbon nanotube, graphene exhibits shorter response time and recovery time. However, its recovery time is still very long, as shown in Figure 2.13(a).

As illustrated in Section 2.2.1, the resistance of the sensor changes following the absorption of the analyte molecules. Hence, recovering it to the sensor's baseline requires the desorption of the molecules absorbed before. To accelerate this process, plenty can be done.

A common strategy is the annealing of the device beyond the absorption temperature. Haiyang Wu et al. give an example in which the recovery time is significantly

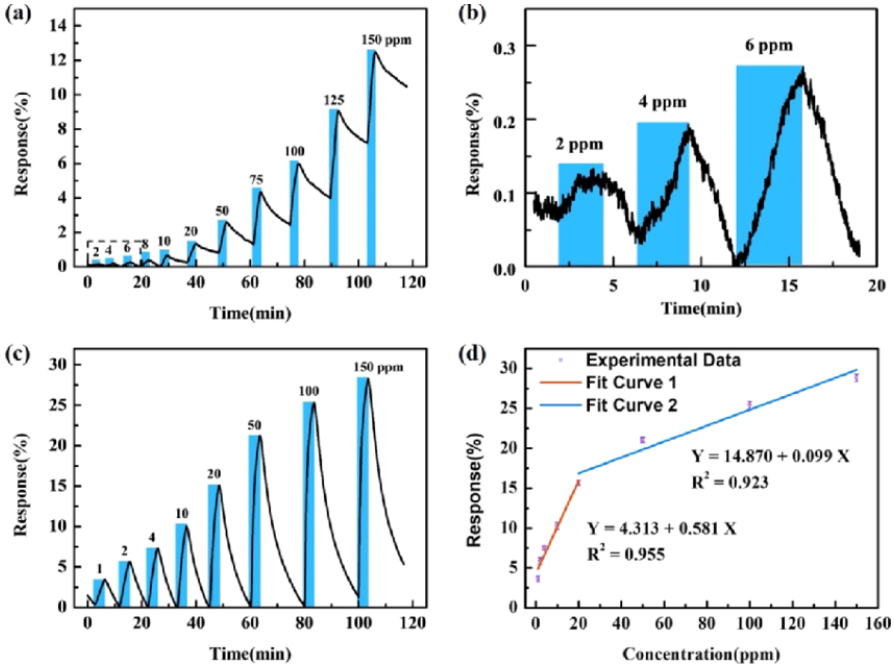

Figure 2.13: (a)The response and recovery curves of the graphene-based gas sensor under the exposure of NO_2 with the concentration from 2 to 140 ppm in dark conditions; (b)The response and recovery curves of the graphene-based gas sensor under the exposure of NO_2 with the concentration of 2, 4 and 6 ppm in dark condition; (c)The response and recovery curves of the graphene-based gas sensor under the exposure of NO_2 with the concentration from 1 to 150 ppm under UV irradiation; (d)The fit curves of the response as a function of NO_2 concentration under UV irradiation[8].

reduced after thermal annealing at a high temperature[39]. However, annealing imposes a number of technical challenges. Primarily, designing and integrating micro-fabricated hotplates for the sensor to achieve homogeneous heat distribution, and low power consumption without any compromise in size, sensitivity, reproducibility, and stability remains a difficult task. Next to it, annealing can change the properties of graphene due to the high operating temperature. Though the changes can be beneficial, e.g., an increase in the sensitivity of the sensor[39], they often introduce more additional defects to the graphene, which can reduce the mobility of the electrons[40].

Another strategy is ultraviolet light (UV)[41]. As depicted in Figure 2.13(c), the recovery process is accelerated under UV irradiation compared to Figure 2.13(a). However, unlike the integration of a hotplate to realize high-temperature annealing, UV irradiation gives a higher demand for the sensing condition.

As can be seen, each strategy comes with advantages and disadvantages. Therefore, finding a suitable way for reducing the recovery time remains a topic where more investigation in needed.

2.3 METAL/METAL OXIDE NANOPARTICLES

Though many efforts have been applied to improve the performance of graphene-based gas sensors, some of the challenges have not yet been fully addressed, such as poor selectivity, the absence of saturation of signal, and the long recovery time. One way to improve the selectivity is to increase the surface-to-volume ratio of the sensing layer, which can provide more adsorption sites than pristine graphene. It is shown that decorating an epitaxial graphene surface with metal oxide nano-

layers can increase the sensitivity and selectivity of the sensor[42]. Not only the metal oxide nano-layers but also metal or metal oxide nanoparticles can also impart selectivity[43].

This section first gives an overview of the functionalization of graphene, and its various implementations, alongside a number of representative researches. Next, spark ablation, a physical process used to generate pure nanoparticles, is introduced. Finally, the sintering process which can change the nanoparticle morphology is discussed.

2.3.1 Functionalization of graphene

Recently, it has been demonstrated both theoretically and experimentally that functionalization is among the most promising technologies that can improve graphene's sensing properties. The functionalization of graphene can be achieved in multiple ways, including nanoparticle decoration, with noble metals or metal oxides, nanoparticle decoration, including metals and metal oxides, quantum dots (QDs) decoration, substitutional doping, and conductive polymers decoration[44].

Noble metal nanoparticle decoration does not only enhance sensing by increasing the active surface area, but also through the analytic effects, which essentially promotes the electron transfer between the graphene and the analyte gases. Within this category, low work function metals emit thermions at low temperature, and high work function metals take effect differently. Decorating with low work function metal nanoparticles hinders graphene's sensitivity towards electron-withdrawing gases because the electrons are transferred from the metal to graphene, which forms a Scotty junction in between that blocks electron withdrawing[45].

An example of low work function metal is silver (Ag), which shows a strong enhancement effect of the sensor response towards NH_3[46], an electron-donating gas. Typically, the enhancement effect is greatly determined by the surface coverage rate. For the detection of NH_3, the enhancement by Ah only takes effect when the surface coverage rate is not too low nor too high (below 4.9%). In the former case, NH_3 gas molecules mainly react with raw uncovered graphene, which has little difference to the sensor without functionalization. In the case where the surface coverage is too high, the aggregation of the Ag nanoparticles reduces the surface area, hence decreasing the active site for gas interaction[47].

On the other side, high work function metals, such as Au, Pt, and Pd, form an ohmic contact between metal and graphene. Eriksson et al. have demonstrated that the epitaxial graphene decorated with Au and Pt NP layers has a shorter response time, higher sensitivity, and higher selectivity[48]. This is because decoration largely changes the graphene's band structure, and consequently the carrier concentration. Such outcomes highlight that just simple nanoparticle decoration can lead to big changes in the band structure, hence the carrier concentration of the graphene.

Next to the noble metal nanoparticles, metal oxide nanoparticles can as well boost the device performance. Copper oxide (CuO), titanium oxide (which spontaneously forms oxides with various degrees of valence states), and aluminum oxide, each of which, through decorating, can strengthen the sensing performances of different analyte gases. For instance, Zhao et al. demonstrated that CVD graphene decorated with titanium oxides nanoparticles exhibit an increased response under visible light compared to pristine graphene. Similar to the decoration with noble metal nanoparticles, controlling the morphology and the coverage of the metal oxide nanoparticles is essential[44].

Another material that can effectively increase graphene's active surface area is QD. In recent years, QDs have gained lots of interest. Many of the latest researches concerned decorating rGO or CVD graphene with QDs[49] and have seen improvements in the response time, sensitivity, and selectivity.

Meanwhile, CP is another decoration material that, possesses unique advantages, including chemical robustness, high sensitivity, and the ability to form a strong $\pi -$

π stacking with graphene (which leads to a low charge carrier transfer in between). Additionally, some types of CP have high transparency and excellent reliability, which makes it an ideal material for low-cost portable setups. The most popular and investigated CP used for decoration is polyaniline (PANI). Similarly, research has proven that combining CP with graphene can reduce the response time and improve the sensitivity[44].

The theoretical knowledge shows another potential way to achieve high sensitivity and selectivity is to introduce the dopants to the surface of graphene. Substitutional doping replaced the carbon atoms occupying the sites with some other atoms having different valence electrons, resulting in changes in the electron configuration and the carrier density. A wide selection of atoms can be used as candidates, such as silicon boron, phosphorus, and sulfur. For example, Si-doped graphene shows higher adsorption energy compared to pristine graphene under the exposure of NO_2[50]. P-doped graphene exhibits a high sensitivity towards H_2S, which, on the contrary, has a relatively weak interaction with pristine graphene[44].

In reality, environmental gas always has a complex composition, which demands excellent sensitivity and selectivity of the sensors. For this reason, functionalization is extraordinarily helpful and crucial.

2.3.2 Spark ablation

Evidently, functionalization needs high quality NPs. Spark ablation is a technology that generates pure particles under controlled settings, invented by Andreas Schmidt-Ott in 1988[9]. Its popularity owes partially to the process being entirely physical, and thus environmentally friendly. On top of it, it features fast quenching and fast dynamics, making it a perfect choice for the production of nanoparticles[51].

Technologically, spark ablation utilizes the electrical discharges induced between two electrodes, namely the spark plasma, to ablate NPs from the material of the electrodes[9]. Under an inlet gas flow mixed with a small vapor cloud produced by a spark, the nanoparticles are brought together and reach extreme supersaturation when they spontaneously cool down. In the end, the condensation effect coagulates the NPs to larger particles, which results in atomic clusters.

Figure 2.14 shows the principle of an electronics circuit of a spark discharge generator, a common setup for spark ablation based on a simple RCL circuit with three switches and a glow discharge supply. L usually equals the inductance of the wiring, while R is predominantly the resistance of the spark gas when no series resistance is added. When the switches S_2 and S_3 are closed and S_1 is open, the capacitance C is charged. Inversely, when S_1 is closed and S_2 and S_3 are open, a spark discharge occurs. Noteworthily, two currents can flow when the circuit is activated: the glow current produced by the spark discharge generator, which is weak; and the spark current stimulated by the pulsing network containing the parallel capacitor, which lasts a short time bit is highly energetic. Because of the need for high energy, the ablation is induced only by the latter[9].

Spark ablation can easily scale up to mass production, which is primarily achieved through the control of the voltage, or the spark energy. The production rate can be estimated as the product of the spark frequency (up to 20 kHz) and the spark energy.

As a last remark, spark ablation is a highly versatile and flexible technology, in the sense that different combinations of the end particles' size, shape, composition, and structure can be obtained through modifications in the process setup. For example, round singlet particles and agglomerate particles can be acquired by changing the temperature in the growth zone. Oxides or compounds can result by introducing certain gases to react with the formed particles. Additionally, a mixed composition of the particles is made feasible by using for each electrode a different metal, or taking one step further, using alloys for the electrodes. Lastly, a core-shell structure

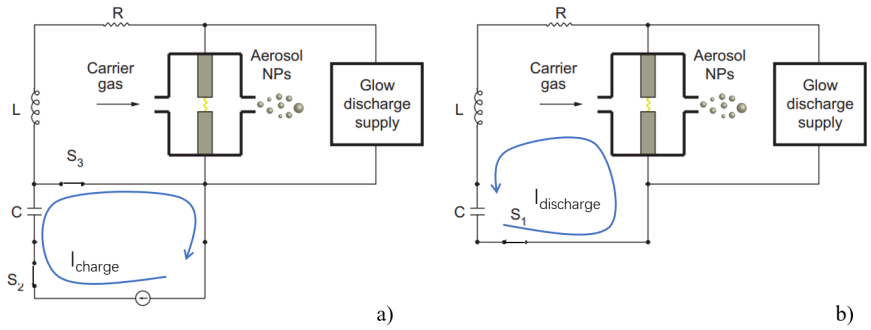

Figure 2.14: The principle switching circuit for the spark ablation[9]: a) When the switches S_2 and S_3 are closed and S_1 is open, the capacitance C is charged; b) when S_1 is closed and S_2 and S_3 are open, a spark discharge occurs.

of the particle cluster can be realized by arranging the spark discharge generators in series.

2.4 SENSOR ARRAY

The gas sensor, which is one kind of chemical sensor, normally can not achieve the required selectivity. The sensors will be rendered ineffective due to many effects in the real-work environments, for example, the interfering species, varying temperature, and humidity[43]. This limitation originates from the fundamental principles of the sensing mechanism, which cannot be eliminated completely. However, this limitation can be reduced by many methods, and applying a sensor array is one of the promising ways.

A sensor array is to combine many sensors in a group to collect information under test. It consists of different sensors with overlapping sensitivity toward different gases to gather signals from multi-component gaseous mixtures[52]. The gas sensor array is inspired by the biological olfactory systems and is constructed by Persaud & Dodd in 1982[53]. It states that each individual channel inside a sensor array does not need to be perfectly orthogonal to other channels. Instead, the cross-sensitivity of the gas sensor array is unavoidable, which means that the chemicals can interact to give different signals from a component in a mixture.

The selection of the sensor and the structure of the sensor array influence directly the performance of the sensor array. Not only the chemiresistors, but also the electrochemical sensor, MOSFETs, and mass-sensitive devices such as quartz crystal microbalance (QCM) devices can all be used as the channels inside a sensor array. In addition, both heterogeneous and homogeneous sensor arrays are feasible, while the former is more versatile and the latter one is simpler. Currently, most of the sensor arrays are designed application-oriented, which gives them bad applicability. The way to improve it is still under-investment.

3 EXPERIMENTAL METHODS

The research and development of a graphene gas sensor array involve several fabrication and characterization techniques. In this chapter, an overview of the fabrication process and data collection is given. It starts with the gas sensing device flowchart based on MLG, including the MLG growth, followed by the functionalization process. Then, the gas measurement setup and data acquisition process are illustrated.

3.1 SENSOR FABRICATION PROCESS AND FUNCTIONALIZATION

This section gives an introduction to graphene growth firstly. Then the flow chart used to fabricate the chemiresistor sensor is discussed. Finally, the functionalization of the graphene by different nanoparticles is illustrated.

3.1.1 Graphene growth process

As discussed before, there are many graphene growth methods, and in this project, a transfer-free wafer-scale CVD graphene fabrication process is applied[10].

Before the deposition of the graphene, a thin film of Mo is sputtered on the substrate. Mo is chosen as the substrate material for graphene growth because of its high melting point, which is 2623 °C. The chemical vapor deposition (CVD) procedure of the graphene needs a temperature higher than 1000 °C. Additionally, the Mo layer can be dry etched with SF_6 in combination with a photo-lithographic resist layer, which makes the graphene can be pre-pattern to micron dimension[10].

After that, the graphene is deposited on the Mo catalyst using an AIXTRON BlackMagic Pro, which is a commercially available device for graphene growth. The recipe temperature has a big effect on the quality and the layer of the graphene. In this fabrication process, the bottom heater of the chamber is set to 950 °C and the top one is set to 1050 °C. First, a pre-annealing of Mo is done to remove oxidized Mo on the surface for 20 minutes. Then CH_4 is used as feedstock in the chamber for graphene growth.

The majority of the transfer methods also synthesize graphene by CVD, but with Ni as the substrate for multi-layer graphene and Cu for mono-layer. However, because of the need for the application, the transfer of the graphene from the metal substrate to another substrate is required. Usually, graphene is removed from the etchant and rinsed with demi-water. Then either dry transfer or wet transfer can be used, the latter takes place in water or another solvent. Normally, the transferred methods will leave residues on the graphene layer. The residues can be a severe problem for the sensor study. With the residue, the segment resistance range from 200 to $>$ 800 kΩ, and the resistance distribution is stochastic in nature[54]. To test and explore the performance of the gas sensor, a repeatable test platform is necessary. However, the residues on graphene can lead to random contamination and therefore a random sensor response.

But there are some works claiming residue-free transfer. Samg-Min K. et al. proposed a residue-free transfer method for the fabrication of suspended structures

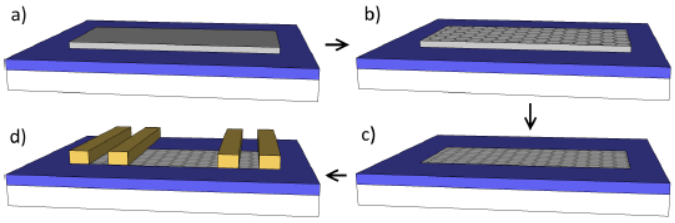

Figure 3.1: The schematic overview of the fabrication process: a) deposition and patterning of Mo layer on SiO_2 substrate; b) graphene by CVD on Mo; c) Mo layer etched by wet etching; d) deposition of the electrodes with Cr/Au using a lift-off process[10].

by using perforated polymer templates[55]. But of course, other complications can arise, like residue contamination.

The transfer-free graphene synthesis method used in this project is a semiconductor manufacturing-compatible approach. Additionally, this approach also allows the patterning of the graphene layer.

3.1.2 Flow chart

For the fabrication of the sensor, single-side polished, 500μm thick, 4-inch silicon wafers are used. All the useful structures were fabricated on the front side of the wafer. The wafers are p-type and 1-0-0 orientation. The fabrication was done in Else Kooi Laboratory (EKL) at TU Delft.

After the zero layer process, which includes the etching of alignment marks, the thermal oxidation procedure is followed to form a SiO_2 layer with the target thickness of 90 nm at the temperature of 1050 °C to insulate the graphene structures from the wafer. Then a thin film of Molybdenum with the thickness of 50 nm is sputtered at 50 °C on the SiO_2 layer. Mo is chosen as the catalyst for the selective growth of graphene. After the photo-lithographic layer patterning, Mo is then dry-etched using Trikon Omega 201. Graphene is grown on patterned Mo using LPCVD by AIXTRON BlackMagic at 1000 °C. Then another photo-lithographic layer is used to pattern the chromium and gold electrical contacts deposited by e-beam evaporation. A lift-off step is used then to remove the photo-resist together with the excessive metal part. After the dicing using the DEMCO machine, the Mo layer underneath the graphene is etched one by one using hydrogen peroxide to form graphene resistors. The schematic of the fabrication processes is illustrated in Figure 3.2.

3.1.3 Nanoparticle functionalization

To functionalize the graphene, adding nanostructures to its surface is a promising method. Nanoparticles are generated using nanoparticle generator from VSParticle B.V. by the process of spark ablation. After that, they are deposited using the nanoparticle printer as shown in Figure 3.3.

In this project, there are totally four metal/metal oxides involved. Gold (Au) and platinum (Pt) are noble metals, which means they are generally resistant to corrosion. Hence, the nanoparticles are in the raw form, Au nanoparticles, and Pt nanoparticles. However, for Cu nanoparticles and Fe nanoparticles, once they are exposed to the air, they will be oxidized immediately.

To optimize the nanoparticle functionalization, the printing parameters need to be varied to get various nanoparticle densities. Because these metals have different deposition rates, the voltage and current of the nanoparticle generator need to be adjusted. Additionally, the print speed is a significant parameter that affects the nanoparticle density. High print speeds give lower density. The combinations of

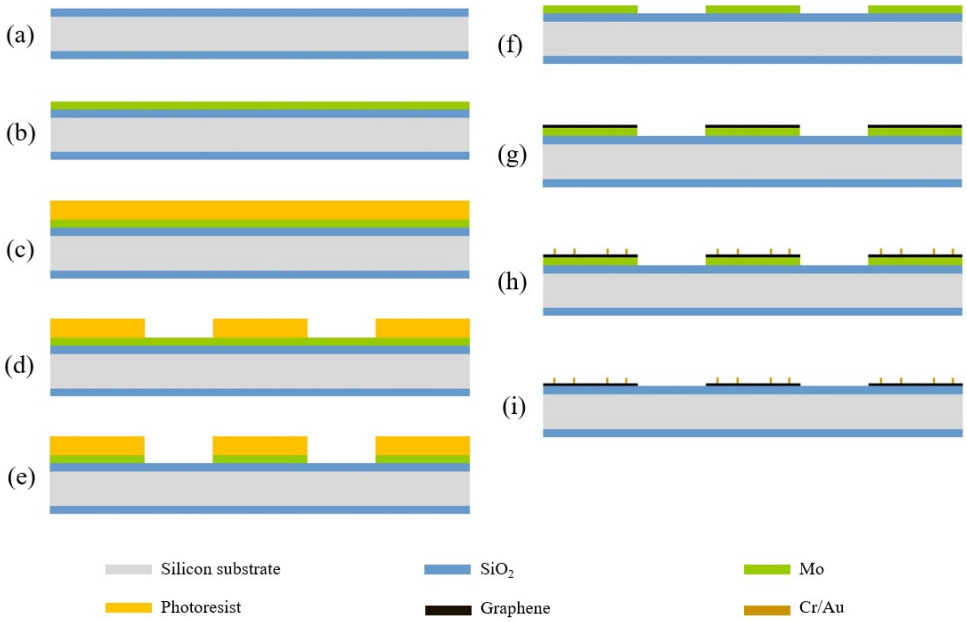

Figure 3.2: The schematic of the wafer cross-section of the flow chart.

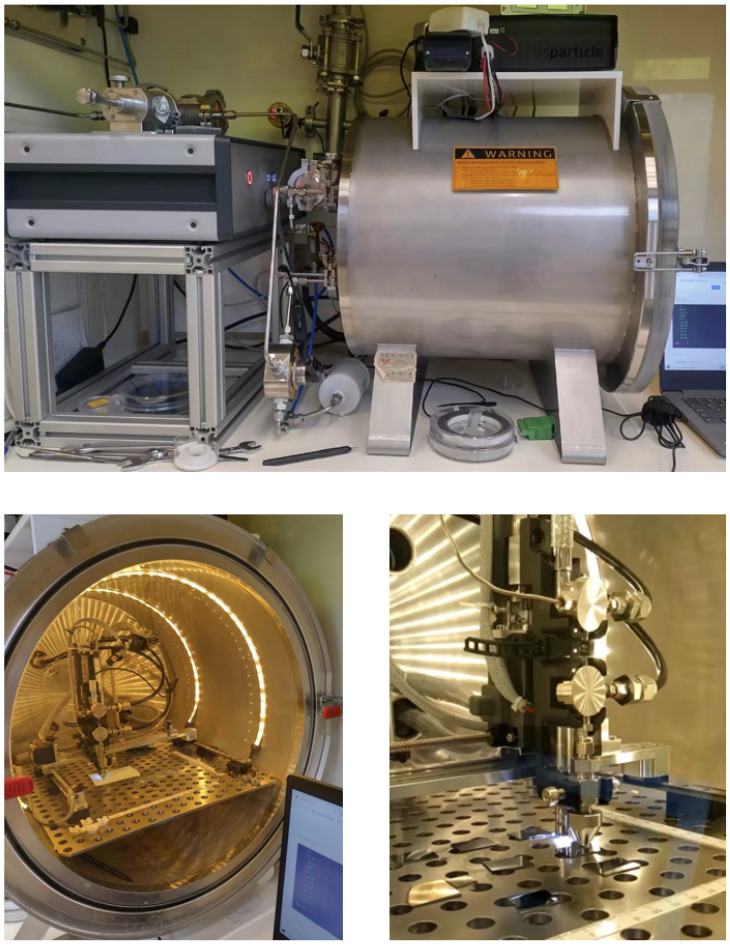

Figure 3.3: The image of the printer and the nozzle inside.

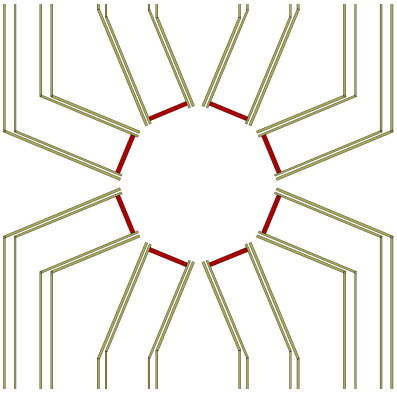

Figure 3.4: The diagram of the alignment of graphene stripes in the device.

various G1 power and various print speed contribute to different densities. In this project, mono-layer nanoparticle coverage needs to be avoided, because nanoparticles are only used as the functionalization material, the real sensing material is the graphene layer underneath. A mono-layer nanoparticle can be regarded as a short circuit in this case.

Besides, due to the small size of graphene stripes, the printing feature needs to be small as well. As shown in Figure 3.4, The red rectangles are the graphene stripes with the size of 200 μm x 20 μm. To make the printing feature as small as possible, the nozzle size needs to be small and the printing height between the nozzle and substrate needs to be small as well. There are three different nozzle sizes. In this work, the smallest nozzle (0.08 L/min) is used. The printing height is 0.3 mm, which can give tiny features.

3.2 GAS MEASUREMENT SETUP

The goal of this project is to design a sensor array that includes multiple gas sensors exhibiting a different response toward the target gas.

To build such a setup to do the gas sensor tests, a gas generator is needed. The tests are performed towards NO_2 and H_2O and all the experiments are carried out using N_2 as the buffer gas at room temperature (around 23°C).

The maximum number of graphene stripes in one device is eight. To acquire the sensing data from these eight stripes continuously, either eight source measure units (SMU) or one source measure unit with a multiplexer switching between these eight stripes is needed. Obviously, using only one source measure unit together with a data acquisition multiplexer is more concise. In this study, a measurement setup with one SMU and one multiplexer is established to execute the data acquisition work.

3.2.1 Hardware

To generate the target gas vapor, a setup equipped with an Owlstone flow controller (OFC-1), a vertical Owlstone vapor generator (V-OVG), and an Owlstone humidity generator (OHG-4) is used. All these three units are integrated in a way shown in Figure 3.5 a), but with a V-OVG in middle instead of OVG-4. Among them, OHG is a versatile humidity generator that is used to produce a range of relative humidity concentrations from 1 to 90%RH (±1%). OVG is a versatile platform for the calibration of industrial and scientific gas sensors. Using permeation tube technology, a V-OVG system can replace multiple gas cylinders resulting in significant cost and space savings. OHC is used in conjunction with OVG to generate a wide range of

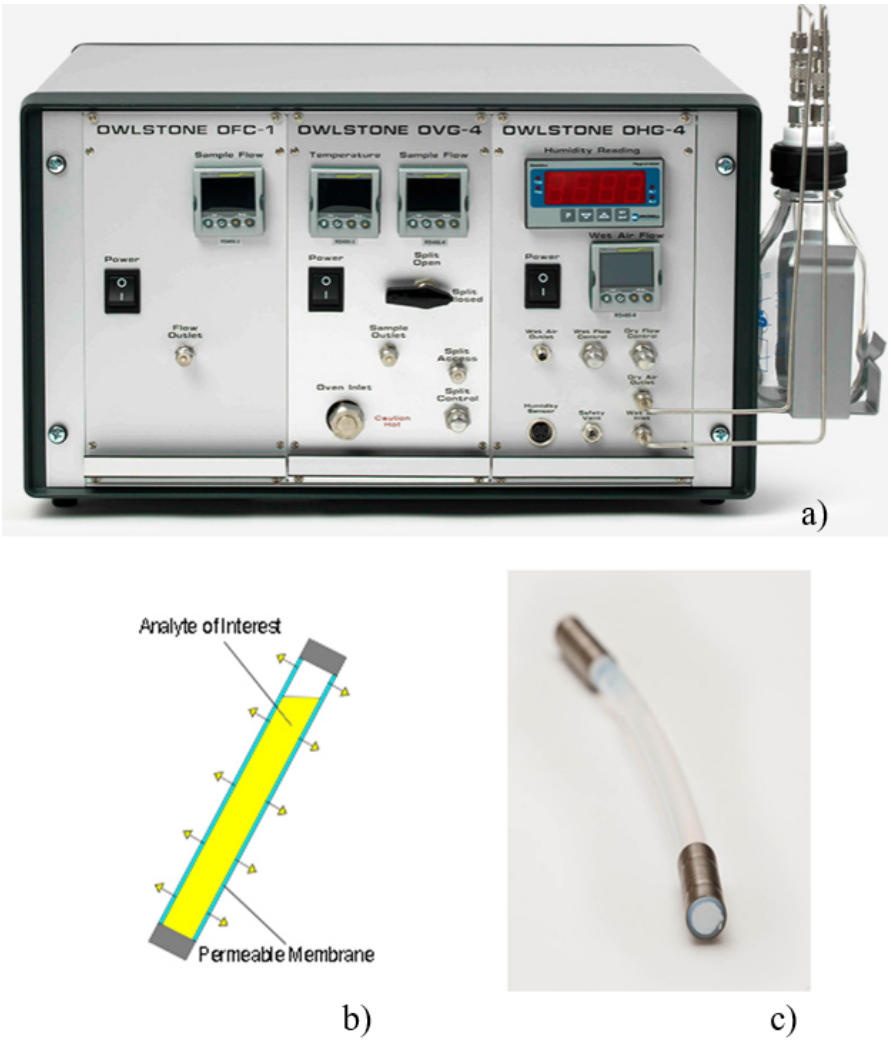

Figure 3.5: a) Gas vapor generator includes a humidity generator (OHG-4) and a flow controller (OFC-1), and a vapor generator unit (OVG-4); b) Permeation tube schematic; C) Permeation tube.

vapor standards, and OFC is integrated into the system for secondary dilution and ultra-low concentrations.

A permeation tube is a sealed cylinder of a permeable material (such as PTFE) with an analyte of interest inside, as shown in Figure 3.5 b) and c). The target gas will very slowly permeate through the walls of the tube, at a rate governed by temperature. The humidity used in this study is generated directly by OHG, and NO_2 is generated by OVG and the NO_2 tube, which has a permeation rate of 1340 ng/min at 50°C. Combining with the molar mass, sample flow rate, and exhaust flow rate, different concentrations of the gas flow can be calculated.

After the generated gas flows into the chamber, the data collection work needs to be done. The SMU used in this project is a Keithley 2612B. There are two channels that can work independently, and the output power can reach 200W. The source voltage range is $\pm 200\ mV$ to $\pm 200\ V$, and the source current range is $\pm 100\ nA$ to $\pm 10\ A$. The resistance measurement range is from 500 nΩ to 100 TΩ. As for the multiplexer, a Data Acquisition Switch Unit 34970A and a Data Acquisition Multiplexer 34901A from Keysight are used. There are totally 22 channels in 34901A. Because there will be a maximum of eight graphene stripes measuring at the same time, one 34901A multiplexer is enough.

The whole setup is connected as shown in Figure 3.6. The diced chip will be put in the PCB, which is specially designed according to the size of the chip. Then

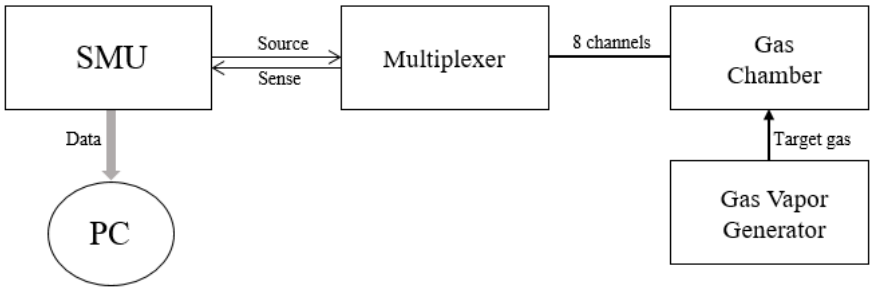

Figure 3.6: The flow chart of the measurement setup.

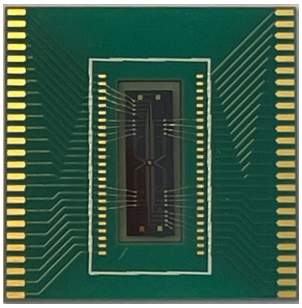

Figure 3.7: The picture of the chip wire bonded on the PCB.

they are connected using wire bonding as shown in Figure 3.7. The gas chamber consists of the gas inlet and outlet terminal, three thermal couples, and a hot plate, as shown in Figure 3.8. There are fifty needles designed for the specific PCB to collect data in total. These needles are then connected to the multiplexer through a fifty-one-wire connector. The selected signal is then connected to the SMU to finish the measurement.

To reduce the effect of the test lead resistance, the four-wire resistance measurement method is used in this project. Figure 3.9 gives an illustration of how four-wire measurement works. With this configuration, the test current (I) is forced through the test resistance (R) via one set of test leads, while the voltage (V_M) across the DUT is measured through a second set of leads (sense leads).

3.2.2 Software

To automatically measure the resistance of graphene stripes sequentially, LabView is used in this project to control the SMU and the multiplexer. LabView is a graphical programming environment that engineers use to develop automated research, validation, and production test systems. There are several advantages to using LabView. Firstly, there are thousands of available analysis functions in LabView, including the

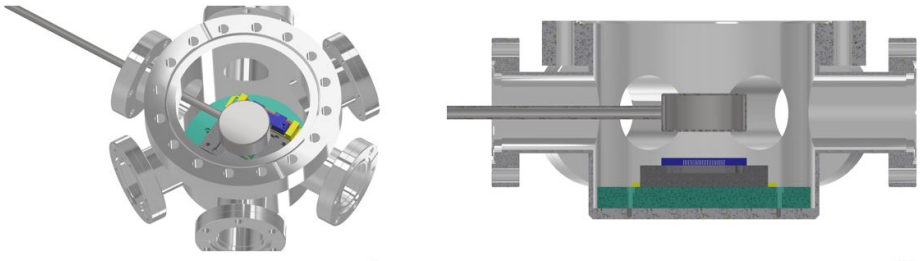

Figure 3.8: The sketches of the whole get setup.

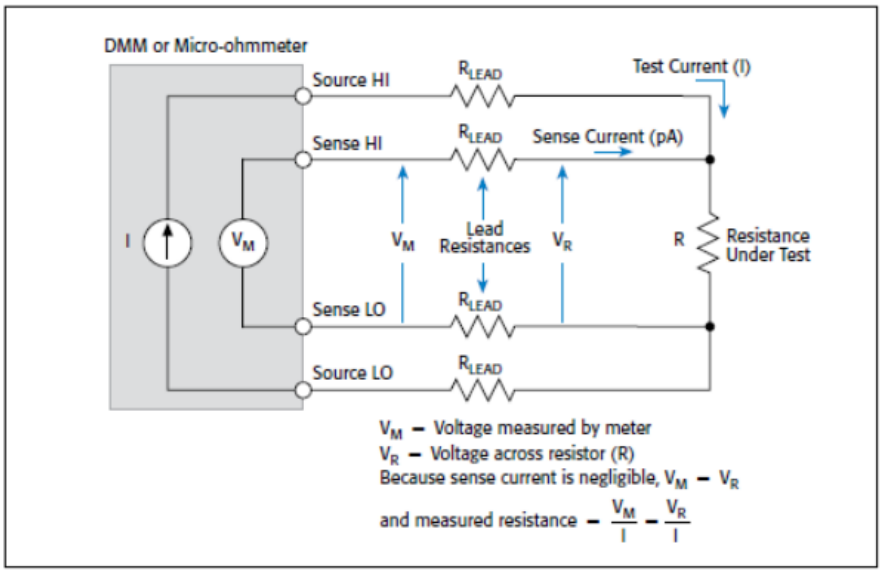

Figure 3.9: Four-wire resistance measurement configuration[11]

configurable, interactive display elements. Secondly, LabView has many drivers for automating instrument and data acquisition hardware. Finally, the connectivity between LabView and other language or industry-standard protocols is good, which makes LabView a compatible tool. which can reduce the programming time and make the design intuitive.

The LabView script of this project can be mainly divided into 4 parts as shown in Figure 3.10. The function of part 1 is to initialize the SMU and the multiplexer. The configuration of the source and sense, including the range, level, and limit, the configuration of the channels, and the configuration of the 2-wire measurement or 4-wire measurement are defined here. All of these used functions are included in the driver of the instruments. Part 2 is to switch between different channels. The open and close function from the multiplexer (34970a) driver reacts according to the number they are connected to. Then part 3 manipulates the SMU to execute the corresponding measurements. Channel A and channel B can work independently. A 500 ms delay is added here to make sure the measurement is finished. Finally, the measured data is exported to a text file, which is easy for further data analysis as shown in part 4.

The clear and complete LabView Script for an 8-channel device is shown in Appendix A.

3.3 DATA HANDLING

The switching frequency of the multiplexer is 2 Hz, which means there are two data points saved per second. Additionally, the gas tests usually last several hours, which makes the data set large. In this project, Origin is used to make the figures, which can import the data with the graph form. Hence, writing a code with the capability of converting the exported text file to an Excel file, filtering out the redundant data, and calculating the needed parameter for the plot will reduce the time for data analysis.

A Matlab code is created to perform this task. First, the code will read the text data file in the given destination. Then all the redundant and abnormal data will be filtered out (there can be some extremely large data points due to the relay), after which the data will be classified according to the channel number. This step is to make sure the data from different stripes will not affect each other. Then the data

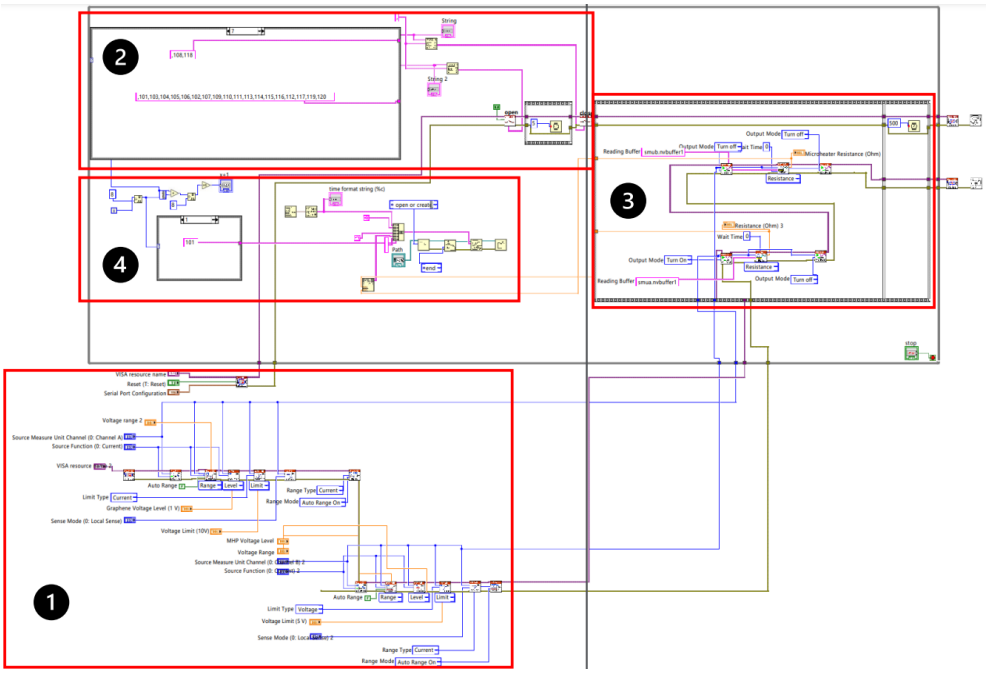

Figure 3.10: A screenshot of the LabView script.

analysis parameters are calculated: the mean value, the standard deviation, and the response. The gas concentration needs to be inserted manually, and this value will also be exported. Finally, all the data will be exported in an Excel file, and the name of the file can be self-defined.

4 MATERIAL AND DEVICE CHARACTERIZATION

This chapter gives the characterization of both the sensing material and the gas sensor device, which ensures the high quality of the design and the manufacturing process.

4.1 MATERIAL CHARACTERIZATION

Evidently, the morphological properties of graphene together with the decorative nanoparticles determine its performance as a gas sensor material. In light of this, a number of analysis techniques were applied to investigate the physical properties of the sensing material. These include Raman Spectroscopy, Scanning Electron Microscopy (SEM), and Atomic Force Microscopy (AFM).

4.1.1 Raman spectroscopy

Introduction to Raman Spectroscopy

Raman Spectroscopy is a non-destructive chemical analysis technique, which uses a beam of high-intensity light to measure the vibrational energy modes of a sample. The light is scattered differently by different molecules. Normally, three ways of scattering take place when the light hits the molecule, as shown in Figure 4.1.

The majority of the scattered light has its energy unchanged after the interaction with a molecule or solid material, which means the wavelength is equal to the laser source, as depicted in green in Figure 4.1. In solids, the interaction is with photons in the crystal lattice and the energy of the material is not altered. This is called Rayleigh scattering and normally provides little useful information. Next to it, a small amount of light has the wavelength changed after scattering because of a transfer of energy between the molecule and the scattered photons. Two types of changes can happen. If the molecule gains energy from the photons, the wavelength of the scattered light will increase, which is called Stokes Raman scattering represented by the red wave in Figure 4.1. Conversely, the molecule may lose energy and lead to a decreased wavelength of light. This is called Anti-Strokes Raman Scattering, shown in blue in Figure 4.1. According to statistics, the Stokes Raman scattering is more likely to take place and thus more often observed in a Raman Spectroscopy.

A Raman spectrum tells the light intensity in the function of the wavelength shift, or Raman shift. Typically, the intensity is centered around several wavelength shift positions, resulting in peaks in the spectrum, as shown in Figure 4.2. These peaks indicate the corresponding molecular bond vibration as well as the group of the bonds.

In the case of graphene, three peaks can usually be observed, conventionally known as the D band at around 1350 cm^{-1}, the G band at around 1582 cm^{-1}, and the G′ band, also called the 2D band, at around 2700 cm^{-1} using the laser excitation at 2.41 eV, as depicted in Figure 4.2.

Among the three featured peaks, the D band and G band are good indicators of the disorders and defects of the graphene. Often, the level of imperfection can be estimated by calculating the $I(D)/I(G)$ value, or deducting the full width of half

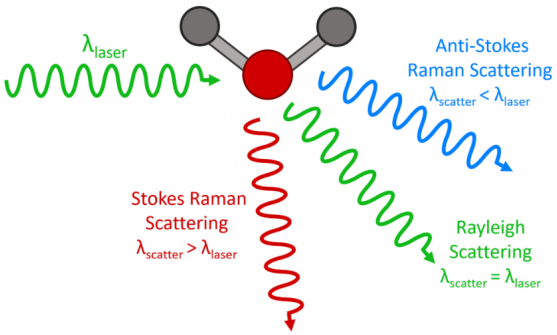

Figure 4.1: Three types of scattering processes that can occur when light interacts with a molecule[12].

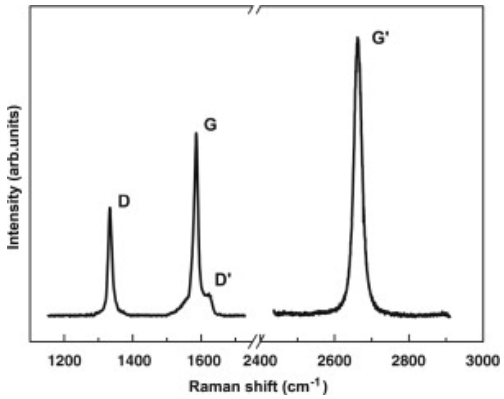

Figure 4.2: The Raman Spectrum of graphene, which shows the main Raman features, the D, G, G′ band taken with a laser excitation energy of 2.41eV[13].

maximum of the G band ($FWHM(G)$). Noteworthily, two categories of defects can be present in graphene: the ones related to sp^2 rings, and the ones associated with chains, including the perfect zigzag edges, charged impurities, intercalates, uniaxial and biaxial strains. While only the former group can induce the peak at the D band, what at the G band changed for both groups[56]. In practice, combining the $I(D)/I(G)$ value and the $FWHM(G)$ gives a comprehensive image of the amount as well as the type of defects[56].

On the other side, the 2D band is correlated with the number of layers of graphene. Changes in the layer number, or graphene turning into graphite, can significantly influence the light intensity there. Often, the $I(D)/I(G)$ value is calculated to predict such variation. A value lower than 1 indicates multi-layer graphene. Additionally, the number of Lorentzians and their energy, width, and intensity can give an indication of the number of layers. Graphene in this study is believed to be turbostratic because it can be fitted with one Lorentzian, which gives evidence that it is multi-layer[57].

In this study, the Raman Spectroscopy was performed for the graphene at each major stage during the fabrication, using a Renishaw inVia Raman microscope with a 633 nm laser. The Raman spectrum was taken in the range of 1100 cm^{-1} to 3200 cm^{-1}. Each stage was given multiple measurements, from which an average can be taken to deduct more concrete information.

Raman spectrum after graphene growth on Mo

The top spectra in Figure 4.3 display the acquired Raman spectrum of the graphene directly after the CVD deposition on Mo. There is a clear D peak in the spectrum, which means the graphene grown by CVD is defective. The $I(2D)/I(G)$ value is around 0.618, implying that the graphene is multi-layer.

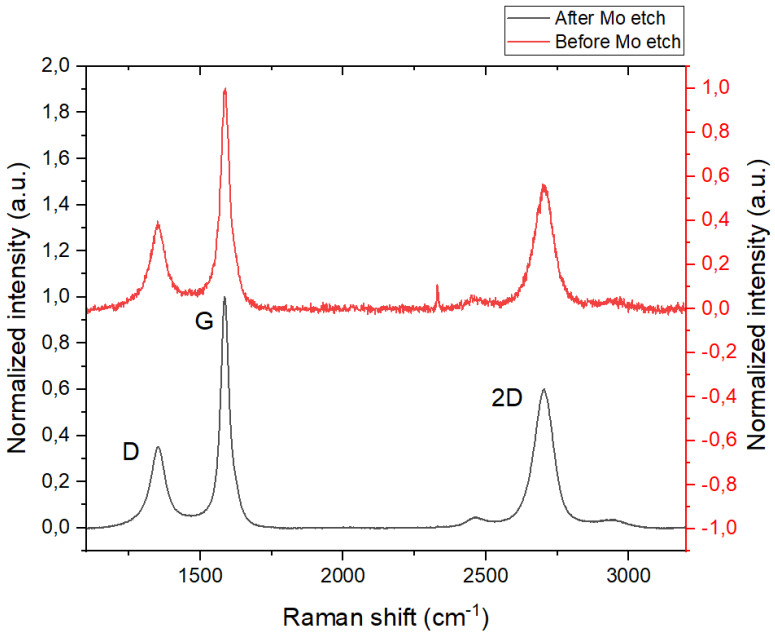

Figure 4.3: The comparison of the Raman spectra of the graphene before and after the Mo etching, normalized to the G peak.

Raman spectrum after Mo etch

The bottom spectra in Figure 4.3 display the Raman spectrum of the graphene landing on the SiO_2 substrate after Mo etch.

Figure 4.3 compares the Raman spectra before and after Mo etch. An observable difference is that the spectra before Mo etch have more noise. This is due to the signal from the graphene being suppressed when on Mo, while on SiO_2 it becomes much larger. Next to it, the $I(D)/I(G)$ peaks are identical before and after release, which indicates little change in the defect density. Similarly, the $I(2D)/I(G)$ value remained nearly unchanged, implying that the layer number of the graphene was almost unaltered.

Figure 4.4 plots $I(D)/I(G)$ value against $FWHM(G)$ before and after the Mo etch. Because the ratio of $I(D)/I(G)$ and $FWHM(G)$ are both related to the defect density, they are proportional to each other. As discussed before, $FWHM(G)$ is sensitive to all types of defects, including the sp^2 rings and chains. On the other hand, $I(D)/I(G)$ is only sensitive to the defects in the rings[56]. The red data points of the graphene, which show the Raman results after the Mo etch, have a higher position in the figure, compared to the black data points exhibiting the Raman results before Mo etch. After Mo etching, the values of $I(D)/I(G)$ are increased. This can be related to the unbounded C-bond. After the graphene grows on Mo, part of the graphene atoms are bonded with the MoC catalyst. And after Mo etch, they are detached and left more unsaturated bonds[58].

Raman spectrum after nanoparticles deposition

The Raman spectrum of the graphene after the Au-NPs functionalization is displayed as the red curve in Figure 4.5. While the spectrum before the deposition is displayed in black for reference, the two curves are alike. The average $I(D)/I(G)$ value of the graphene before Au-NPs deposition is 0.358, and the value after the Au-NPs deposition is 0.353, which is almost identical, implying that Au-NPs had hardly affected the defect density of the graphene. A possible explanation is that Au-NPs are small and sparsely distributed and they don't have sufficient kinetic energy to cause defects.

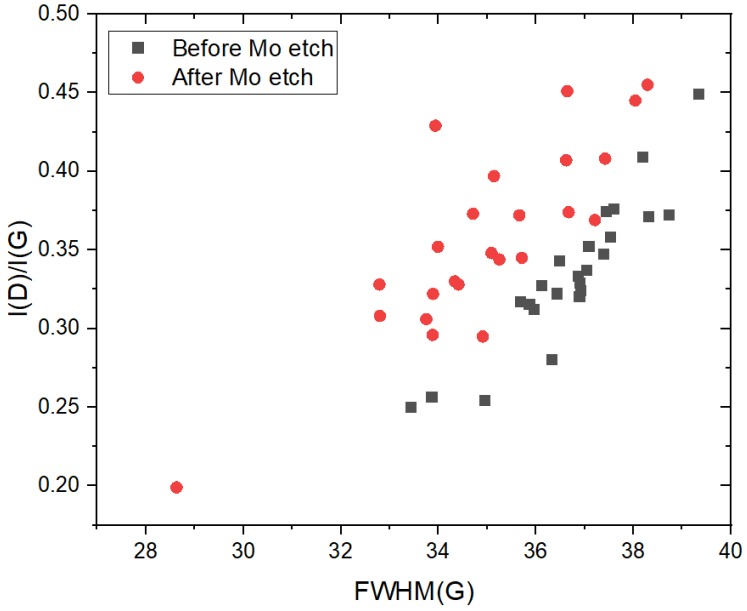

Figure 4.4: $I(D)/I(G)$ against $FWHM(G)$ for the graphene before and after Mo etch.

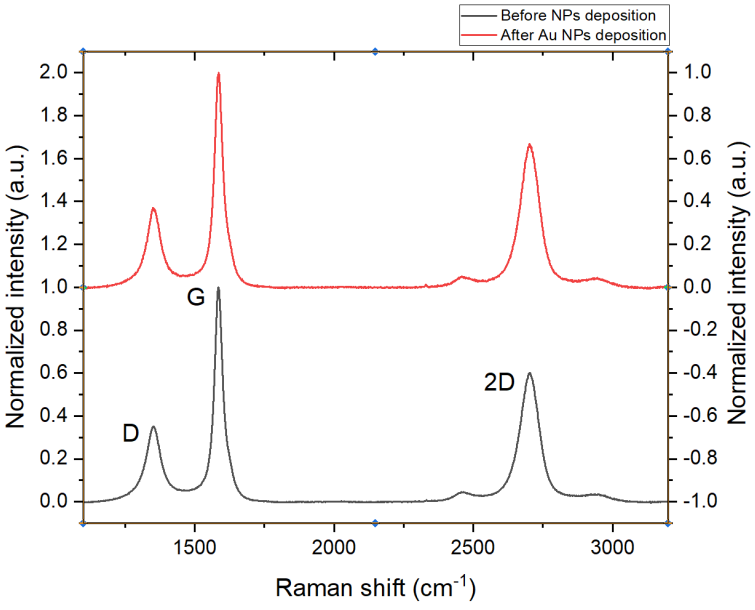

Figure 4.5: The comparison of the Raman spectra of the graphene before and after Au NPs deposition, normalized to the G peak.

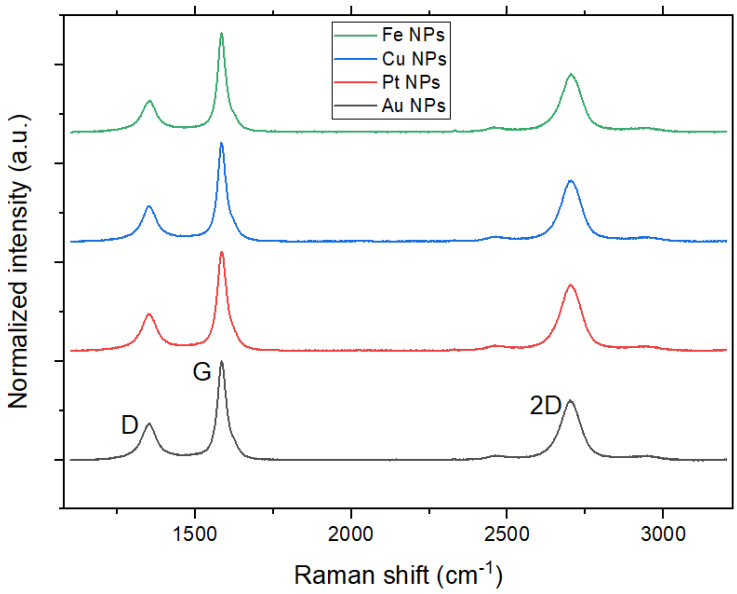

Figure 4.6: The comparison of the Raman spectra of the graphene after four different nanoparticle deposition, normalized to the G peak.

	without NPs		with Au-NPs		with Pt-NPs		with Cu-NPs		with Fe-NPs	
	M	SD	M	SD	M	SD	M	SD	M	SD
$I(D)/I(G)$	0.358	0.05918	0.353	0.04946	0.423	0.0681	0.262	0.0598	0.285	0.03064
$FWHM(G)$	34.99	2.057	35.84	1.5046	37.89	2.321	31.17	1.391	32.03	0.737
$I(2D)/I(G)$	0.635	0.0617	0.663	0.0767	0.686	0.0741	0.615	0.0604	0.661	0.103

Table 4.1: Details concerning the average $I(D)/I(G)$, $FWHM(G)$, and $I(2D)/I(G)$ values of the graphene decorated with nothing and other four metal nanoparticles. M is the mean value and SD is the standard deviation.

The Raman spectrum of the MLG deposited with Au-NPs, Pt-NPs, Cu-NPs, and Fe-NPs are put next to each other in Figure 4.6. As in the case of graphene deposited with Au-NPs, the three nanoparticles, Pt-NPs, Cu-NPs, and Fe-NPs, as displayed in the above figures, did not change the Raman spectra of the pristine graphene.

Furtherly, the three parameters were calculated per nanoparticle type, whose averages were summarized in Table 4.1. Adjacently, a scatter plot of the $I(D)/I(G)$ values against the $FWHM(G)$ values is shown in Figure 4.7.

Because the $I(2D)/I(G)$ values of all four types were smaller than one, all resulting graphene materials were of a multi-layer type. In the meantime, by examining the $I(D)/I(G)$ and the $FWHM(G)$ values, it can be deduced that the values were higher for the graphenes deposited with Pt-NPs or Au-NPs than those deposited with Cu-NPs or Fe-NPs, implying a higher density of both defect types. However, this conclusion is not reliable due to the small data set. Correspondingly, their values appeared in the upper right corner in Figure 4.7.

4.1.2 Scanning Electron Microscopy

Introduction to Scanning Electron Microscopy (SEM)

Another way to examine the graphene structure is SEM, a type of electron microscope technology, which uses a beam of focused electrons of relatively low energy as a probe that scans over a surface to create an image. This technology gives information about a surface's topography and composition, based on the electrons'

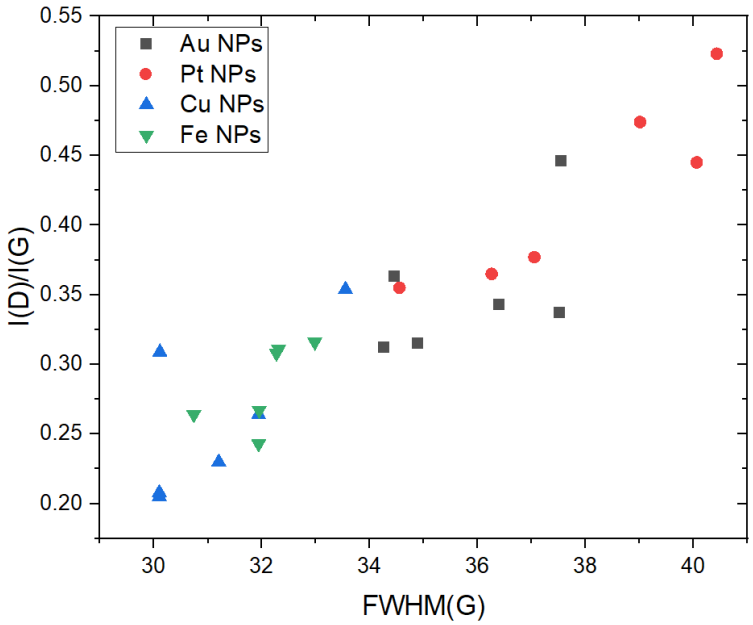

Figure 4.7: $I(D)/I(G)$ against $FWHM(G)$ for the graphene functionalized with different NPs.

reaction toward the surface. In general. when the beam hits the specimen surface, it penetrates the specimen to a few micron depths, depending on the accelerating voltage and the specimen material. Such contacts produce two types of the electrons' behavior: the back-scattered electrons which have relatively high energy, and the secondary electrons with relatively low energy. Together, they are utilized to reconstruct topological images of the specimen surface.

Figure 4.8 illustrates a typical setup of an SEM, which consists of an electron source to generate the electron beam, an anode to accelerate the electrons, a series of lenses to focus the electrons, a set of detectors to collect the emitted signals, and a motorized stage to control the movement of the specimen during a scan. The setup is put inside a vacuum sample chamber to inhibit the evaporation of volatile compounds of the specimen. The collected signals are amplified by an amplifier and then used to generate scanning images[14].

In this study, SEM was performed by a Hitachi Regulus 8230 with a beam acceleration voltage of 3 kV.

SEM after graphene growth on Mo

Figure 4.9 shows an SEM image of the pristine MLG with a magnification of x10000 and x50000, in which the layer structure was to a good extent reassembled. It can be clearly observed that the structure had holes, depicted in black, which corresponds to defects of the graphene. This again proves that the CVD process leads to graphene defects, and is consistent with the results obtained from the Raman Spectroscopy. In the meantime, one can notice the small grains in the image, which identify the MoC layer underneath (Mo is transformed to MoC during growth)[59].

SEM after the Mo etch

The SEM image of the graphene settling on the SiO_2 substrate after the Mo etch is shown in Figure 4.10. The defects density was similar to that in Figure 4.9, which demonstrates that Mo etch step did not introduce more defects. This is another piece of evidence that the transfer-free fabrication method is advantageous.

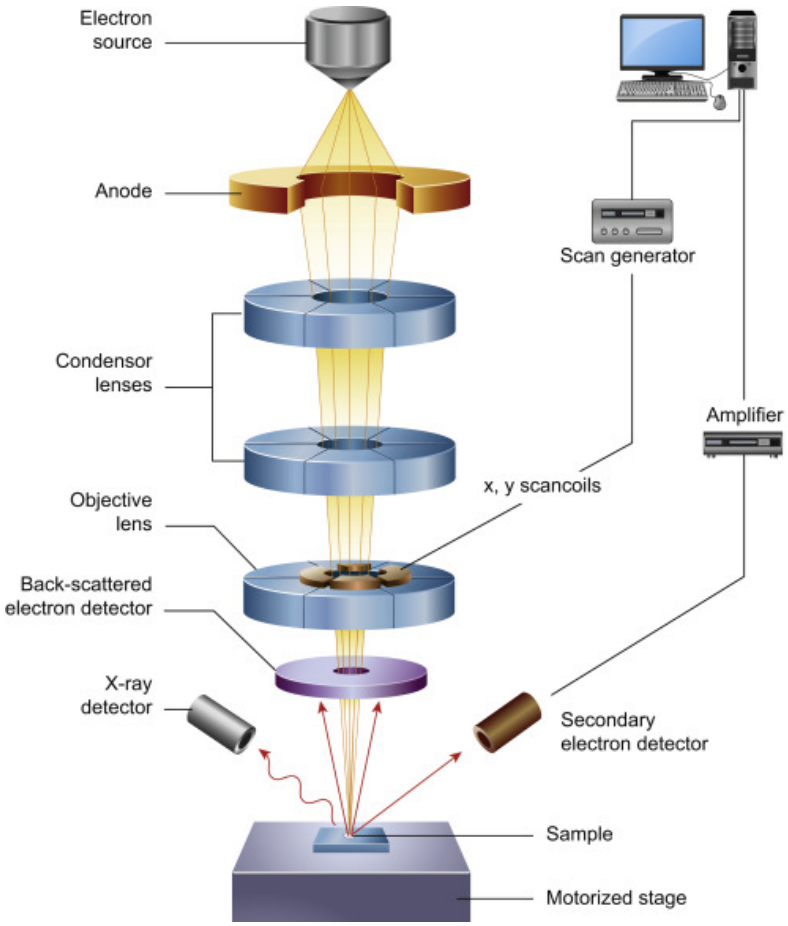

Figure 4.8: The schematic diagram of the core components of an SEM microscope[14].

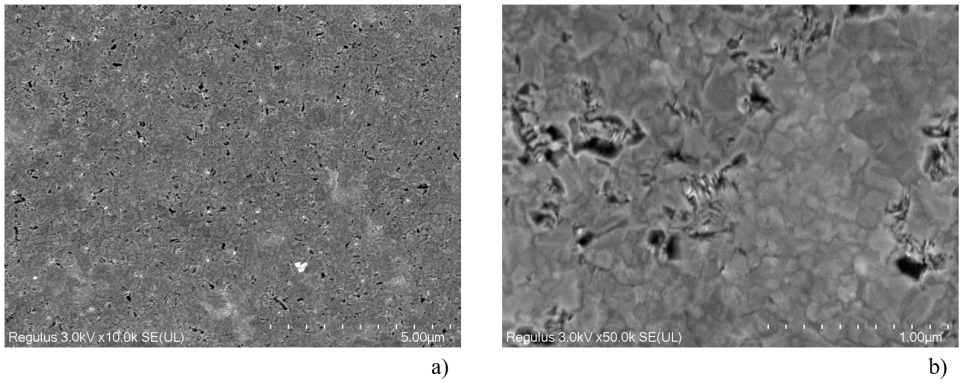

a) b)

Figure 4.9: SEM image of the graphene with Mo underneath with different magnifications: a) with a magnification of 10000x; b) with a magnification of 50000x.

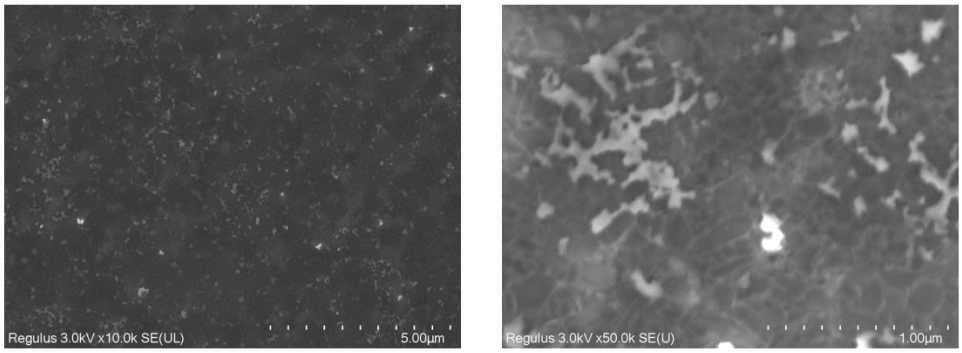

Figure 4.10: SEM image of the graphene after Mo etch with different magnifications: a) with a magnification of 10000x; b) with a magnification of 50000x.

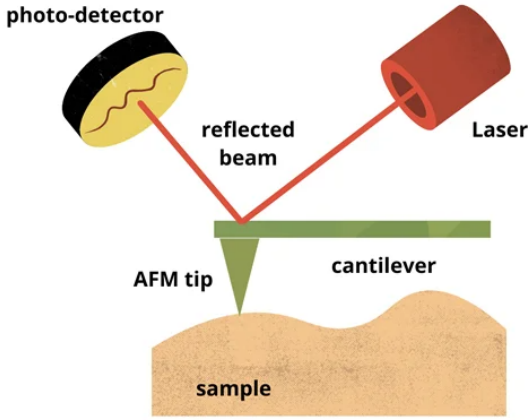

Figure 4.11: Schematic illustrations showing basic principles of AFM. Image Credit: Ilamaran Sivarajah[15].

4.1.3 Atomic Force Microscope

Introduction to Atomic Force Microscope (AFM)

AFM is applicable to almost any type of surface. As the name implies, it relies on the atomic force, which enables it to picture surfaces, including and not limited to polymer, composite, glass, ceramics, nano, and biological materials[15].

Normally, an AFM setup consists of three components as shown in Figure 4.11: a cantilever with a sharp tip, a laser, and a photodetector, normally a position-sensitive photodiode (PSPD). The backside of the cantilever is made of or coated with a reflective material, which reflects the laser light to the photodetector, through which the position information of the laser beam is collected.

Consider the tip approaching a surface, the attractive force first takes place, causing the cantilever to deflect towards the surface. When the tip comes closer to the surface, or even touches it, the repulsive force dominates, causing the cantilever to deflect. The deflection results in a direction change of the reflected beam, and subsequently, a shift in the beam position on the photodetector. By scanning over the surface in a just-mentioned way, an AFM image describing the surface topography can be generated.

In practice, AFM can be performed in three operation modes: the contact mode, the tapping mode, and the non-contact mode. In the contact mode, the tip contacts the surface through an adsorbed fluid layer on it. In the tapping mode, the tip is not in constant contact with the surface, instead, the cantilever oscillates at or

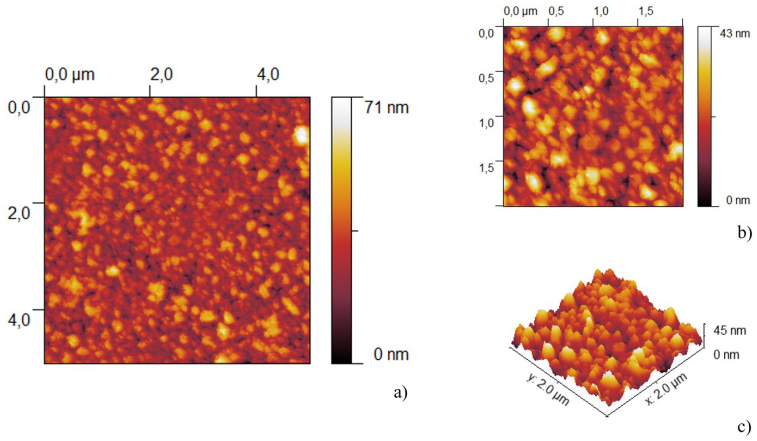

Figure 4.12: AFM acquisition of the graphene with Mo underneath: a) 5nmx5nm MLG sample; b) 2nmx2nm MLG sample; c) 3D view of b).

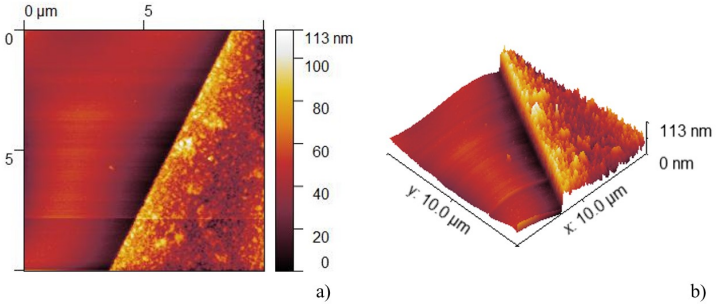

Figure 4.13: AFM acquisition of the graphene strip edge before Mo etch: a) 10nmx10nm MLG sample; b) 3D view of a).

slightly below the resonant frequency, causing the tip to oscillate up and down. In the non-contact mode, the tip oscillates near the sample surface without contacting it.

AFM measurements in this study were carried out in semi-contact mode. The results were processed and analyzed with a data visualization and analysis software, Gwyddion.

AFM after graphene growth on Mo

Figure 4.12 shows 2D and 3D AFM images of the MLG with Mo underneath. The Mo grains can be clearly observed in the figure.

Figure 4.13 shows the surface around the edge of the graphene strip. Especially from the 3D image, one can deduce that the roughness of the SiO_2 substrate and that of the graphene strip were significantly different.

AFM after the Mo etch

The AFM images of the MLG after the Mo etch are in Figure 4.14. Both the graphene structure can be clearly seen. According to the 3D image, the defects were the main contributor to the roughness.

Figure 4.15 shows the AFM images around the edge of the MLG strip on SiO_2 after the Mo etch. Again, the roughness difference between the graphene strip and the SiO_2 substrate remained.

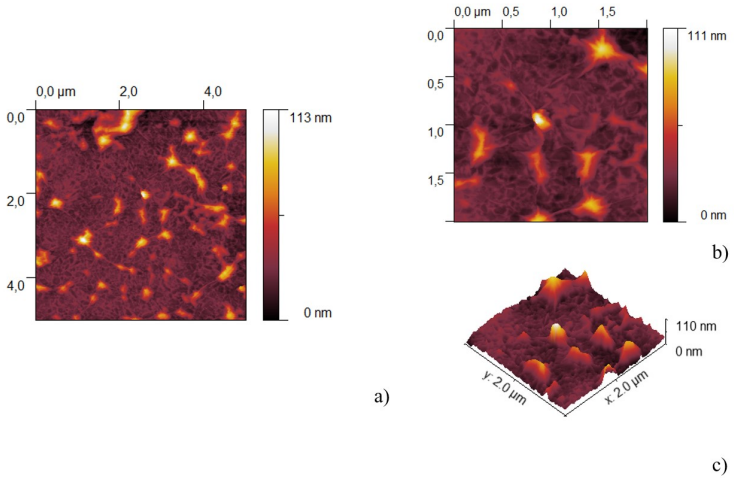

Figure 4.14: AFM acquisition of the graphene after Mo etch: a) 5nmx5nm MLG sample; b) 2nmx2nm MLG sample; c) 3D view of b).

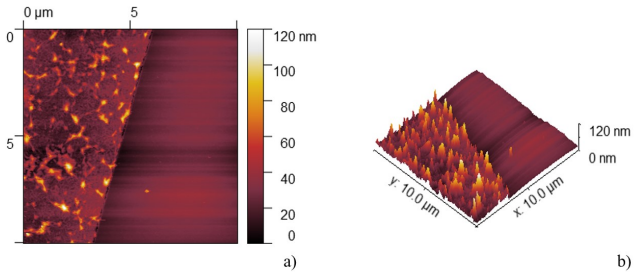

Figure 4.15: AFM acquisition of the graphene strip edge after Mo etch: a) 10nmx10nm MLG sample; b) 3D view of a).

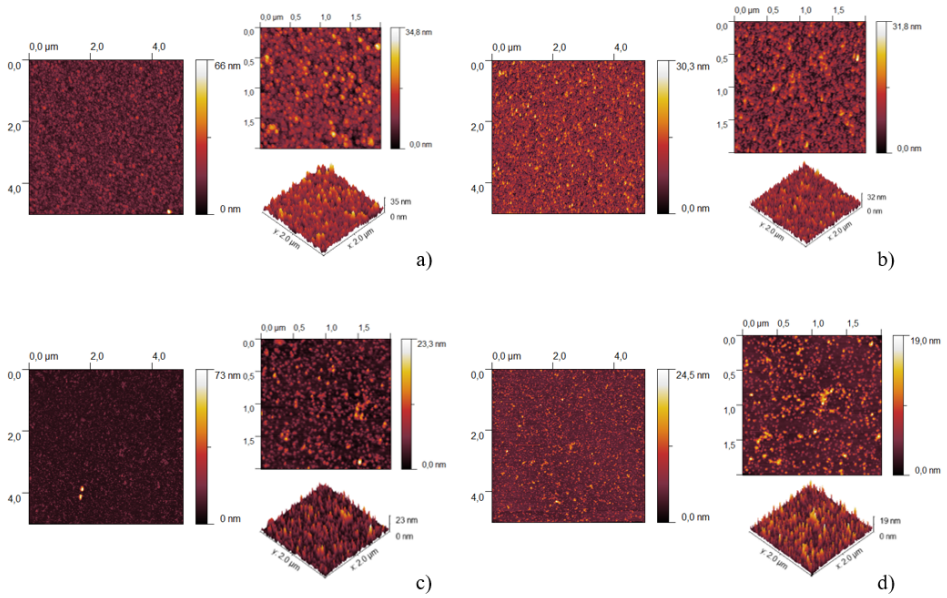

Figure 4.16: AFM acquisition of the graphene strip After Au-NPs deposition with the print speed of: a) 10 mm/min; b) 20 mm/min; c) 75 mm/min; d) 100 mm/min.

AFM after the nanoparticle depositions on SiO_2

Figure 4.16 gives the AFM images of the graphene with Au-NPs printed at different speeds on SiO_2 substrate, with other parameters set constant: a G1 voltage of 1 kV, a current of 3 mA, a nozzle size of 0.08 L/min, a nozzle height of 0.3 mm and a nitrogen flow rate of 1.5 L/min. Four print speeds were tested: 10 mm/min, 20 mm/min, 75 mm/min, and 100 mm/min. Respectively, the roughness of the image of 2 μm x 2 μm was 4.178 nm, 3.570 nm, 2.4 nm, and 2.301 nm, from which a negative correlation between the roughness and the print speed can be deducted. As to be discussed in sTable 4.1.4, the result aligned with the nanoparticle coverage rate derived from the SEM images.

4.1.4 The optimization of the nanoparticle printing

To print nanoparticles with different densities on the graphene instead of forming a layer, the printing parameters need to be optimized. After printing, SEM is used to obtain the density information. The SEM images are taken with a beam acceleration voltage of 3 kV and a magnification of 50000x, and the nanoparticle size distribution is analyzed using the software ImageJ. Also, Matlab can be used to obtain nanoparticle coverage.

For the particle size analysis, choosing an evenly illuminated image is very important. Hence, the first step is to select a part of the image which is evenly illuminated. Then apply a band-pass filter to flatten the image to some extent, and it will reveal the details that you did not notice before. After that, adjust the threshold of the image to make sure all the nanoparticles needed are included in the calculation. The average pixel value of all the nanoparticles is selected as the threshold. At last, the calculation can be accomplished.

There are two possible printing patterns. One is to print dots, and the density can be controlled by adjusting the printing time. The other is to print lines, then the print speed is the determinate factor for the coverage. Due to the mechanical structure of the nozzle of the printer, the minimum printing time is 1 second. If the printer is turned on for less than 1 second, there is the possibility that the nozzle does not have enough time to start working and can not print any nanoparticles.

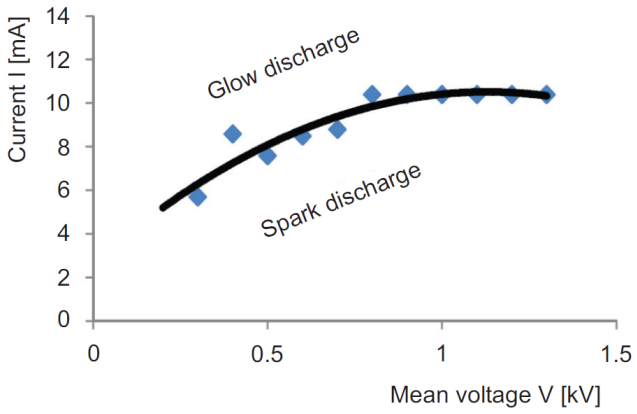

Figure 4.17: Spark discharge limit in nitrogen with VSParticle G1[9].

Metal	Mean voltage(kV)	Current(mA)	Nozzle size(L/min)	Nozzle height(mm)	Flow gas
Au	1	3	0.08	0.3	N_2
Pt	1	3	0.08	0.3	N_2
Cu	1	5	0.08	0.3	N_2
Fe	1	1	0.08	0.3	N_2

Table 4.2: The printing settings for several metals.

When printing dots with a printing time of more than 1 second, the nanoparticles are too dense and form a layer instead of dispersed particles. Hence, in this project, the NPs are printed on the graphene in the form of lines.

Different metals can have different deposition rates. There are many adjustable parameters that can affect the nanoparticle density:

- The mean voltage and current of VSP-G1. Because of the technology of spark ablation used, the mean voltage and the current can have a significant effect on the nanoparticle density. The discharge frequency will increase if the mean voltage and current increase. However, if the frequency goes too high, the spark discharge will become unstable, and it will transfer to a glow discharge mode. In Figure 4.17, the limit where the spark mode transfers to a glow discharge mode is indicated. The higher the mean voltage and current, the higher the discharge frequency, hence the higher the nanoparticle density.
- The nozzle size. There are three different nozzle sizes. In this project, to have the smallest feature, the smallest one is used.
- The nozzle height. The distance between the nozzle and the substrate will also influence the printing results. Generally, the larger the nozzle height, the bigger the printing feature, hence the lower the nanoparticle density.
- The print speed. The higher the print speed, the short the time interval that the nozzle is printing at one location, hence the lower the nanoparticle density.

Towards these different metals, different combinations of the parameters are tested to get the most suitable one for these four metals, which is shown in Table 4.2.

The printing parameter optimization for Au NPs

As listed in Table 4.2, to calculate the nanoparticle coverage using different print speeds, the experiments were done under the condition: the mean voltage is 1 kV, the current is 3 mA, the nozzle size is 0.08 L/min, and the nozzle height is 0.3 mm.

Print speed (mm/min)	10	12	15	16	18	20	30	40	50	75	100
Width (μm)	184	150	152	153	149	143	131	136	131	132	132
Coverage	73%	39%	30%	26%	22%	16%	11%	10%	7%	5%	4%
Roughness (μm)	3.219	2.81	3.63	3.16	2.72	3.422	2.939	3.248	2.146	0.979	1.161

Table 4.3: Details about the Au-NPs printing density

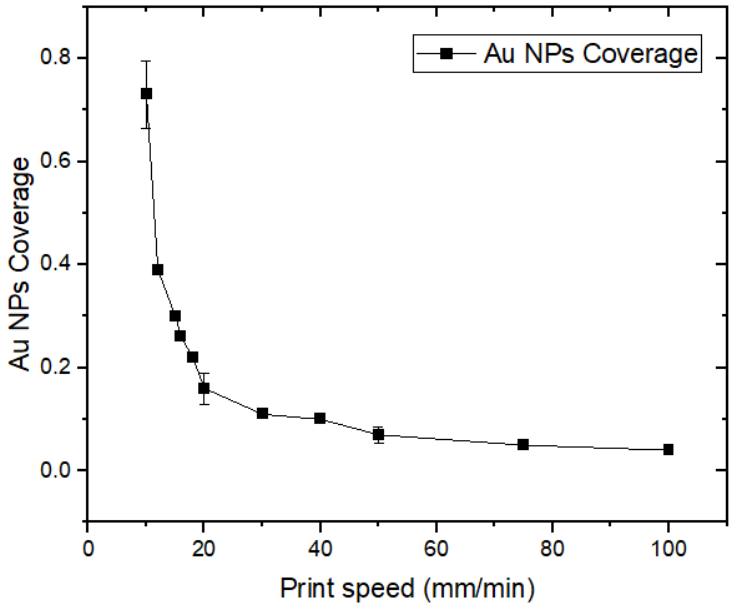

Figure 4.18: The Au-NPs coverage in different print speeds. The coverage values here are the same as shown in the table but in a form of fractions.

The corresponding results are shown in Table 4.3, and Figure 4.18 shows the plot. For each setting, three data points were measured and the error bar was calculated according to this, same as the other metals. The conclusion can be drawn: the higher the print speed, the thinner the printing line width, the lower the nanoparticle coverage, and the smaller roughness.

The printing parameter optimization for Pt NPs

The optimized Pt-NPs printing settings are: the mean voltage is 1 kV, the current is 3 mA, the nozzle size is 0.08 L/min, and the nozzle height is 0.3 mm. The corresponding results are shown in Table 4.4, and Figure 4.19 shows the plot. The results show when the print speed is increased, the printing line width and the nanoparticle coverage are both decreased.

Print speed (mm/min)	10	12	15	20	30	40	50	75	100	150
Width (μm)	274.38	270.05	263.07	248.72	247.6	244.56	237.09	233.23	235.16	240.73
Coverage	67.4%	54.7%	32.3%	26.4%	15%	18.8%	12.6%	8%	5.5%	2.6%

Table 4.4: Details about the Pt-NPs printing density

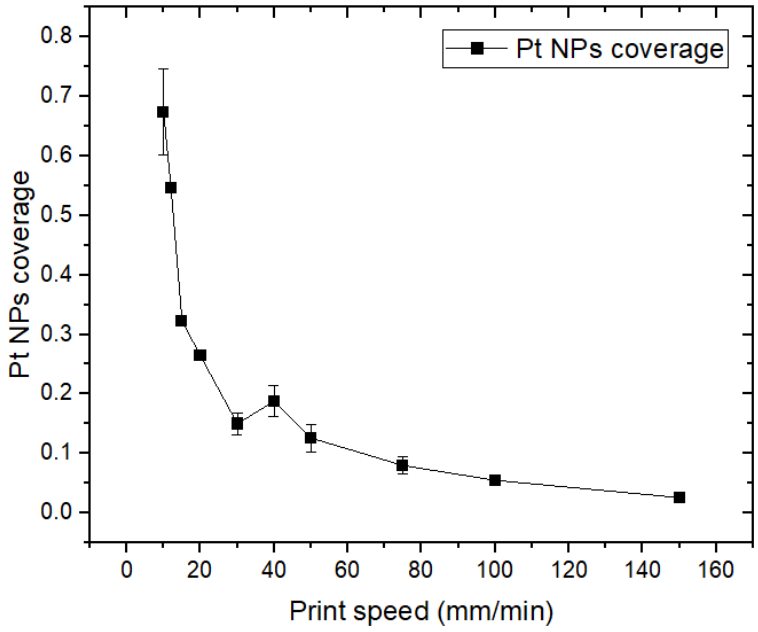

Figure 4.19: The Pt-NPs coverage in different print speeds.

Print speed (mm/min)	1	1.2	1.5	2	3	4	5
Width (m)	346.63	309.17	300.06	303.57	288.95	303.82	198.47
Coverage	70%	48%	35%	27%	20%	14%	9%

Table 4.5: Details about the Cu-NPs printing density

The printing parameter optimization for Cu NPs

Compared to Au and Pt, Cu had a relatively low deposition rate, hence, to have similar densities, the power of G1 needs to be increased. The optimized Cu-NPs printing settings are: the mean voltage is 1 kV, the current is 5 mA, the nozzle size is 0.08 L/min, and the nozzle height is 0.3 mm. The corresponding results are shown in Table 4.5, and Figure 4.20 shows the plot.

The printing parameter optimization for Fe NPs

Compared to Au and Pt, Fe had a relatively high deposition rate, hence, to have similar densities, the power of G1 needs to be decreased. The optimized Fe-NPs printing settings are: the mean voltage is 1 kV, the current is 1 mA, the nozzle size is 0.08 L/min, and the nozzle height is 0.3 mm. The corresponding results are shown in Table 4.6, and Figure 4.21 shows the plot.

Print speed (mm/min)	1	5	10	15	25	50	75
Coverage	100%	52.7%	29.8%	21.3%	16.1%	9.2%	5.6%

Table 4.6: Details about the Fe-NPs printing density

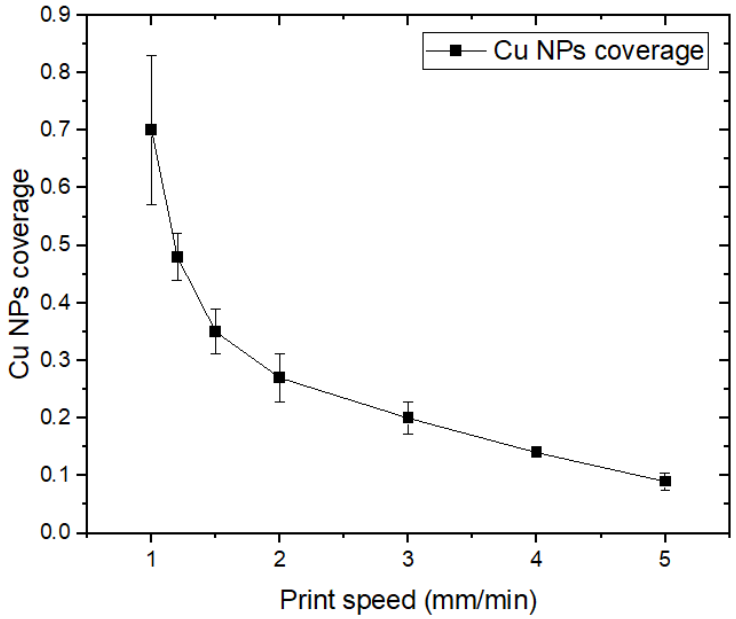

Figure 4.20: The Cu-NPs coverage in different print speed.

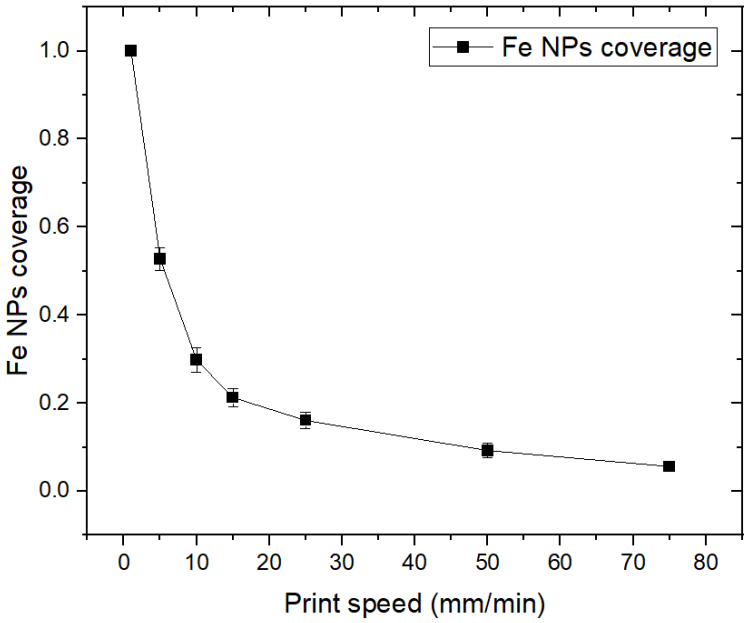

Figure 4.21: The Fe-NPs coverage in different print speed.

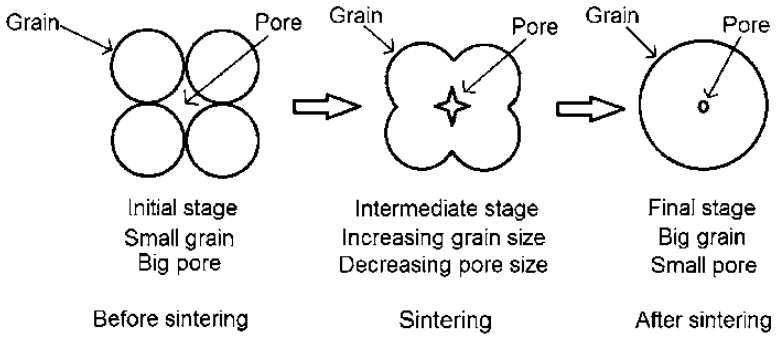

Figure 4.22: The sintering process containing three stages[16]

4.1.5 Nanoparticle annealing on graphene

IV

Heating is a common method to help gas sensor recovery, which can also cause the sintering of nanoparticles. Sintering is a process of converting loose fine particles into a solid coherent mass by heat and/or pressure without fully melting the particles to the point of melting, as shown in Figure 4.22 [60]. For example, the melting point of gold is 1064 °C, while nanoparticle gold can be sintered at a temperature as low as 180 °C, which is much lower than the melting point[61].

As discussed in Chapter 2, normally, the gas sensors need a high temperature or UV illumination to help recover to the initial state. However, the desirable properties of nanostructure may be eliminated during heat treatment. Unlike bulk material, nanostructure material exhibit a high degree of surface curvatures and atomic forces, which makes the sintering of the nanomaterial more complex[62]. Hence, the change of the nanoparticle properties, especially the coverage change after sintering needs further measurements.

Two different experiments are performed in this project related to nanoparticle annealing. One is to determine how the nanoparticle coverages change if they are annealed at different temperatures. The other is to let the nanoparticle undergo annealing multiple times at the same temperature, and observe how the coverage changes.

Experiment 1: annealing at different temperature

Figure 4.23 shows the coverage change of Au-NPs before and after annealing at different temperatures for 5 minutes. The Au-NPs are printed under the condition of: the generator voltage of 1kV, the generator current of 3mA, the nozzle size of 0.08L/min, and the print speed of 10 mm/min, the printing height of 0.3 mm. It is obvious that the shape of the nanoparticles becomes smoothed and condensed when the annealing temperature increases, which gives decreased coverage.

The same experiments are also executed with different print speeds: 15 mm/min, 20 mm/min, 40 mm/min, and 75 mm/min. It turns out that the same phenomenon occurs even though the nanoparticles are printed at different speeds. The black curve in Figure 4.24 shows the nanoparticle coverage before annealing, while the red and blue curves show the coverages after annealing at $100C$ and $200C$ respectively. Obviously, the nanoparticle coverage decreases after annealing, and it drops more at a higher temperature.

Figure 4.25 shows the Pt-NPs coverage change after annealing at different temperatures, and it exhibits the same conclusion as the Au-NPs.

Unlike the Au-NPs and Pt-NPs, the coverage of Cu-NPs hardly changed after the annealing, as shown in Figure 4.26.

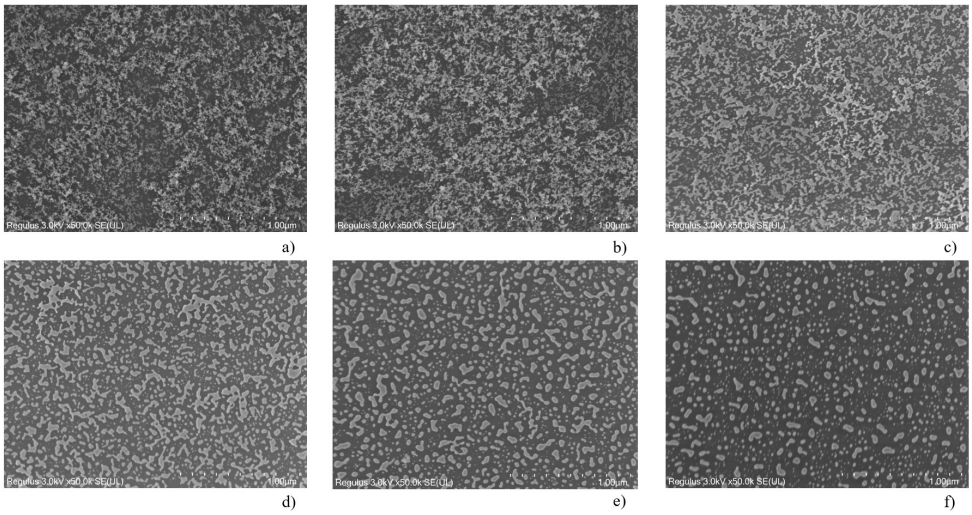

Figure 4.23: The SEM images of Au-NPs morphology change after annealing at different temperatures for 5 minutes: a) before annealing; b) annealing at 100 °C; c) annealing at 150 °C; d) annealing at 200 °C; e) annealing at 250 °C; f) annealing at 350 °C.

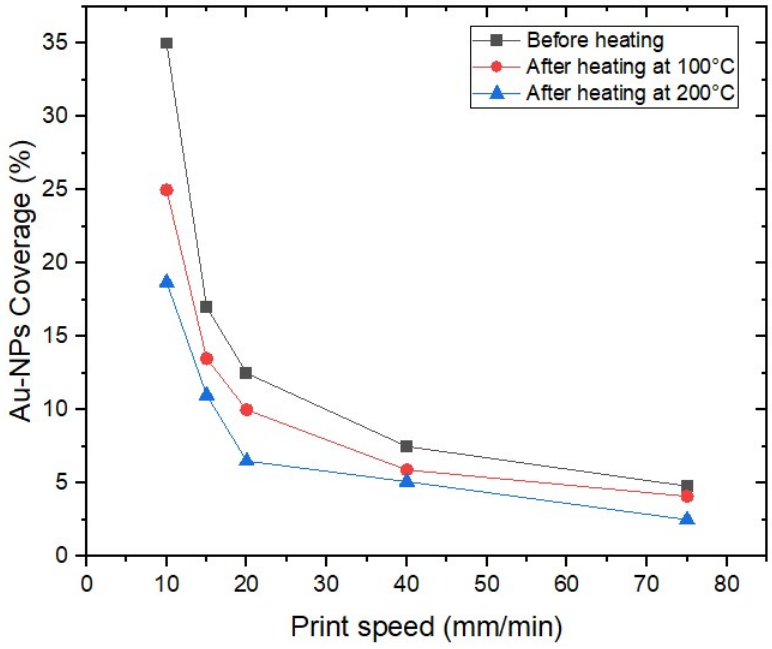

Figure 4.24: The plot of Au-NPs coverage with different print speeds before and after annealing at different temperatures.

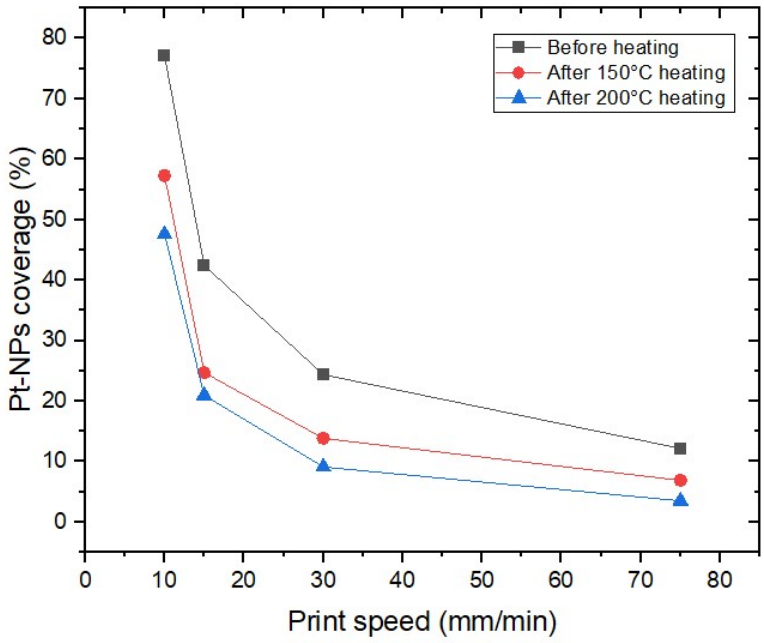

Figure 4.25: The plot of Pt-NPs coverage with different print speeds before and after annealing at different temperatures.

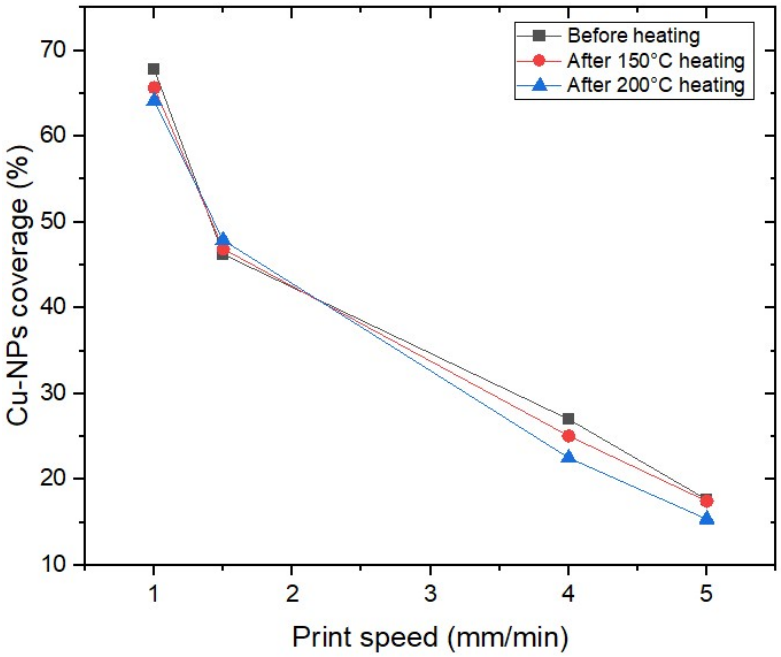

Figure 4.26: The plot of Cu-NPs coverage with different print speeds before and after annealing at different temperatures.

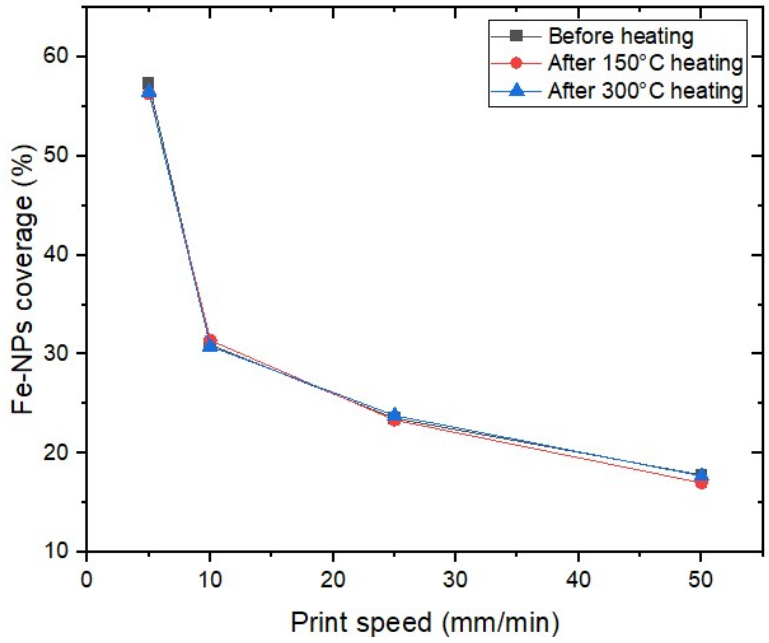

Figure 4.27: The plot of Fe-NPs coverage with different print speeds before and after annealing at different temperatures.

Figure 4.27 shows the Fe-NPs coverage change after annealing at different temperatures, and there is no significant change.

This can be explained by the oxidation of the Cu-NPs and Fe-NPs once they have contact with air. Conversely, Au and Pt are more stable than them. X-ray diffraction can be performed to explore the reason further. Another possible explanation is the difference of dewetting of the different metals. The noble metals can have less adhesion to the surface than other metals.

Experiment 2: annealing multiple times at same temperature

Figure 4.28 shows the nanoparticle coverage change of the four kinds of metals after annealing for multiple times at the same temperature. There is no obvious change among all the four kinds of nanoparticles. This is a good thing for the project, which means the sensor recovery through heating will not change the morphology of the nanoparticles after the first annealing step. The response of the sensor can then be considered stable.

4.2 DEVICE CHARACTERIZATION

In this project, four-wire measurements are performed to measure the resistance of the device. Because the size of the graphene strips is 200 x 20 μm, the sheet resistance can be calculated by

$$R_{\square} = R * W/L \tag{4.1}$$

where $R_{\square}$ is the sheet resistance, R is the measured resistance, W is the width of the graphene strip, and L is the length of the graphene strip.

In this project, a Cascade probe station equipped with an HP 4156C parameter analyzer is used to execute the 4-wire measurement. Besides, a heater is integrated inside the probe station, which can be used to measure the temperature coefficient of resistance (TCR).

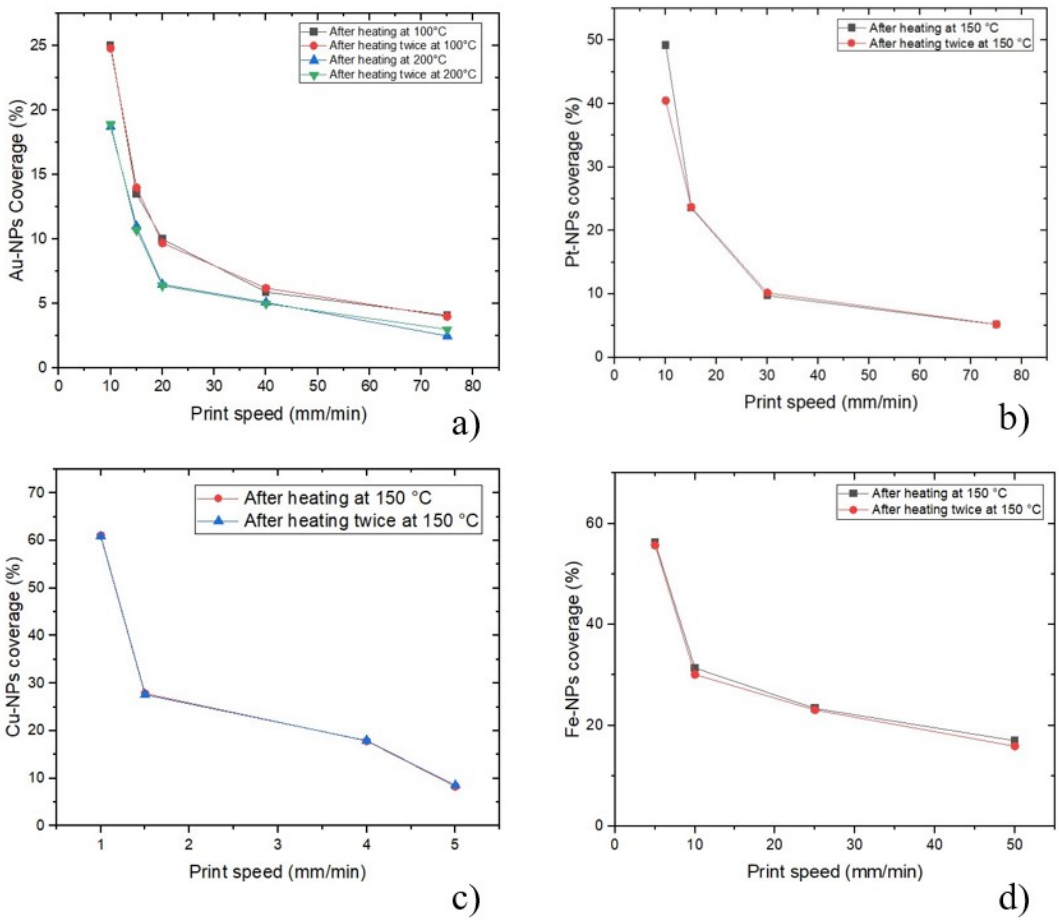

Figure 4.28: The nanoparticle coverage with different print speeds after annealing multiple times at the same temperature: a) Au-NPs; b) Pt-NPs; c) Cu-NPs; d) Fe-NPs.

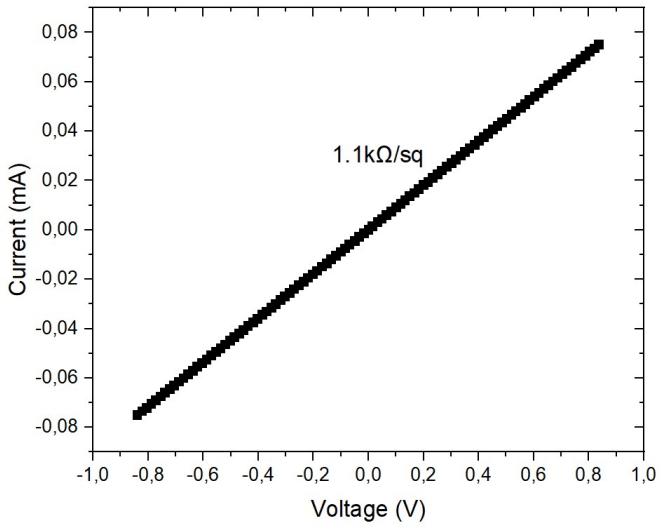

Figure 4.29: I-V characteristics of the graphene strip before functionalization.

Print speed (mm/min)	10	15	20	40	75
Resistance before NPs deposition (Ω)	1032.5	933.1	939.9	963.1	942.5
Resistance after NPs deposition (Ω)	1076	984.7	1002.8	1033.4	1016.9
Resistance change (Ω)	+43.5	+51.6	+62.9	+70.3	+74.4

Table 4.7: The change of the sheet resistance before and after Au-NPs deposition

4.2.1 I-V characteristic

Figure 4.29 shows the I-V characteristic of one of the graphene strips, and the sheet resistance of which is 938 Ω.

4.2.2 Wafer map

The wafer-scale sheet resistance measurement results are listed in Figure 4.30.

Because the process variation between wafers exists, the sheet resistance shown in a later chapter can be bigger or smaller than this value. The largest variation between devices in this study can be 90%.

4.2.3 Sheet resistance change after functionalization

Table 4.7, Table 4.8, Table 4.9, and Table 4.10 show how the sheet resistance of the graphene strips change after the nanoparticle deposition respectively. The results exhibit a resistance increase after the functionalization. This is another piece of evidence that shows the deposition of nanoparticles changes the property of the pristine graphene.

Print speed (mm/min)	10	15	30	75
Resistance before NPs deposition (Ω)	1328.2	1288.3	1257.6	1368
Resistance after NPs deposition (Ω)	1386.4	1381.7	1379.6	1462.3
Resistance change (Ω)	+58.2	+93.4	+122	+94.3

Table 4.8: The change of the sheet resistance before and after Pt-NPs depostion

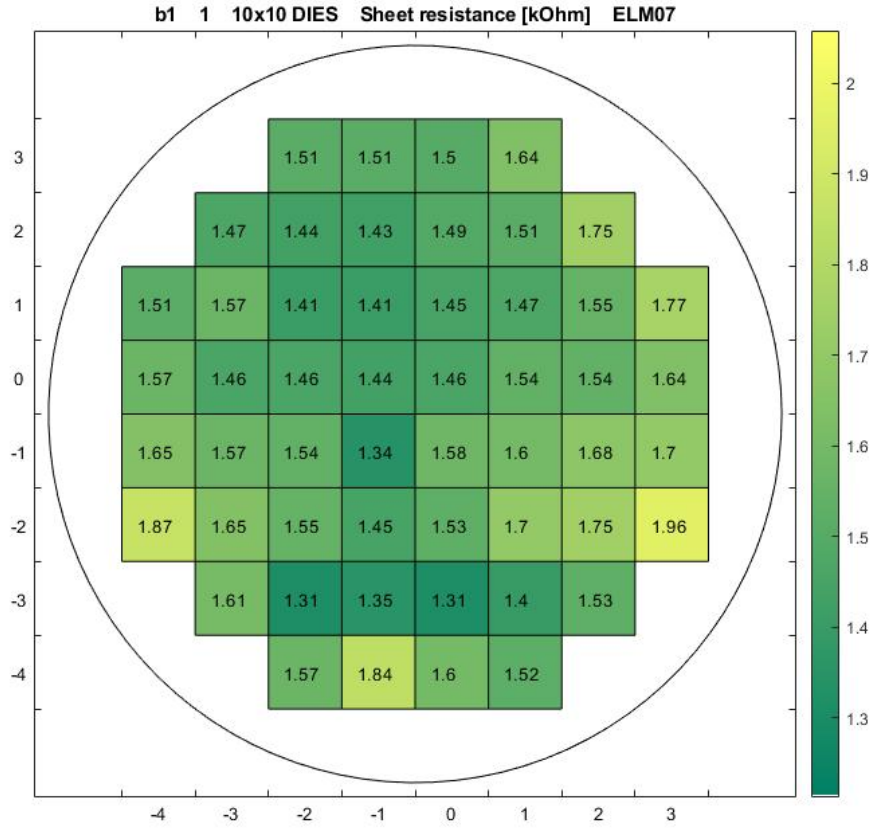

Figure 4.30: The wafer map depicting the average sheet resistance of the 52 dies on a whole wafer.

Print speed (mm/min)	1	1.5	4	5
Resistance before NPs deposition (Ω)	1005.7	1001.7	1081.8	1064.6
Resistance after NPs deposition (Ω)	1097.1	1088.4	1131.5	1123.9
Resistance change (Ω)	+91.4	+86.7	+49.7	+59.3

Table 4.9: The change of the sheet resistance before and after Cu-NPs depostion

Print speed (mm/min)	5	10	25	50
Resistance before NPs deposition (Ω)	978.3	982.6	979.1	968.7
Resistance after NPs deposition (Ω)	1030.9	1033.6	1036.1	1030.9
Resistance change (Ω)	+52.6	+51	+57	+62.2

Table 4.10: The change of the sheet resistance before and after Fe-NPs depostion

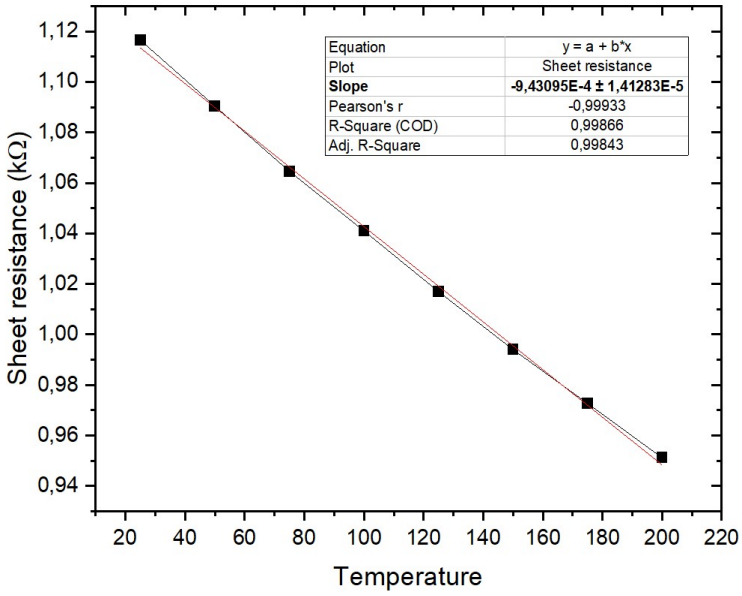

Figure 4.31: Sheet resistance measurement results of graphene strips at different chuck temperatures. The figure includes the linear fits.

4.2.4 Thermal coefficient of resistance

In Figure 4.31, the sheet resistances of the graphene strip at different chuck temperatures are depicted. The figure shows the average value of five strips among five different dies. It exhibits a constant negative TCR value over the temperature range ($25 \sim 200°C$), which is $(-9.43 \pm 0.14) * 10^{-4} K^{-1}$, which matches values reported in [63].

4.3 DISCUSSION

In this chapter, the properties of pristine graphene, NPs, and MLG strips were shown to investigate the physical and electrical properties of the devices.

For graphene and NPs, Raman spectroscopy was first performed. It was found that there was more noise before etching Mo. This is because the signal from graphene can be suppressed when it is on Mo, while the signal on SiO_2 becomes much larger[64]. Moreover, the spectra of graphene have higher $I(D)/I(G)$ values (or lower $FWHM(G)$ values) after the Mo etching step than before the Mo etching. This may be related to the unbound C bond caused by the detachment of Mo atoms from the MoC catalyst during graphene growth.

The spectrum of the graphene after the NPs deposition shows little difference compared to the graphene without deposition. As shown in Figure 4.7, Au-Nps and Pt-NPs functionalized graphene showed higher $I(D)/I(G)$ values and $FWHM(G)$ values. In principle, this is related to the more defects inside the Au-Nps and Pt-NPs functionalized graphene. However, due to the small data sets, such a conclusion is not reliable.

SEM and AFM were also performed to examine the material structure. Both of them showed clear graphene structure and NPs after functionalization.

According to the SEM inspection result, the NP coverage can be deduced. This is done using a software imageJ with a threshold of the average pixels of all the NPs. To find out the optimal NP printing parameters for gas sensing, different combinations of the print settings are examined. And for all types of NPs, the lower the generator voltage and current, the higher the print speed, then the lower

the coverage. For each type of NPs, several printing settings are chosen to get different NPs coverages in Section 4.1.4.

An annealing experiment was also performed to study the change in coverage of NPs on the graphene surface after the purge step with the heater. For Au-Nps and Pt-NPs, the coverage values decreased when the annealing temperature increased. This is due to dewetting, a phenomenon in which a thin liquid film on a substrate cracks, leading to the formation of droplets. However, when the annealing temperature was increased, the coverage values of Cu-NPs and Fe-NPs did not change significantly. This can be explained by the oxidation of Cu-NPs and Fe-NPs, which makes them even more stable. Moreover, it was found that after the first annealing, all kinds of NPs became stable and did not change even after repeated annealing at the same temperature.

The I-V characteristics of MLG strips showed the resistance property, and the wafer map of sheet resistance is shown in Figure 4.30. The stability of the resistance in the middle of the wafer is due to the higher temperature in the center area of the heater in the Blackmagic, which is a device for growing graphene.

After NP deposition, the resistances of all four device types increased. This may be related to the fact that the gas flow damaged the graphene during printing. Further investigation needs to be done in this regard.

Finally, the MLG strips showed a negative TCR, which was $(-9.43 \pm 0.14) * 10^{-4} K^{-1}$. The value is in agreement with those reported in the literature[63].

5 GAS SENSOR TEST

This chapter presents and discusses the experimental results of the gas sensor test. The first section discusses the response of the devices to the humidity, and the next section discusses the response to nitrogen dioxide (NO_2). In each section, different kinds of devices will be introduced and compared, which include pristine devices, and functionalized devices with different nanoparticles. Before each device was measured, it was heated for 20 minutes to remove adsorbed gas.

The device response displayed in the later section was calculated by

$$R[\%] = 100\% * (R_{Gas} - R_{N_2})/R_{N_2} \tag{5.1}$$

where R_{Gas} and R_{N_2} are sheet resistance measured during the exposure to measured gas during a gas test step and during the N_2 exposure, respectively. The resistance measured during the N_2 exposure acts as a reference here. The MLG devices were biased with 1 V.

5.1 GAS SENSOR TESTS TOWARDS HUMIDITY

The gas sensor shows different responses to different gases depending on the electronic properties of the gases. As discussed in Chapter 2, H_2O acts as an electron acceptor, which can increase the conductivity and decrease the resistance of p-type graphene. Next to it, the different interaction modes between the water electrostatic dipole moment and the defects in the graphene may also cause the sensitivity of the resistance change[65]. The absorption of the water molecule at the grain boundary can lead to an increase in resistivity because of the electronic property of the water molecule and the p-type conductivity of the graphene. Conversely, the adsorption at the edge defects in MLG can lead to a decrease of the resistivity due to the formation of the conductive chains with ionic conductivity[66].

In this study, two kinds of gas sensing devices being tested: the pristine MLG devices without any nanoparticles, and the functionalized MLG devices with Au-NPs.

5.1.1 The pristine MLG devices

The MLG strips were exposed to different humidity levels between 10% and 84%. The humidity increases as a step function, and at each humidity level, 10 minutes is allowed to let the device respond.

As observed in Figure 5.1, when the humidity level is low, the resistivity shows little change. Only when the humidity value increased to a value higher than 80%, the resistivity of several strips started to decrease, while there are still three of them remaining unchanged. When the humidity level went back to a very low level, two of the strips which had a large decrease at high humidity levels increased a bit. The other three strips had no significant changes.

The normalized response of the pristine MLG devices is depicted in Figure 5.2. With the humidity level lower than 60%, the response was nearly zero. When the humidity exceeded 60%, generally, the strips have a negative response.

Because the resistivity of three MLG strips hardly responds to the humidity, even with a very high level, it is hard to say the pristine MLG devices are sensitive

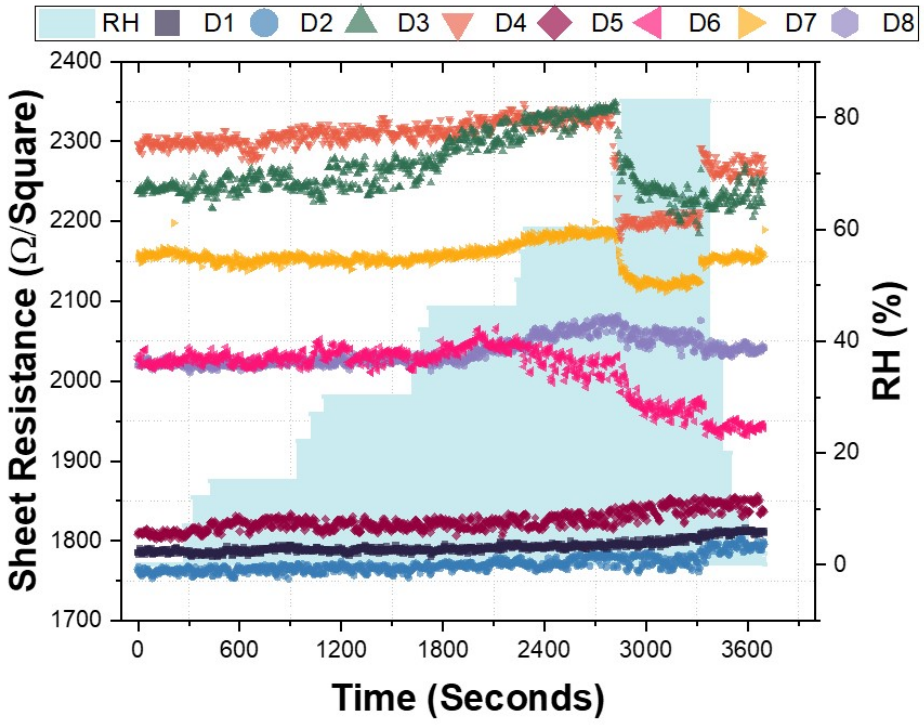

Figure 5.1: MLG sheet resistances (lift y-axis) of eight MLG strips in a pristine device at different humidity steps (right y-axis). The right MLG strips are indicated by D1 to D8.

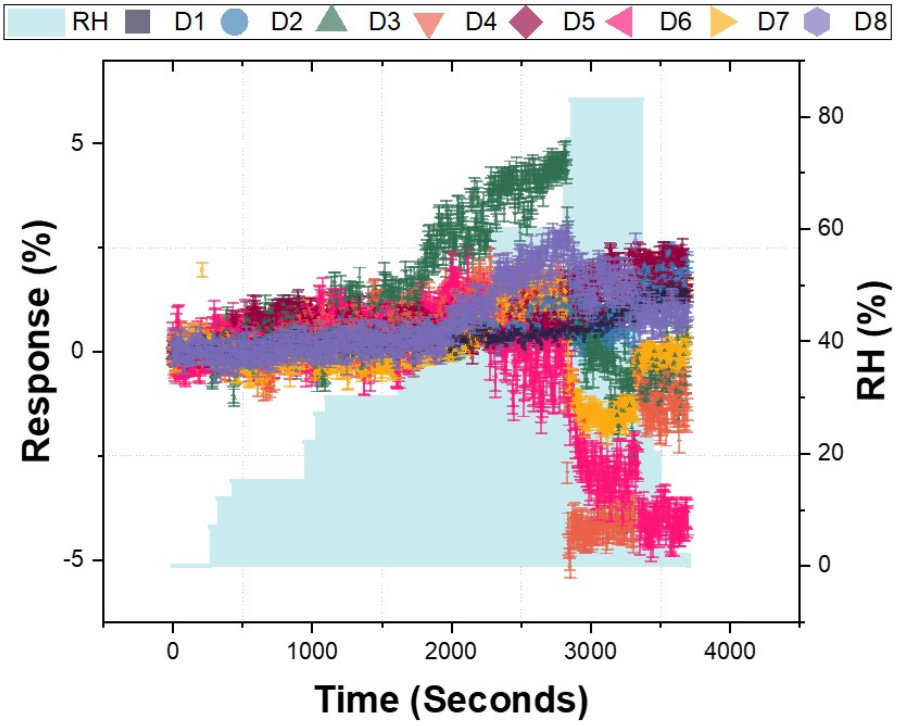

Figure 5.2: The responses (lift y-axis) of eight MLG strips in a pristine device at different humidity steps (right y-axis). The right MLG strips are indicated by D1 to D8.

to the humidity. The result is inconsistent with Smith's study, which introduced a humidity sensor based on CVD-grown single-layer graphene placed on s SiO_2 layer of a Si wafer. This device exhibited excellent sensing performance towards the humidity sensing: a large response and a fast response and recovery time[65]. However, this is consistent with Filibert's results, which shows along the range 30% - 70% of RH, the current variation is as low as 0.005%/%RH[67].

This inconsistency may be caused by the different graphene structures and potential process variation. In Smith's study, the graphene is single-layer, while in this study, the graphene is multi-layer. Next to it, the graphene in this study is fabricated using the transfer-free method, which can also change the property of the graphene.

As for the big resistivity decrease, when the humidity level increases , the intercalated water molecules can form a layer, which can also affect the conductivity[68].

5.1.2 The functionalized devices with Au-NPs deposition

The functionalized MLG strips were exposed to different humidity levels between 10% and 84%. The humidity increases as a step function, and at each humidity level, 10 minutes is needed to let the device respond.

The device tested in this section consists of 6 MLG strips, which are deposited by the Au-NPs with different coverage: 75%, 30%, 15%, 10%, 5%, and 0%. These different coverages are obtained by varying the print speed, as discussed in Section 4.1.4. The purpose of testing different coverage is to select the most suitable coverage with the best response.

The sheet resistance changes of the device introduced before at different humidity levels are depicted in Figure 5.3. When the humidity level is smaller than 60%, all the strips showed a low response. When the humidity level increased to 85%, the strips with the coverage of 75%, 2%, and the pristine graphene have an increased sheet resistance, while the others have little change.

Figure 5.4 shows the normalized response. Unlike the pristine devices, the devices with Au-NPs deposited to have a positive response to the humidity level exceeding 60%.

There is no evidence that can illustrate the response is related to the nanoparticle coverage in this device. The variation between strips may contribute to the response difference. Nevertheless, compared to the response of pristine device in Figure 5.2, the nanoparticle functionalization does change the response direction. The pristine MLG strips have a negative response when the humidity steps enter a relatively high level, while the functionalized MLG strips have a positive response.

5.2 GAS SENSOR TESTS TOWARDS NITROGEN DIOXIDE (NO_2)

As a p-type material, the adsorption of oxygen molecules results in the formation of a hole accumulation layer on the surface of the graphene. Thus nitrogen dioxide (NO_2), which is an oxidizing gas, therefore should increase the conductivity of the graphene.

In this section, the pristine devices, and the functionalized devices were tested towards the exposure of NO_2.

5.2.1 The pristine MLG devices

The first test is to put the devices under the exposure of 1 ppm of NO_2 for 17 minutes, and then heat the device to accelerate the recovery. The heating is done

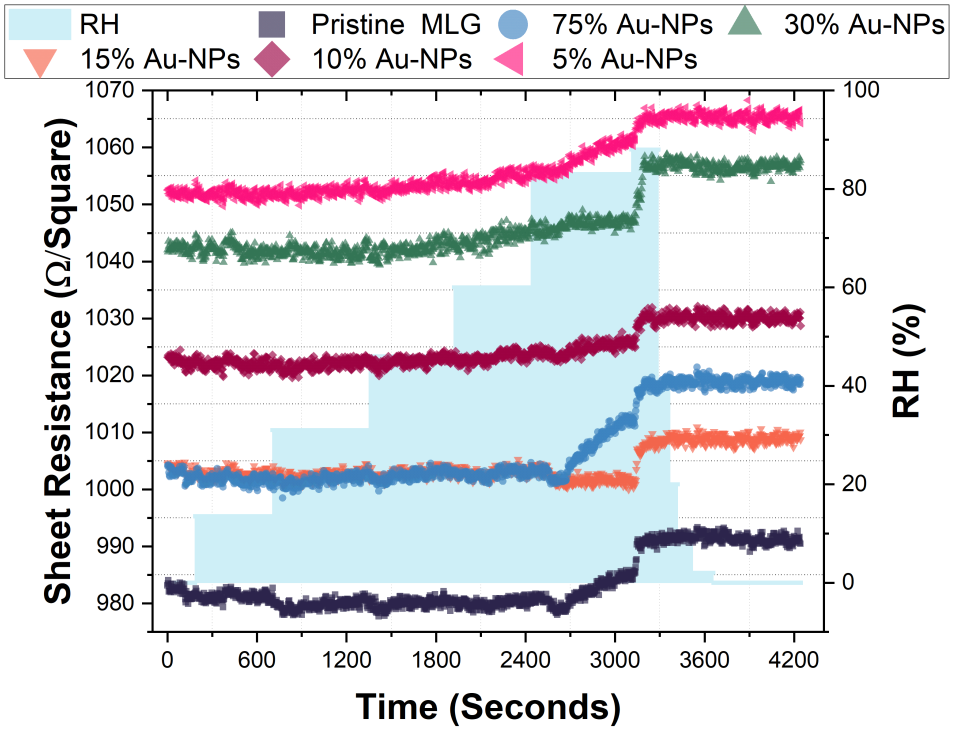

Figure 5.3: MLG sheet resistances (lift y-axis) of the devices with Au-NPs deposited in different coverage at different humidity steps (right y-axis). The nanoparticle coverage varies from 5% to 75%.

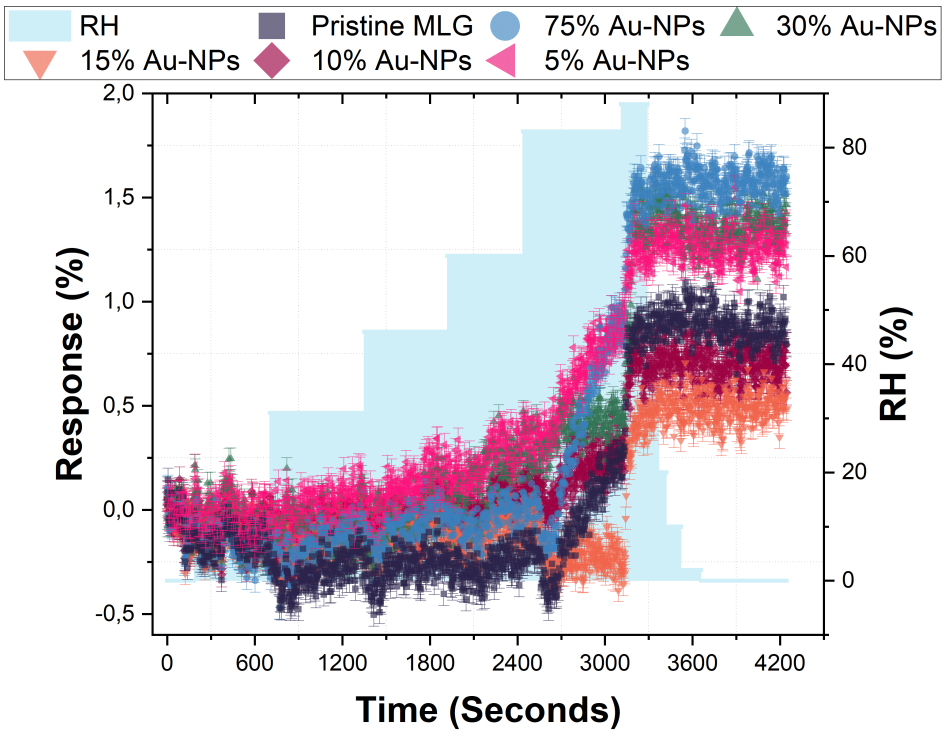

Figure 5.4: The response (lift y-axis) of the devices with Au-NPs deposited in different coverage at different humidity steps (right y-axis). The nanoparticle coverage varies from 5% to 75%.

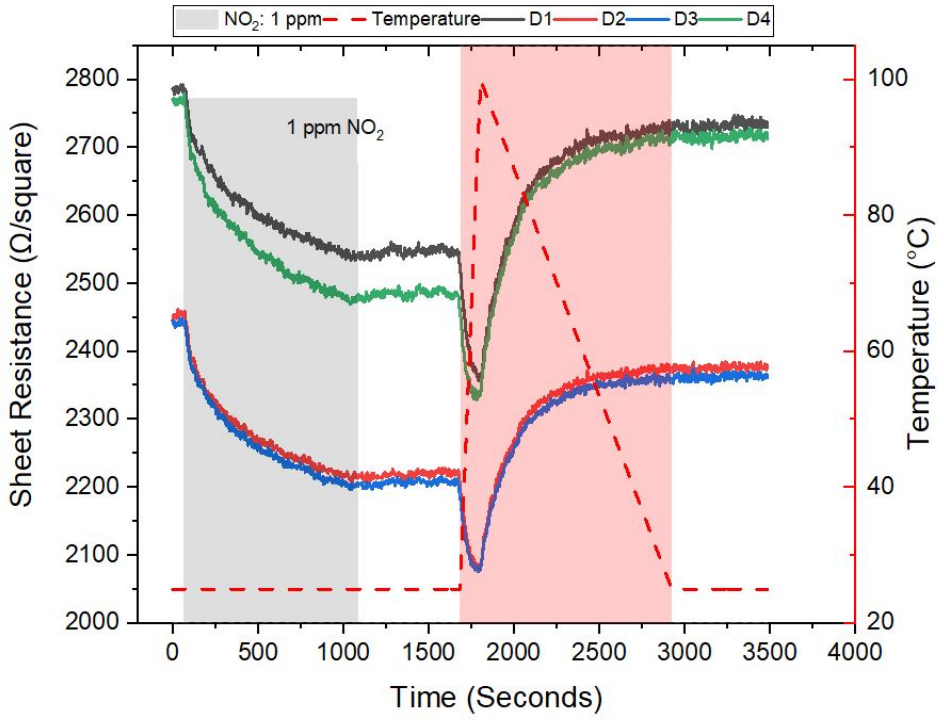

Figure 5.5: The response of pristine devices with baseline in dry N_2, followed by 10 minutes of exposure to NO_2 with a concentration of 1 ppm. A heater is added to help the recovery.

by a ceramic heater underneath the device inside the chamber. Because this heater is not a micro hotplate that can reach the desired temperature and go back to room temperature immediately, it takes time to heat up the heater and let it cool down. During the cooling period, the temperature is still high, thus once the heater reaches the setting value, it will be turned off to avoid the recovery time being too long. All the strips inside a device are measured simultaneously using the automatic measurement setup as discussed in Section 3.2.2.

Figure 5.5 shows the sheet resistance change to the exposure of NO_2 with the concentration of 1 ppm. The pink area shown in Figure 5.5 is the period that the temperature is higher than room temperature, while the red dash line is the real temperature of the heater.

When the MLG strips are exposed to the NO_2 with the concentration of 1ppm, the sheet resistance decreased, which is consistent with the conjecture at the beginning of this section. After the exposure period, the sheet resistance did not increase to the original value, which means there are few gas molecules desorbed from the MLG strips. Then when the temperature increased, the sheet resistance even decreased while the temperature started to increase, which is due to the negative thermal coefficient of resistance. Finally, the sheet resistance increased back to the approximate initial value.

Figure 5.6 shows the sheet resistance change to the different NO_2 concentration levels. The concentration level increased from 250 ppb to 5 ppm, and then it decreased back to 250 ppb. There are five levels in both the concentration increasing regime and the decreasing regime, which are 250 ppb, 500 ppb, 1 ppm, 3 ppm, and 5 ppm. After each exposure to NO_2, the heater will be powered on to help with the NO_2 desorption from the surface of the MLG. Once the heater temperature reached 100 $\circ C$, the heater is turned off and waited for it to cool down to room temperature, which will take approximately 15 minutes.

It can be clearly observed that the resistance decreases more when the NO_2 concentration is at a high level. However, 15 minutes is not enough for the MLG strips

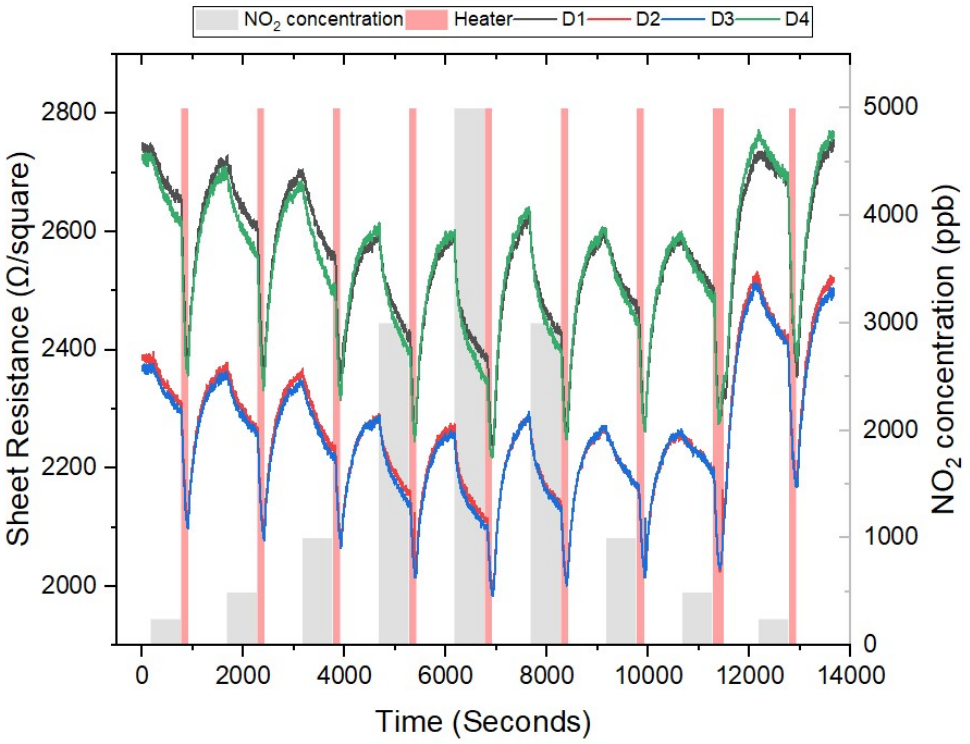

Figure 5.6: MLG sheet resistances (lift y-axis) of four devices at different NO_2 concentration steps (right y-axis).

to recover to the initial state. The sheet resistance increase at the next to the last NO_2 exposure is because of the longer heating time compared to the before steps.

Figure 5.7 shows the response as a function of NO_2 concentration levels. The response is calculated by doing an average of the sheet resistance value during the first and the last minute of exposure of the gas steps, and the results show the average values of the four devices.

As shown in Figure 5.7, as the NO_2 concentration increases, the devices had bigger responses. However, the response shows non-linear relation, unlike the humidity test. This can e attributed to the partial recovery at higher NO_2 levels.

5.2.2 The functionalized devices with Au-NPs deposition

The devices tested in this section are deposited with different Au-NPs coverages: 75%, 30%, 15%, 10%, and 5%, which are controlled by adjusting the print speed.

Figure 5.8 shows the sheet resistance change of the MLG strips with different Au-NPs coverages to the exposure of NO_2 with a concentration of 1 ppm. The pink area is the period that the temperature is higher than room temperature, while the red dash line is the real temperature of the heater.

When the heater was turned on and started to heat up the device, the resistance decreased, which is consistent with the results of the pristine devices because of the negative TCR. After the recovery period, the devices can go back to the initial values.

Figure 5.9 shows the response of MLG strips with different coverages towards the NO_2 with a concentration of 1 ppm. The responses were calculated by doing an average of the sheet resistance value during the first and last minute of exposure of the NO_2 steps.

As can be observed from Figure 5.9, when the coverage increased from 0 to 5%, the response also increased. But it started to decrease when the coverage increased more to 15% and increased again when the coverage reached 75%. However, the

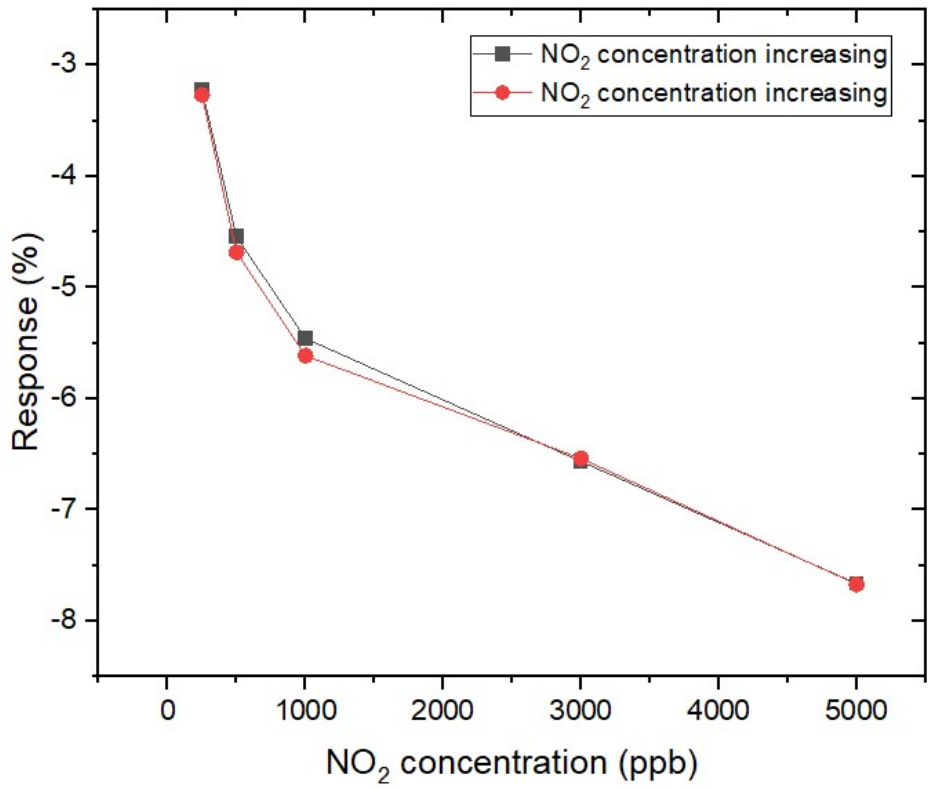

Figure 5.7: Response as a function of NO_2 concentration level, where the response was calculated through the increasing and decreasing of the NO_2 steps during the first and last minute of NO_2 exposure.

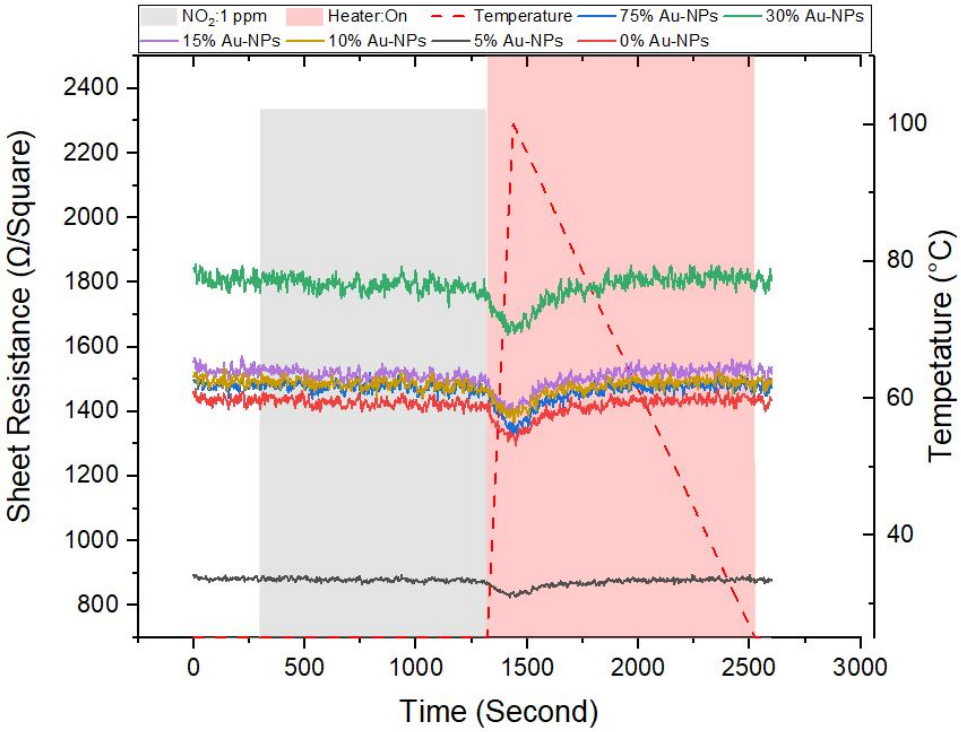

Figure 5.8: The response of device deposited by Au-NPs with baseline in dry N_2, followed by 10 minutes of exposure to NO_2 with a concentration of 1 ppm. A heater is added to help the recovery. The pink area is the period that the temperature is higher than room temperature, while the red dash line is the real temperature of the heater.

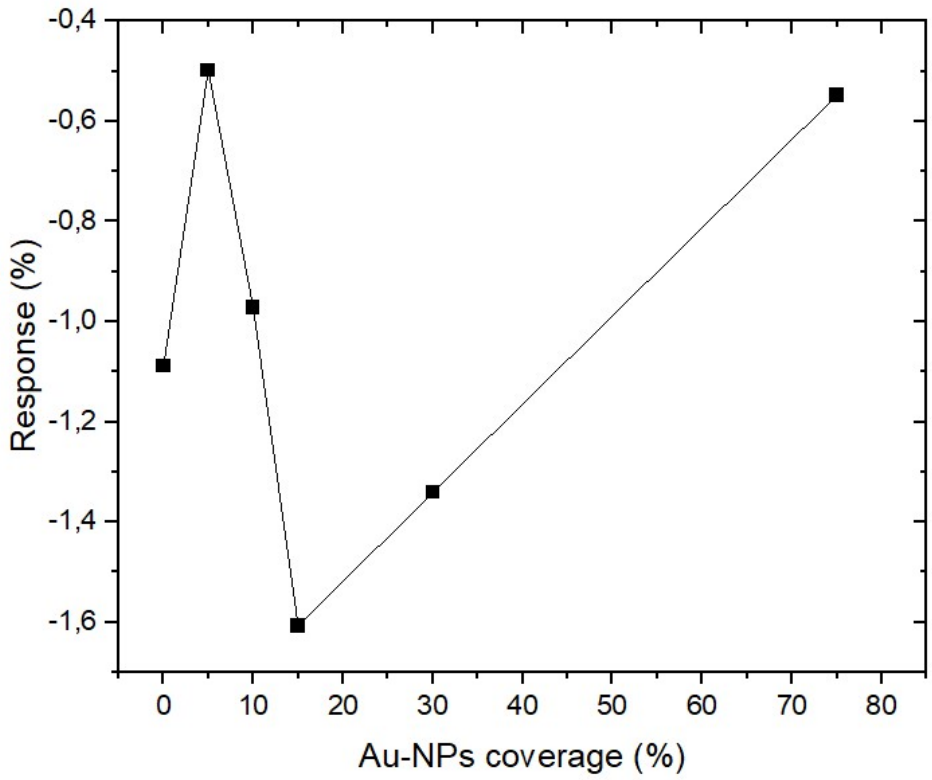

Figure 5.9: The response to 1 ppm of NO_2 as a function of different Au-NPs coverage. The responses were calculated by doing an average of the sheet resistance value during the first and last minute of exposure of the NO_2 steps.

response values of all these coverages are relatively small, thus it is hard to draw the conclusion that the response is related to Au-NPs coverage.

Figure 5.10 shows the sheet resistance change to the different NO_2 concentration levels, which are 250 ppb, 500 ppb, 1 ppm, 3 ppm, and 5ppm. After each exposure period, the heater is used to help the recovery. Figure 5.11 shows the response towards different NO_2 concentration levels.

When the NO_2 concentration level is high, the sheet resistance has a clear decrease. However, the difference between the devices with different nanoparticle coverages is unclear, which gives evidence that the coverage does not affect the response to NO_2. Compared to Figure 5.6, the drifts of Au-NPs deposited devices is much higher than the pristine devices. This is a disadvantage of Au-NPs deposited devices.

Compared to the response of the pristine device in Figure 5.7, the MLG strip with 0% Au-NPs coverage in this section has a rather low response. This may be caused by the bad printing alignment during the nanoparticle deposition process. Due to the limitation of the printer accuracy, it is hard to print nanoparticles on the desired area exactly, which can cause some nanoparticles deposited on 0% coverage strip. Further improvement of the printer alignment is needed to have a more accurate result.

5.2.3 The functionalized devices with Pt-NPs deposition

The devices tested in this section are deposited with different Pt-NPs coverages: 70%, 35%, 15%, and 10%, which are controlled by adjusting the print speed.

Figure 5.12 shows the sheet resistance change of the MLG strips with different Pt-NPs coverages to the exposure of NO_2 with the concentration of 1 ppm. And the responses are shown in Figure 5.13.

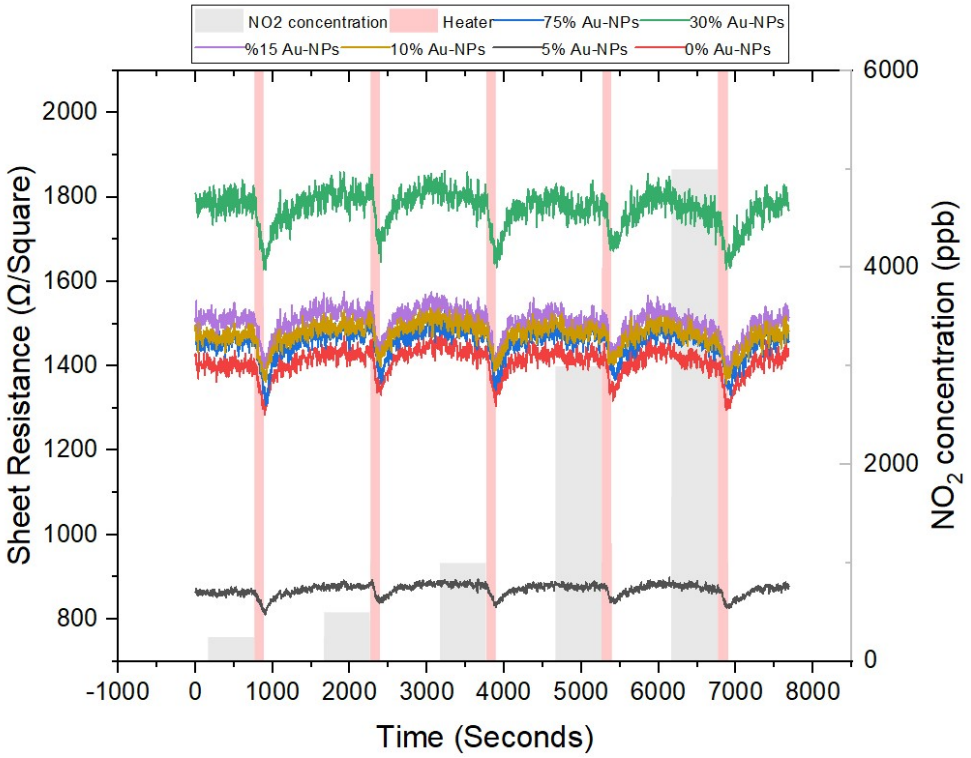

Figure 5.10: MLG sheet resistance of devices with different Au-NPs coverages at different NO_2 concentration steps. The heater is powered after each humidity step.

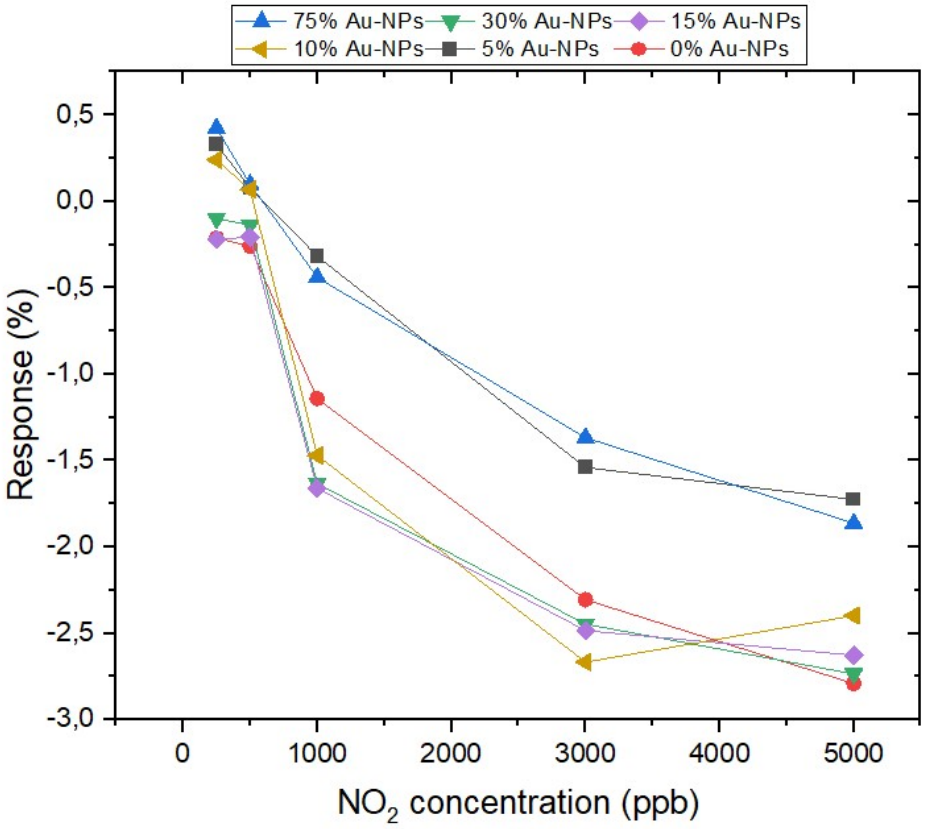

Figure 5.11: The response as a function of NO_2 concentration level. The responses were calculated by doing an average of the sheet resistance value during the first and last minute of exposure of the NO_2 steps.

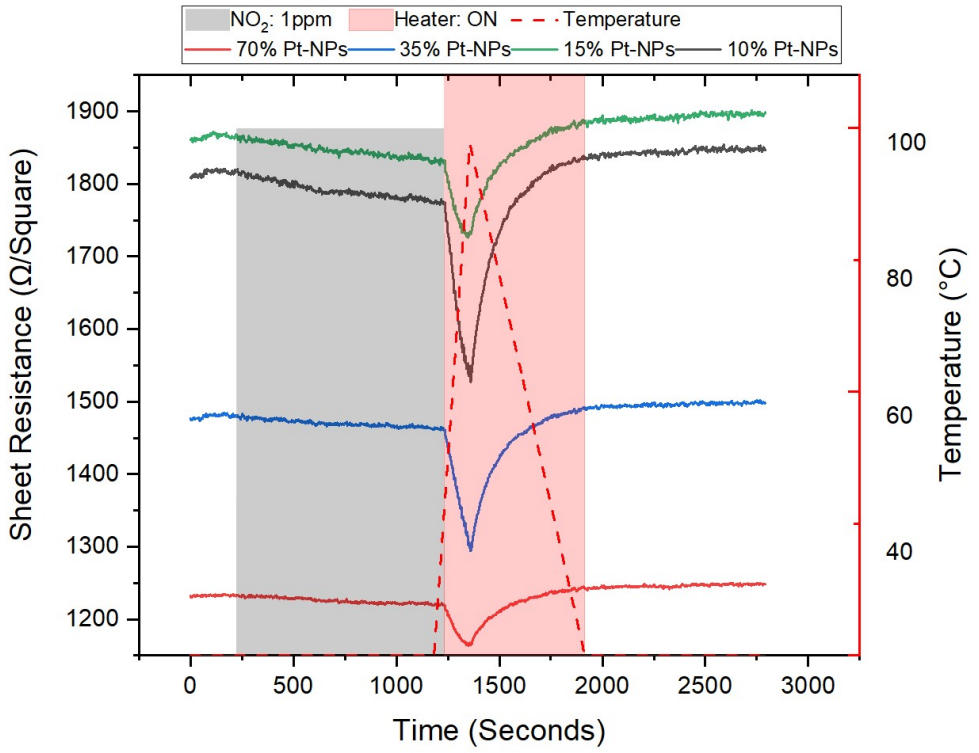

Figure 5.12: The response of device deposited by Pt-NPs with baseline in dry N_2, followed by 10 minutes of exposure to NO_2 with a concentration of 1 ppm. A heater is added to help the recovery. The pink area is the period that the temperature is higher than room temperature, while the red dash line is the real temperature of the heater.

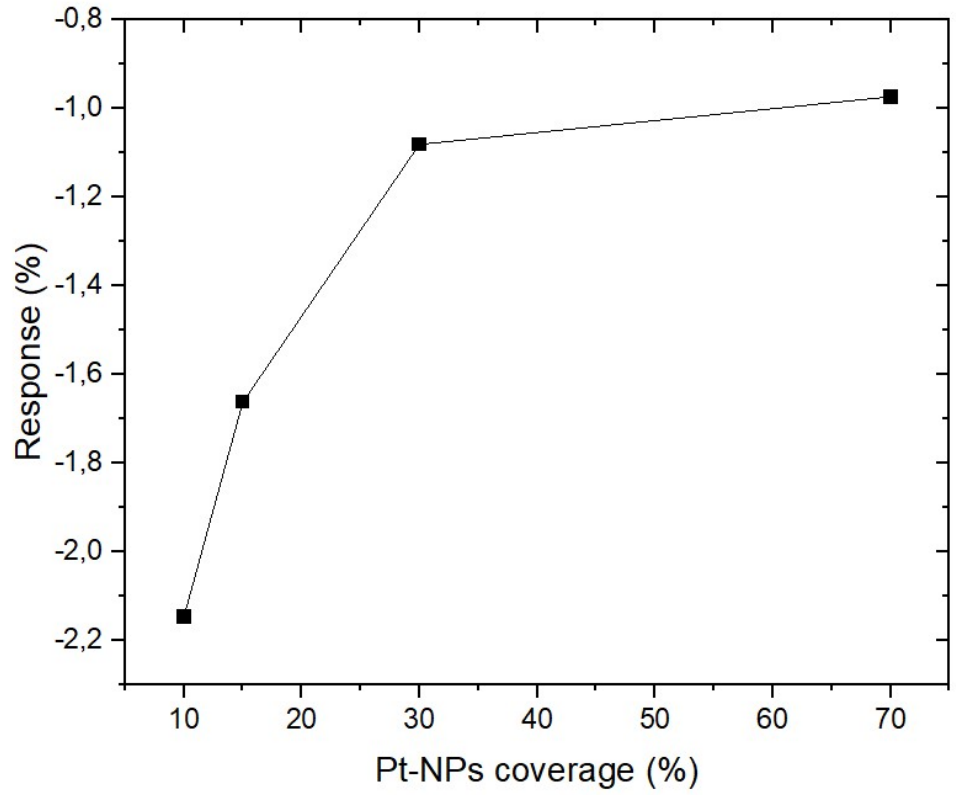

Figure 5.13: The response to 1 ppm of NO_2 as a function of different Pt-NPs coverage. The responses were calculated by doing an average of the sheet resistance value during the first and last minute of exposure of the NO_2 steps.

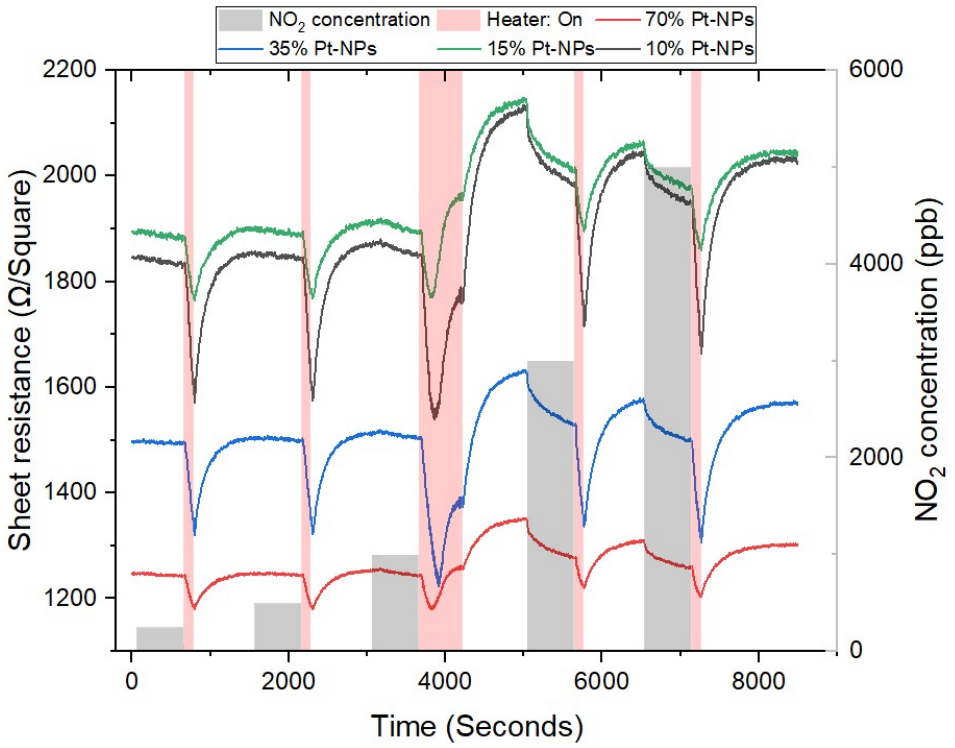

Figure 5.14: MLG sheet resistance of devices with different Pt-NPs coverages at different NO_2 concentration steps. The heater is powered after each humidity step.

Same as the pristine devices and Au-NPs deposited devices, the Pt-NPs devices also have a decreased sheet resistance to the exposure of NO_2. And after the recovery period with heating, the resistance values can also go back to the original state. From Figure 5.12, the MLG strips with different coverages also responded differently when the temperature was increased. But in this study, the response to different gases is the main issue, thus no in-depth research. Unlike the Au-NPs deposited devices, different Pt-NPs coverage has a clear effect on the response. The negative response decreases with the increase of the Pt-NPs coverage.

The sheet resistance change of MLG strips with different Pt-NPs coverages with the increased NO_2 concentration are shown in Figure 5.14, and the responses as a function of NO_2 concentration is shown in Figure 5.15.

The response to the flowing of NO_2 can be clearly observed. The long heating time caused the increased sheet resistance during the recovery step after the exposure of NO_2 with a concentration of 1 ppm. As shown in Figure 5.15, the significant decrease when the concentration is increased from 1 ppm to 3 ppm can be caused by this uneven heating time. Next to it, this gave evidence that the heating time is not long enough to complete the gas molecule desorption. The heating time needs to be prolonged in future experiments.

5.2.4 The functionalized devices with Cu-NPs deposition

The devices tested in this section are deposited with different Cu-NPs coverages: 50%, 30%, 15%, and 10%. The coverage can be controlled by adjusting the print speed.

Figure 5.16 shows the sheet resistance change of MLG strips with different Cu-NPs coverages to the exposure of NO_2 with the concentration of 1 ppm. This responses are shown in Figure 5.17.

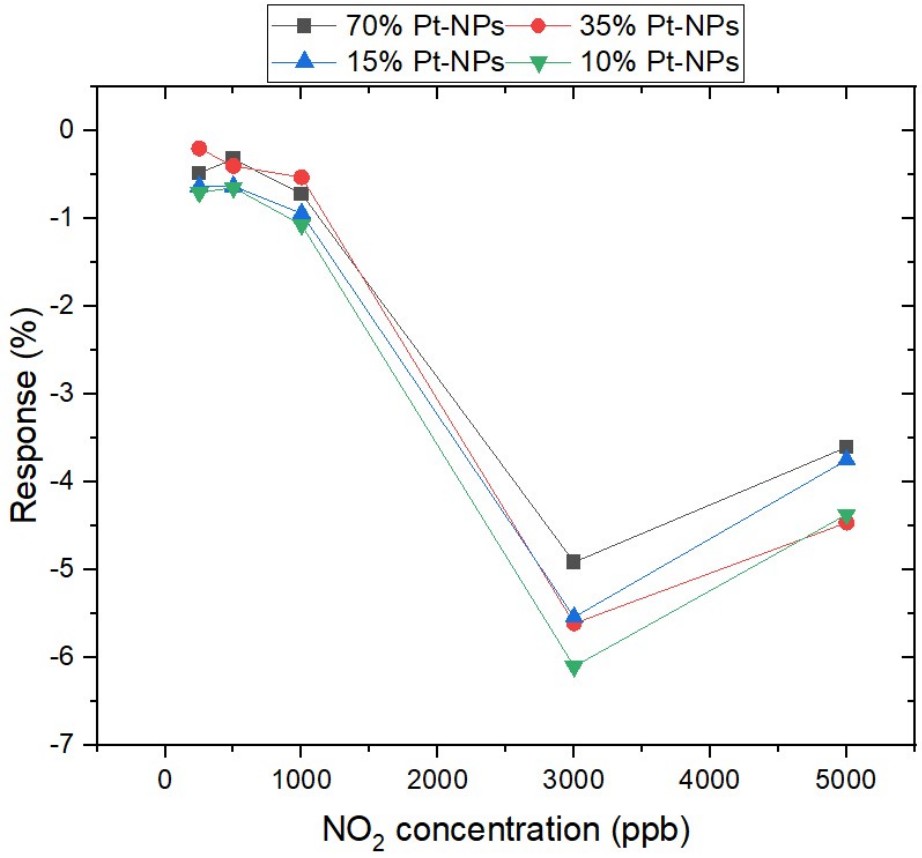

Figure 5.15: The response as a function of NO_2 concentration level. The responses were calculated by doing an average of the sheet resistance value during the first and last minute of exposure of the NO_2 steps.

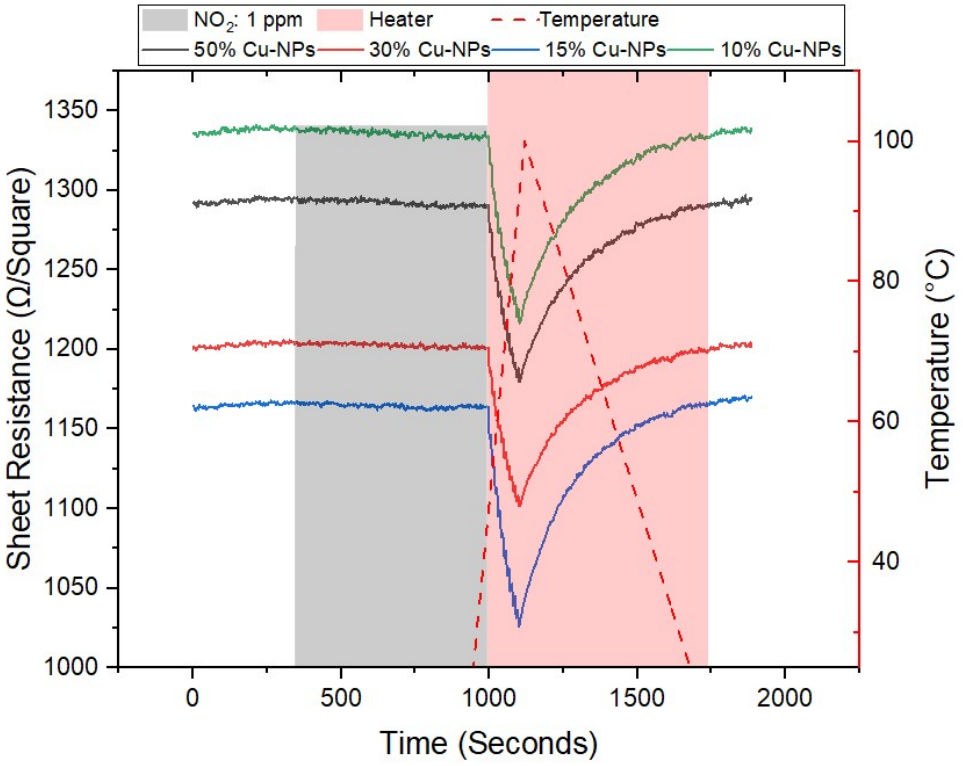

Figure 5.16: The response of device deposited by Cu-NPs with baseline in dry N_2, followed by 10 minutes of exposure to NO_2 with a concentration of 1 ppm. A heater is added to help the recovery. The pink area is the period that the temperature is higher than room temperature, while the red dash line is the real temperature of the heater.

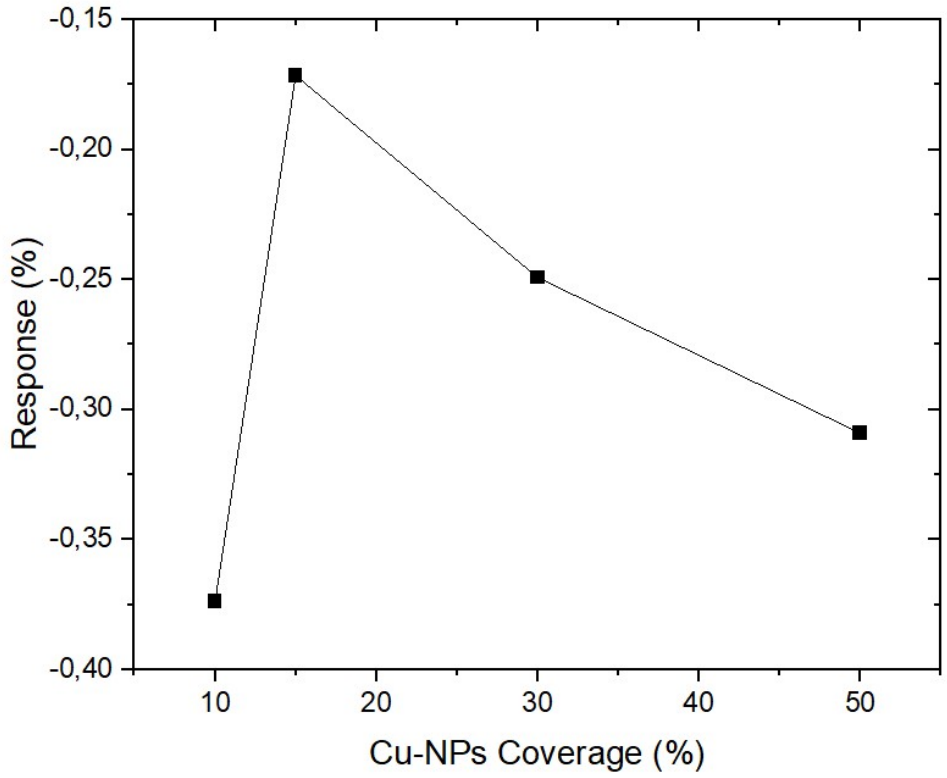

Figure 5.17: The response to 1 ppm of NO_2 as a function of different Cu-NPs coverage. The responses were calculated by doing an average of the sheet resistance value during the first and last minute of exposure of the NO_2 steps.

A decrease in sheet resistance can be observed. However, The response is much smaller than the response with other kinds of nanoparticle deposition. Hence, there is not enough evidence to justify the response is related to the Cu-NPs coverage.

MLG sheet resistance of devices with different Cu-NPs coverages at different NO_2 concentration steps are shown in Figure 5.18. And the responses are shown in Figure 5.19.

As shown in Figure 5.19, when the NO_2 concentration increased, the negative response also increased, which is contrary to Au-NPs deposited device.

5.3 DISCUSSION

In this chapter, all gas detection tests for $H2_O$ and NO_2 were discussed.

The results showed that both the pristine devices and the devices deposited with Au-NPs hardly reacted to the water molecules until the humidity increased to 80%. These results are consistent with the work[67]. The significant response at 85% humidity is due to the intercalation of water between the graphene layers[68].

The deposition of Au NPs showed no significant help in measuring humidity. They also showed little response when the humidity was less than 80%. However, when the humidity increased, the MLG strips showed increased sheet resistance, which is in contrast to the pristine devices. Further measurements of the Au-NPs coverage of the surface are needed to explore the reason for this.

As for NO_2, the pristine devices showed a promising response. However, a longer heating time is required for the devices to fully recover to the initial values.

However, the devices deposited with NPs showed a lower response to NO_2. One of the stripes on the device deposited with Au-NPs has coverage of 0%, but it still barely responded, unlike the pristine devices.

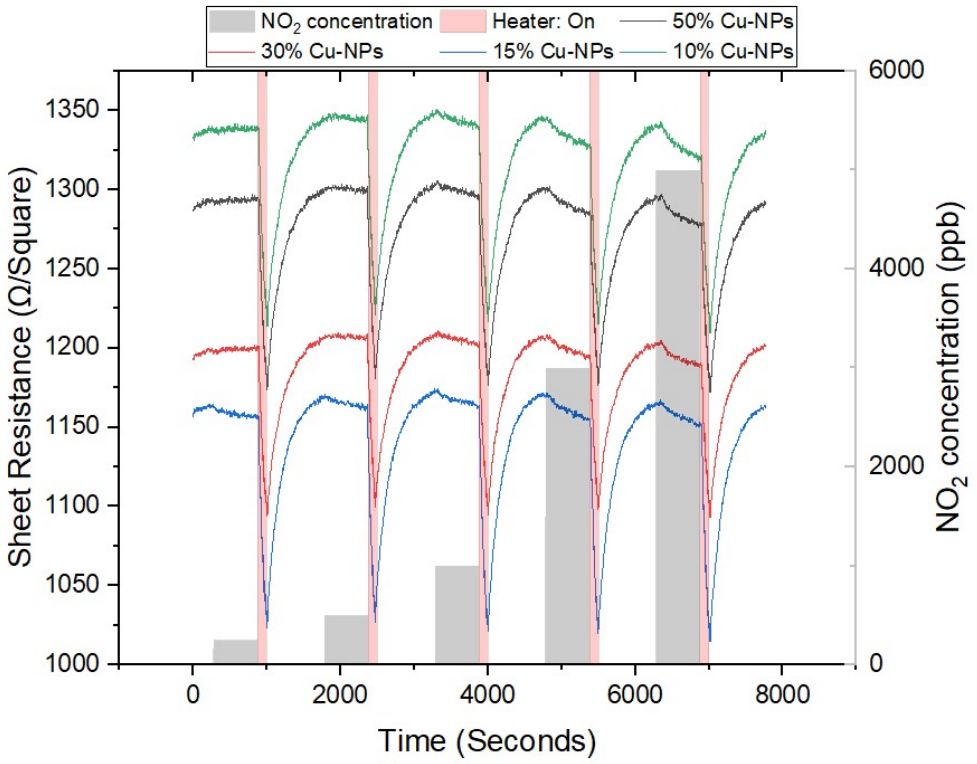

Figure 5.18: MLG sheet resistance of devices with different Cu-NPs coverages at different NO_2 concentration steps. The heater is powered after each humidity step.

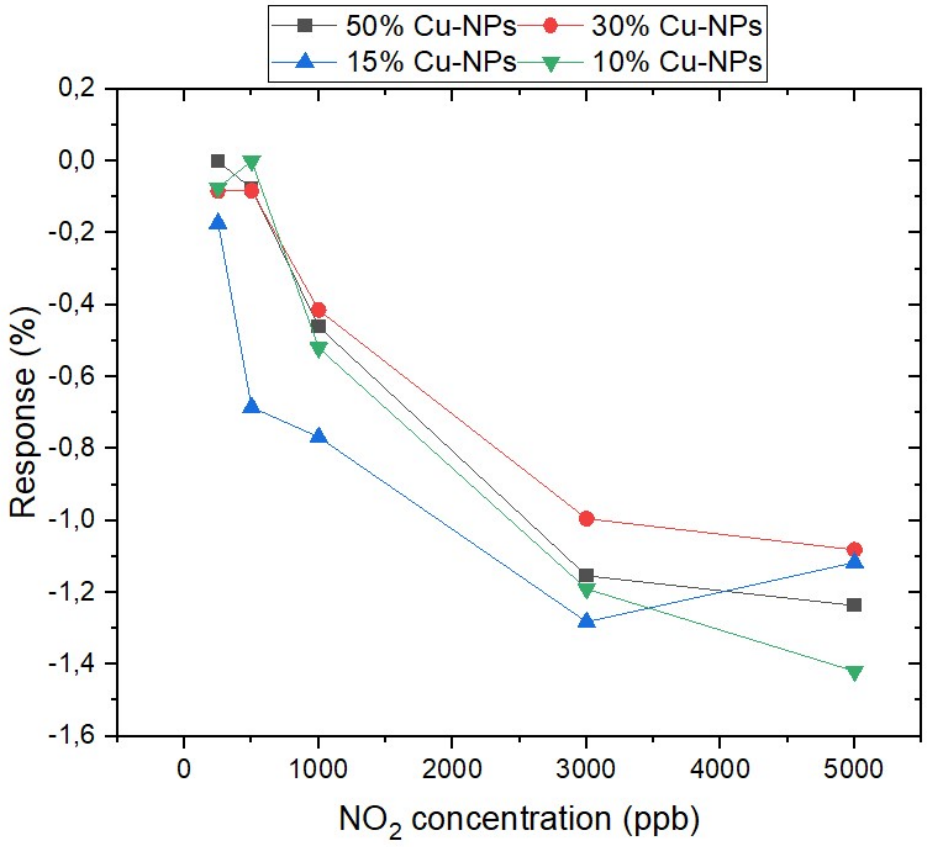

Figure 5.19: The response as a function of NO_2 concentration level. The responses were calculated by doing an average of the sheet resistance value during the first and last minute of exposure of the NO_2 steps.

Device type	The largest response	at the coverage of
Pristine device	5.7%	-
Au-NPs decorated device	1.6%	15%
Pt-NPs decorated device	2.2%	10%
Cu-NPs decorated device	0.375%	10%

Table 5.1: The maximum response and the corresponding coverage of each type of device.

Compared to other devices, those deposited with Au-NPs have more noise. One possible reason is that Au-NPs have efficient local heating when the surface plasmon oscillation is excited. This resulted in more noise than other metal/metal oxide nanoparticles.

Even though Pt-NPs deposited devices have a stronger response than Au-NPs and Cu-NPs devices have a lower response, they all have a lower response than the pristine devices. And for all three types of devices, there is no clear indication that the response is strongly related to the coverage values. This is due not only to the lack of data sets and replicates but also to the possible misalignment problem. Among the functionalized devices, the devices deposited with Pt-NPs have a close response to the pristine device.

Contrary to our expectations, after functionalization of the NPs, the response of the sensor to the gas is reduced to varying degrees. With respect to NO_2 with a concentration of 1 ppm, the response is a maximum of 5.7% for the pristine devices, 1.6% for the devices deposited with Au-NPs with a coverage of 15%, 2.2% for the devices deposited with Pt-NPs with a coverage of 10%, and 0.375% for the devices deposited with Fe-NPs with coverage of 10% as shown in

There are a couple of possible reasons for this. The first reason is that during the printing of the NPs, some impurities can cause contamination, which changed the electronic properties of the graphene. The increased sheet resistance after the deposition of the NPs can also be explained by this reason. Another reason is that the NPs deposited in this study did not act as a catalyst but as an obstacle for gas sensing. This could also explain the lower response to the higher Pt- NP coverages.

To design a sensor array, the response to many gases is needed. It may be that the previously measured devices are poor only for detecting NO_2, but to other gases, the deposited devices may respond more strongly than pristine devices. Experiments with other gases will need to be performed in future work to verify this.

6 CONCLUSION AND RECOMMENDATIONS

Graphene as an allotrope of carbon is promising for the detection of gaseous molecules due to its extremely high surface-to-volume ratio. However, its low selectivity is still a major problem for practical use. In this study, a gas sensor based on graphene functionalized with nanoparticles was explored. Four different metal/metal oxides were tested and evaluated for their effects on the response to different gases.

First, the gas sensor was fabricated, and graphene was synthesized by selective CVD growth on patterned Mo. The graphene strips on a device were arranged in the shape of an octagon to act as a sensor array. Each strip has a size of 200 μ m x 20 μm. The functionalized nanoparticles were deposited with a nanoparticle printer that used the principle of spark ablation. Four metal/metal oxides were tested in this study: Au, Pt, Cu, and Fe, of which Cu and Fe can be oxidized once they come into contact with air. The types of nanoparticles were selected according to the existing experimental literature.

Subsequently, material characterization was investigated to explore the effects of nanoparticles on the physical and electrical properties of graphene. The Raman spectroscopy results showed no significant difference after functionalization, while the surface morphology of the device was significantly changed by SEM and AFM, proving that the nanoparticles were bound to graphene. To optimize the printing parameters and determine the relationship between nanoparticle coverage and printing parameters, SEM images with different printing speeds were used to calculate the coverage value. Four different coverage values for each type of nanoparticle were selected to be tested in the following gas tests. Also, annealing tests were performed to obtain information about the changes of coverage after annealing. It is found that the coverage of Au and Pt nanoparticles decreases when the annealing temperature increases, while Cu and Fe nanoparticles hardly change. As for multiple annealing at the same temperature, all four types of nanoparticles showed no significant changes. The coverage values obtained after annealing are used for the following gas test.

Electrical characterization of the devices was also performed. The I-V characteristics showed the resistance properties of the MLG strips. The average sheet resistance of 1.52 $k\Omega$ was measured according to an illustrated wafer map inFigure 4.30. The center portion of the wafer exhibited stable sheet resistance compared to the edge of the wafer. This may be due to the non-uniformity of heating in the Blackmagic during graphene growth, resulting in a higher temperature in the center. The thermal resistance coefficient of the MLG strip is $(-9.43 \pm 0.14) * 10^{-4} K^{-1}$, which means that it has lower resistance at higher temperature.

In this study, a complete gas test measurement setup was presented. A gas generator equipped with several gas permeation tubes and a humidity generator was used to generate and control the gas flow. The measured gas flowed into a specially designed chamber that incorporated a ceramic heater. The wired device was placed on the heater with all contact surfaces connected to the fifty needles of the chamber for electrical data acquisition. For data acquisition, a multiplexer and source meter were coded with LabView for strip switching and data acquisition.

As a final step, humidity and NO_2 were tested. As for humidity, the pristine devices barely responded until the humidity level rose above 80%. The devices with the Au-NPs deposited also showed little response, but in different directions.

With respect to NO_2, the same experiments were performed with pristine devices and devices coated with Au, Pt, and Cu-NPs. Among these devices, pristine devices

showed the largest response, which was not in accordance with our assumption. All the devices showed a negative response to NO_2. This is because NO_2 as an oxidizing gas could increase the conductivity of graphene by reacting with the hole accumulation layer formed on the surface of p-type graphene. And only for the devices deposited with Pt-NPs, there is a clear inverse relationship between the coverage and the reaction. For the other functionalized devices, it is difficult to conclude that nanoparticle coverage has an effect on the response to NO_2. Moreover, the devices deposited with Au-NPs have stronger noise, and the devices deposited with Cu-NPs have the lowest response. Considering all these results, Pt-NPs can be a potential functionalized material for NO_2 detection.

Even though the functionalized devices have a small response to NO_2, they can still show a larger response to other gases, which is essential for the gas sensor array. The sensor array consists of multiple sensors that respond differently to the gases, which facilitates the detection of fingerprints in complex mixtures.

The work in this study is not sufficient to develop a sensor array to detect multiple gases, but it shows the potential for such an approach to be successful. There is still much work to be done in the future:

- X-ray diffraction (XRD) is needed to identify the composition of the oxidized nanoparticles for Cu and Fe.
- The imfluence of the dielectric layer on the sensing mechanisms needs to be investigated.
- The protocols for the gas test need to be completed and improved to avoid system errors.
- A large number of replicates need to be performed to obtain additional information on the reliability of the conclusion.
- More gases need to be tested to study the effects of nanoparticles on sensitivity to other gases.
- More metal/metal oxide nanoparticles can be explored to further improve the selectivity of the sensor array.
- A suitable method for accelerating recovery needs to be explored to achieve rapid recovery.

BIBLIOGRAPHY

[1] J. Phiri, "General overview of graphene: Production, properties and application in polymer composites," *Materials Science and Engineering: B*, vol. 215, pp. 9–28, 2017.

[2] A. H. C. Neto, "The electronic properties of graphene," *Reviews of Modern Physics*, vol. 81, pp. 109–162, 2009.

[3] E. W. Hill, "Graphene sensors," *IEEE Sensors Journal*, vol. 11, pp. 3161–3170, 2011.

[4] N. Mishra, "Graphene growth on silicon carbide: A review," *physica status solidi (a)*, vol. 213, pp. 2277–2289, 2016.

[5] M. Pykal, "Modelling of graphene functionalization," *Physical chemistry chemical physics : PCCP*, vol. 18, 2015.

[6] F. Schedin, "Detection of individual gas molecules adsorbed on graphene," *Nature Materials*, vol. 6, pp. 652–655, 2007.

[7] W. Yuan, "Graphene-based gas sensors," *Journal of Materials Chemistry A*, vol. 1, pp. 10078–10091, 2013.

[8] X. Yan, "High-performance uv-assisted no 2 sensor based on chemical vapor deposition graphene at room temperature," *ACS Omega*, vol. 4, 2019.

[9] A. Schmidt-Ott, *Spark Ablation: Building Blocks for Nanotechnology*. CRC Press, 2019.

[10] S. Vollebregt, "A transfer-free wafer-scale cvd graphene fabrication process for mems/nems sensors," *2016 IEEE 29th International Conference on Micro Electro Mechanical Systems (MEMS)*, 2016.

[11] "Advantages of 4 wire resistance measurement — disadvantage of four wire resistance measurement.." https://www.rfwireless-world.com/Terminology/Advantages-of-4-Wire-Resistance-Measurement.html. Accessed: 2022-07-20.

[12] "Granite, "what is raman spectroscopy? — raman spectroscopy principle," edinburgh instruments.." https://www.edinst.com/blog/what-is-raman-spectroscopy/. Accessed: 2022-07-21.

[13] L. M. Malard, "Raman spectroscopy in graphene," *Physics Reports*, vol. 473, 2009.

[14] G. Hübschen, *Materials Characterization Using Nondestructive Evaluation (NDE) Methods*. Woodhead Publishing, 2016.

[15] "Atomic force microscopy: General principles and applications." https://www.azooptics.com/Article.aspx?ArticleID=2083. Accessed: 2022-07-27.

[16] A. Aytimur, "Calcia stabilized ceria doped zirconia nanocrystalline ceramic," *Journal of Inorganic and Organometallic Polymers and Materials*, vol. 24, 2014.

[17] W. H. Organization, *WHO global air quality guidelines: particulate matter (PM2.5 and PM10), ozone, nitrogen dioxide, sulfur dioxide and carbon monoxide*. World Health Organization, 2021.

[18] "Particulate air pollution is the single greatest threat to human health globally.." https://aqli.epic.uchicago.edu/pollution-facts/. Accessed: 2022-08-15.

[19] H. Tang, "Recent advances in 2d/nanostructured metal sulfide-based gas sensors: mechanisms, applications, and perspectives," *Journal of Materials Chemistry A*, vol. 8, pp. 24943–24976, 2020.

[20] N. Yamazoe, "Toward innovations of gas sensor technology," *Sensors and Actuators B: Chemical*, vol. 108, pp. 2–14, 2005.

[21] H. Ding, "Recent advances in gas and humidity sensors based on 3d structured and porous graphene and its derivatives," *ACS Materials Letters*, vol. 2, pp. 1381–1411, 2020.

[22] I. V. Zaporotskova, "Carbon nanotubes: Sensor properties. a review," *Modern Electronic Materials*, vol. 2, pp. 95–105, 2016.

[23] C. Anichini, "Chemical sensing with 2d materials," *Chemical Society Reviews*, vol. 47, pp. 4860–4908, 2018.

[24] M. Rodner, "Performance tuning of gas sensors based on epitaxial graphene on silicon carbide," *Materials Design*, vol. 153, pp. 153–158, 2018.

[25] A. Star, "Gas sensor array based on metal-decorated carbon nanotubes," *The Journal of Physical Chemistry B*, vol. 110, pp. 21014–21020, 2006.

[26] P. R. Wallace, "The band theory of graphite," *Publisher: American Physical Society*, vol. 71, pp. 622–634, 1947.

[27] K. S. Novoselov, "Electrical field effect in atomically thin carbon film," *Science*, vol. 306, pp. 666–669, 2004.

[28] C. Lee, "Measurement of the elastic properties and intrinsic strength of monolayer graphene," *Science*, vol. 321, pp. 385–388, 2008.

[29] Y. Zhu, "Graphene and graphene oxide: Synthesis, properties, and applications," *Advanced Materials*, vol. 22, 2010.

[30] R. R. Nair, "Fine structure constant defines visual transparency of graphene," *Science*, vol. 320, 2008.

[31] A. A. Balandin, "Superior thermal conductivity of single-layer graphene," *Nano Letters*, vol. 8, 2008.

[32] M. Rodner, "Functionalized epitaxial graphene as versatile platform for air quality sensors," *Linköping University Electronic Press*, 2021.

[33] A. K. Geim, "The rise of graphene," *Nature Materials*, vol. 6, pp. 183–191, 2007.

[34] Q. Yu, "Graphene segregated on ni surfaces and transferred to insulators," *Applied Physics Letters*, vol. 93, p. 113103, 2008.

[35] X. Li, "Large-area synthesis of high-quality and uniform graphene films on copper foils," *Science (New York, N.Y.)*, vol. 324, pp. 1312–1314, 2009.

[36] J. Lin, "Laser-induced porous graphene films from commercial polymers," *Nature communications*, vol. 5, p. 5714, 2014.

[37] J. Moser, "The environment of graphene probed by electrostatic force microscopy," *Applied Physics Letters*, vol. 92, p. 123507, 2008.

[38] J. Burgués, "Estimation of the limit of detection in semiconductor gas sensors through linearized calibration models," *Analytica Chimica Acta*, vol. 1013, 2018.

[39] H. Wu, "Gas sensing performance of graphene-metal contact after thermal annealing," *Sensors and Actuators B: Chemical*, vol. 282, 2019.

[40] J. E. Lee, "Optical separation of mechanical strain from charge doping in graphene," *Nature Communications*, vol. 3, 2012.

[41] X. Chen, "Uv-light-assisted no2 gas sensor based on ws2/pbs heterostructures with full recoverability and reliable anti-humidity ability," *Sensors and Actuators B: Chemical*, vol. 339, 2021.

[42] M. Rodner, "Metal oxide nanolayer-decorated epitaxial graphene: A gas sensor study," *Nanomaterials*, vol. 10, 2020.

[43] V. Schroeder, "Carbon nanotube chemical sensors," *Chemical Reviews*, vol. 119, 2019.

[44] D. J. Buckley, "Frontiers of graphene and 2d material-based gas sensors for environmental monitoring," *2D Materials*, vol. 7, 2020.

[45] A. V. Singhal, "Noble metal decorated graphene-based gas sensors and their fabrication: A review," *Critical Reviews in Solid State and Materials Sciences*, vol. 42, 2017.

[46] B. Alfano, "Modulating the sensing properties of graphene through an eco-friendly metal-decoration process," *Sensors and Actuators B: Chemical*, vol. 222, 2016.

[47] H. Song, "Morphology optimization of cvd graphene decorated with ag nanoparticles as ammonia sensor," *Sensors and Actuators B: Chemical*, vol. 244, 2017.

[48] J. Eriksson, "Adjusting the electronic properties and gas reactivity of epitaxial graphene by thin surface metallization," *Physica B: Condensed Matter*, vol. 439, 2014.

[49] D. Raeyani, "Synthesizing graphene quantum dots for gas sensing applications," *Procedia Engineering*, vol. 168, 2016.

[50] Y. Zou, "An ab initio study on gas sensing properties of graphene and si-doped graphene," *The European Physical Journal B*, vol. 81, 2011.

[51] J. Lu, "Preparation of ag nanoparticles by spark ablation in gas as catalysts for electrocatalytic hydrogen production," *RSC Advances*, vol. 10, 2020.

[52] W. Yang, *Sensor Array*. IntechOpen, 2012.

[53] K. Persaud, "Analysis of discrimination mechanisms in the mammalian olfactory system using a model nose," *Nature*, vol. 299, 1982.

[54] A. Lipatov, "Intrinsic device-to-device variation in graphene field-effect transistors on a si/sio2 substrate as a platform for discriminative gas sensing," *Applied Physics Letters*, vol. 104, 2014.

[55] S.-M. Kim, "Residue-free suspended graphene transferred by perforated template," *Nanotechnology*, vol. 33, 2022.

[56] A. C. Ferrari, "Raman spectroscopy as a versatile tool for studying the properties of graphene," *Nature Nanotechnology*, vol. 8, 2013.

[57] D. R. Lenski, "Raman and optical characterization of multilayer turbostratic graphene grown via chemical vapor deposition," *Journal of Applied Physics*, vol. 110, 2011.

[58] A. Eckmann, "Raman study on defective graphene: Effect of the excitation energy, type, and amount of defects," *Physical Review B*, vol. 88, 2013.

[59] Y. Grachova, "High quality wafer-scale cvd graphene on molybdenum thin film for sensing application," *Procedia Engineering*, vol. 87, 2014.

[60] L. Lu, *Iron Ore*. Woodhead Publishing, 2015.

[61] M. J. Coutts, "Rapid and controllable sintering of gold nanoparticle inks at room temperature using a chemical agent," *The Journal of Physical Chemistry C*, vol. 113, 2009.

[62] P. Zeng, "Nanoparticle sintering simulations1this paper was presented at the microstructural evolution in bulk phases," *Materials Science and Engineering: A*, vol. 252, 1998.

[63] J. Torres, "Effects of surface modifications to single and multilayer graphene temperature coefficient of resistance," *ACS Applied Materials Interfaces*, vol. 12, 2020.

[64] Y. Que, "Graphene–silicon layered structures on single-crystalline ir(111) thin films," *Advanced Materials Interfaces*, vol. 2, 2015.

[65] A. D. Smith, "Resistive graphene humidity sensors with rapid and direct electrical readout," *Nanoscale*, vol. 7, 2015.

[66] V. I. Popov, "Graphene-based humidity sensors: the origin of alternating resistance change," *Nanotechnology*, vol. 28, 2017.

[67] F. Ricciardella, "Low-humidity sensing properties of multi-layered graphene grown by chemical vapor deposition," *Sensors*, vol. 20, 2020.

[68] A. Qadir, "Effect of humidity on the interlayer interaction of bilayer graphene," *Physical Review B*, vol. 99, 2019.

A LABVIEW SCRIPT FOR AUTOMATIC MEASUREMENT

2612BDEMO_8channel.vi
C:\Users\MSI-NB\Downloads\2612BDEMO_8channel.vi
Last modified on 2022/7/20 at 19:48
Printed on 2022/7/20 at 22:54

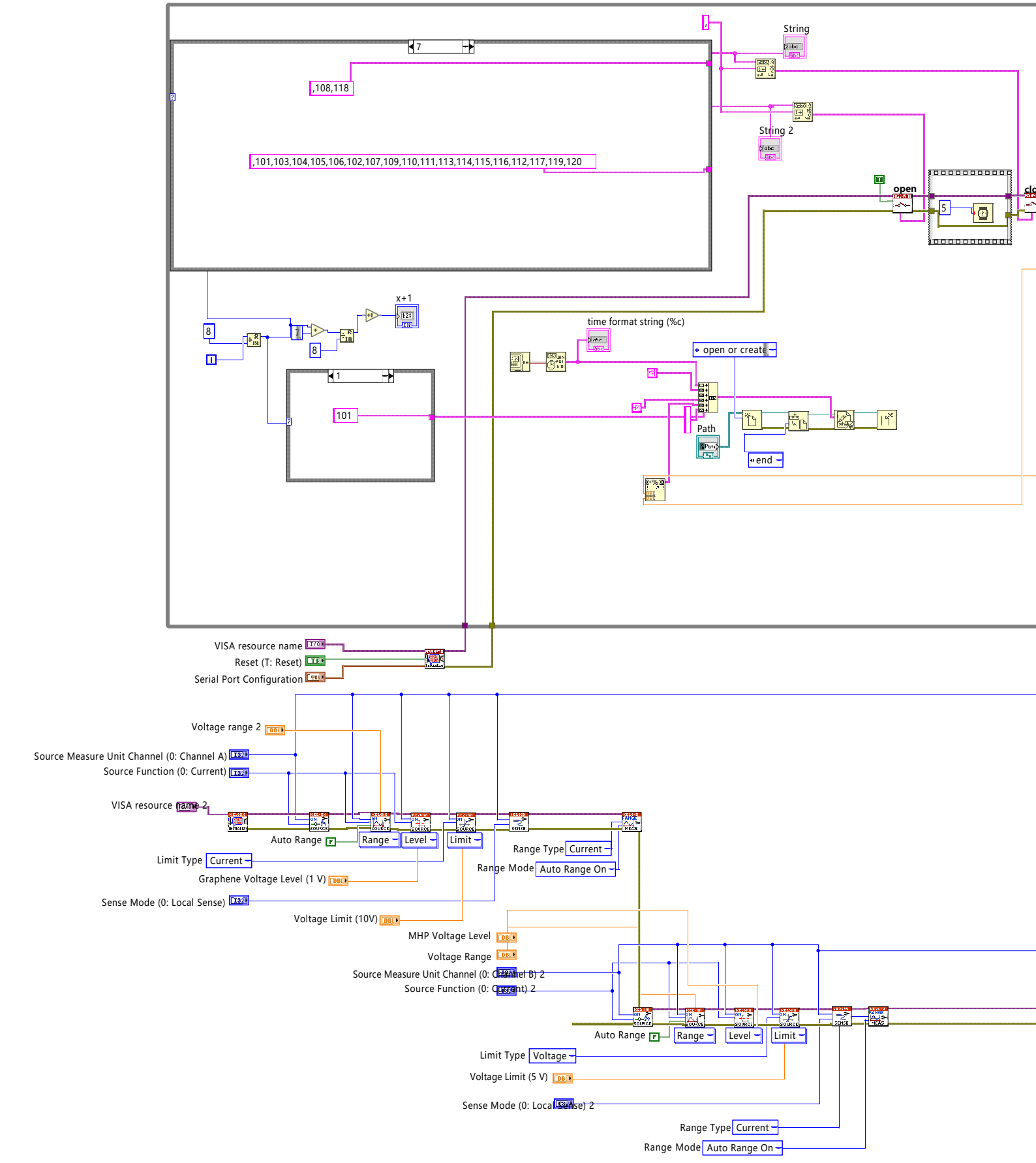

2612BDEMO_8channel.vi
C:\Users\MSI-NB\Downloads\2612BDEMO_8channel.vi
Last modified on 2022/7/20 at 19:48
Printed on 2022/7/20 at 22:54

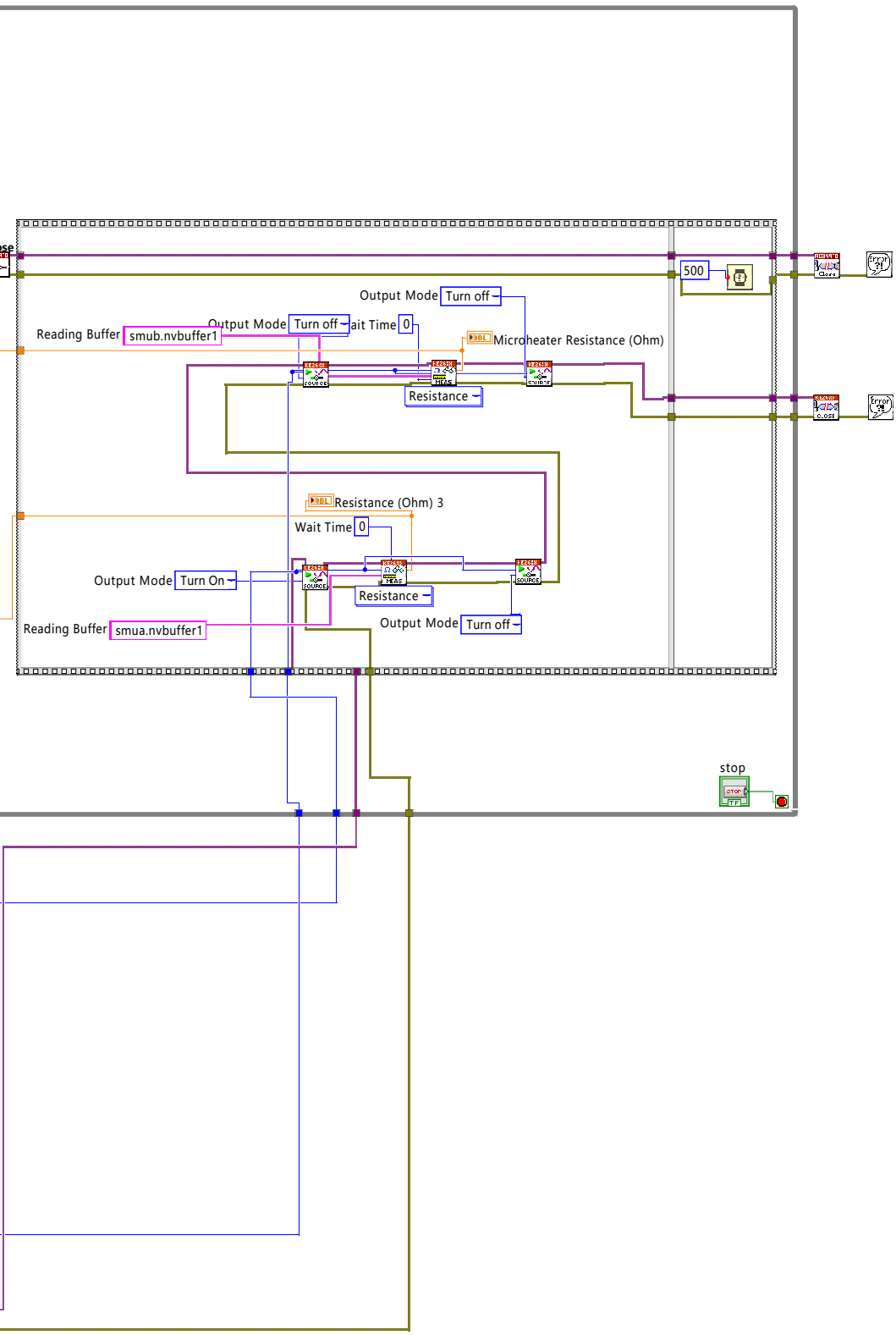

2612BDEMO_8channel.vi
C:\Users\MSI-NB\Downloads\2612BDEMO_8channel.vi
Last modified on 2022/7/20 at 19:48
Printed on 2022/7/20 at 22:54

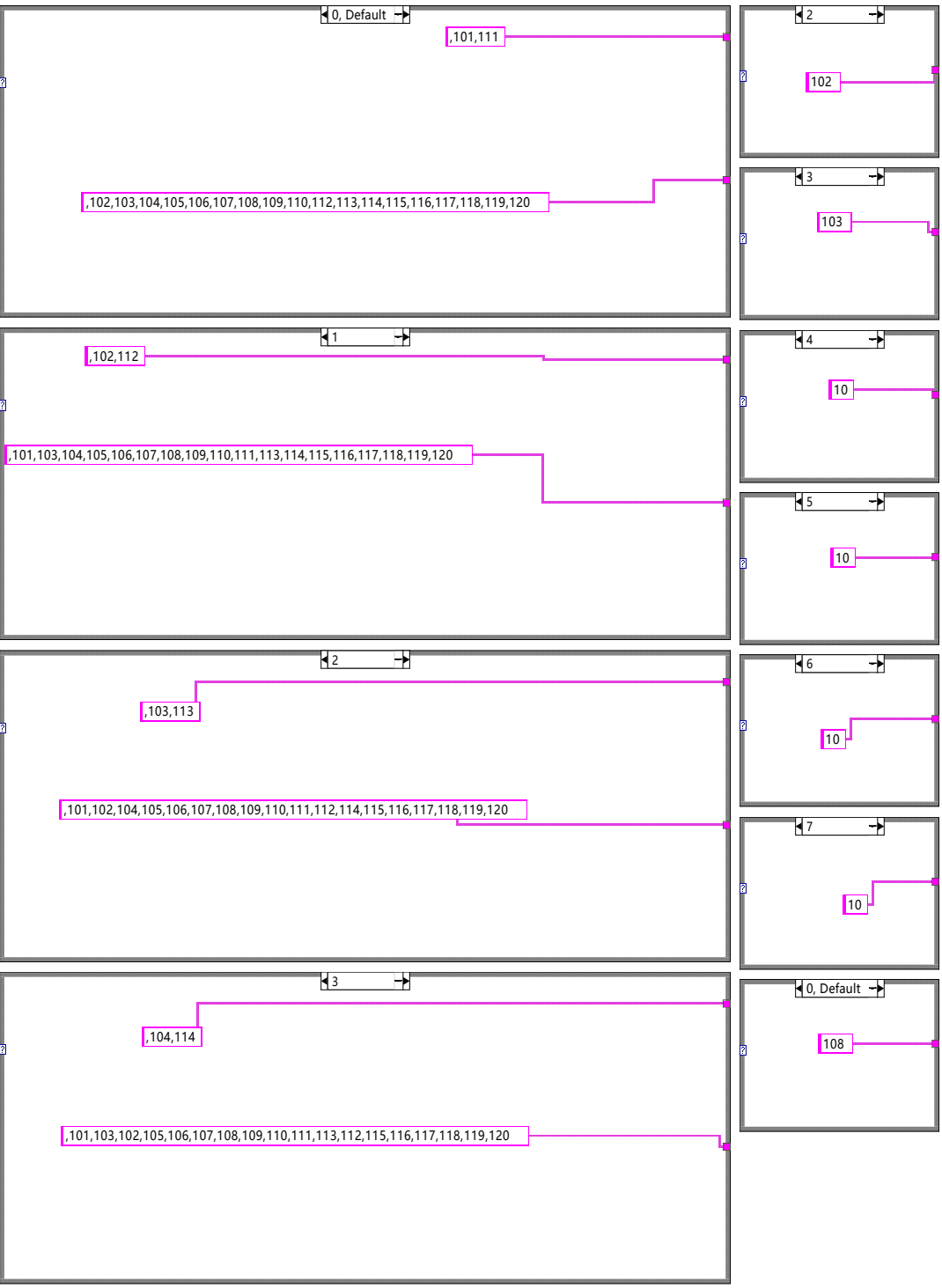

2612BDEMO_8channel.vi
C:\Users\MSI-NB\Downloads\2612BDEMO_8channel.vi
Last modified on 2022/7/20 at 19:48
Printed on 2022/7/20 at 22:54